Doctoral Thesis

On the Strengthening of Laser Powder Bed Fusion Titanium Alloys by Interstitial Carbon

侵入型炭素原子によるチタン粉末積層造形合金の固溶強化

Peterson Jack Edward

June 2023

Graduate School of Engineering
Osaka University

This thesis is presented to the Osaka University Graduate School of Engineering as the doctoral dissertation of Jack Edward Peterson in June 2023.

Table of Contents

Chapter 1:
Introduction

1.1 Metallurgy

The complaint tablet to Ea-Nasir from the Old Babylonian period is perhaps the oldest known instance of poor customer service[1]. In the tablet, the author laments about the poor quality of copper ingots sold by the merchant Ea-Nasir at a high price and with an attitude of contempt[2]. While the copper ingots of Ea-Nasir have withered and decayed, the author's primal human desire to readily acquire good quality metal ingots has endured through millennia.

Metal manufacturing technology has advanced substantially since the days of poor-quality copper merchants. However, the fundamentals of early metallurgy remain relevant. A good alloy must be strong enough to last, but not so brittle that it will shatter. Metals harden when worked, but heat can soften them again. A high-purity metal can be less useful than one with carefully controlled additives. The first major advancements in early copper technology were the addition of other elements to make alloys. Tin was added to make bronze, improving mechanical performance. Zinc was added to make brass, improving color and corrosion resistance. During the iron age, substitutional metal-metal alloys were succeeded by interstitial alloys, namely steel. The addition of carbon to an iron matrix could be used to improve the hardness of steel or lower the melting point of cast iron.

Modern metallurgy has unlocked access to the entire periodic table's worth of alloying elements. However, that means there are thousands of binary elemental combinations and countless more higher order combinations to explore. This overabundance of choice in alloy design can be focused down by two considerations: the properties of the base metal and

availability or cost of individual components. In the case of the aforementioned bronze, copper was highly processable with contemporary technology, and tin was readily available.

1.2 Titanium

The properties of titanium make it an attractive base alloying metal for a wide range of applications. The two defining properties of titanium are its high specific strength and excellent corrosion resistance. It also has two stable crystallographic phases, α and β, providing additional design space for highly tunable properties. The β-phase is normally only stable at high temperatures in pure titanium, so β-phase stabilizing elements like molybdenum or vanadium must be alloyed into a titanium matrix in order to achieve the most desirable properties[3].

High specific strength refers to a high strength to density ratio and means that a lower mass of material is required to support a fixed mechanical load. Lowering the mass of parts is of particular interest to the transportation and avionics industries, where reducing mass improves fuel efficiency and speed. However, commercially pure titanium (CP-Ti) has a much lower absolute yield strength than other structural metals like steel[4]. To combat this, high-strength titanium alloys have been developed to increase absolute strength without sacrificing its specific strength.

By far the most popular high strength alloy is Ti – 6 wt.% Al – 4 wt.% V (Ti64) which is a duplex α-β alloy[5–7]. Ti64 was developed in 1951, shortly after the development of industrial titanium production by the Kroll process in 1946[8]. Its long history of production and use has made Ti64 the benchmark standard for high strength titanium alloys. It sees widespread use in airplane turbine blades, airframe components, high pressure vessels, biomedical implants, and countless more applications[9–11].

The corrosion resistance of titanium and its alloys allows them to be used in a wide variety of reactive environments. In the transportation industry, titanium can improve the lifespan of the parts of ocean faring vessels that are constantly exposed to a salt-rich environment[12]. Titanium alloys are also excellent implant materials, having particularly high biocompatibility in bone implants due to their corrosion resistance and low elastic moduli. The good corrosion resistance prevents decay of the implant over the course of its lifetime in an extremely active environment. While stainless steel, the main competitor alloy for biomedical applications, also has good corrosion resistance, titanium alloys have lower elastic moduli. The elastic modulus of titanium is closer than the elastic modulus of stainless steel to that of bone. Matching the elastic modulus of the implant to that of bone prevents the stress shielding effect, where the bone is shielded from experiencing any mechanical loads and atrophies away. Traditionally, CP-Ti and Ti64 are the primary alloys used for implant purposes[9,13]. While CP-Ti has proven its excellent biocompatibility, it has a sub-standard mechanical performance.

Furthermore, the vanadium in Ti64 has been suggested to have cytotoxic effects[14]. There is ample opportunity for new, low elastic modulus, low toxicity alloys in biomedical applications.

While β-phase titanium alloys are not as widely produced as CP-Ti and Ti64, they excel in their specific applications[3,15]. β-phase alloys are notable for their heat treatability and low elastic modulus relative to α-phase alloys. Due to the low stability but high crystallographic symmetry of the β-phase, the mechanical properties of β-phase alloys can be varied wildly by heat treatment. A part can be machined into shape while in the softer full-β state, then heat treated up to high strength for implementation via the precipitation of metastable phases[16]. These β-phase alloys were first adopted by the aerospace industry during the production of the SR-71 "Blackbird" and are still frequently used in springs and landing gear[15,17]. β-phase Ti alloys are also a strong candidate material for future implants because the low elastic modulus of the β-phase is close to that of bone. The binary titanium-molybdenum system is particularly promising because up to 15 wt.% molybdenum further improves the corrosion resistance of titanium[18,19].

To accommodate these applications, 5.7 million metric tons of titanium were mined in 2022[20]. Most titanium is mined in China and southern Africa from ilmenite ore, although rutile ores are also mined to a lesser extent[20,21]. Over 95% of this titanium is used for pigment production, as TiO_2 can produce a bright white pigment[20]. While a smaller mass of titanium is used for the production of metallic alloys, the titanium metal industry has a much larger economic footprint. In 2021, 4.51 billion USD worth of titanium was traded globally[22]. The titanium market is still growing rapidly, indicating strong interest in and economic viability of titanium alloy design[23].

1.3 Additive Manufacturing of Metals

Metals have an excellent balance of durability and formability. Traditionally, objects made of metal were considered to be of higher quality than wood or ceramic because they do not rot away after getting wet or shatter when dropped. However, strong and durable materials are by definition difficult to form. In traditional metalworking, the primary strategy is to make the metal hot and then hit it repeatedly with a hammer until it reaches the desired shape. Modern conventional manufacturing has improved this technique by automating it, but the general principle of forging has stayed the same. Automation has allowed other traditional techniques to expand in scale and speed. Casting, milling, and welding are all integral parts of conventional manufacturing methods with a robust history of use.

The conventional metals manufacturing industry is currently being disrupted by additive manufacturing (AM) techniques[24]. In AM, parts are made by incrementally fusing new feedstock material onto the workpiece. With metals, this often involves using a laser to weld powder together. While AM has historical precedent in a few fringe cases for materials like

ceramics, AM of metals is relatively unexplored. As a joining technique, metallic AM shares many similarities with welding. Laser welding in particular provides some basis for metallic AM due to their shared features. However, the scale of welding a single interface versus millions of powder particles is quite different. This newly flourishing manufacturing technique has opened up new frontiers for materials research and design.

AM's niche in metals manufacturing is currently for production of medium-small sized parts with complex geometries in low quantities. The incremental approach of AM is not well suited to quickly creating extremely large workpieces but can improve the production time of smaller parts. Unlike conventional machining, no material is removed, so production time is a function of part volume rather than the difference in volume between the stock material and the final part. Conventional machining also has limitations in part geometry and material hardness due to the intrinsic nature of the tools used that are not present in AM. Harder workpiece materials will quickly wear down conventional machining equipment. Furthermore, unlike casting, no mold or part-specific equipment is required for AM, which makes AM well suited to the production of unique or small-batch parts. The additive approach in which no material is removed also reduces the amount of waste material. During the conventional machining of titanium parts, as much as 95% of stock material can be removed in the form of machine chips and scrap and must be discarded[23,25]. The reduction in production time and waste material is beneficial to the cost and environmental impact of titanium manufacturing.

Titanium alloys are one of the most common classes of metals to manufacture by AM. Titanium is difficult to fabricate by conventional machining methods. Its high hardness, low thermal conductivity, and reactivity with common tooling materials slows down machining time and can make the fabrication cost ten times higher than that of equivalent aluminum processing[25]. Not only are conventional manufacturing methods unsuitable, but the benefits of AM happen to align well with the applications of titanium and its alloys. In aerospace, specialized parts of bespoke alloys are individually produced, allowing AM to be a relatively low-cost manufacturing method[10,26]. Aerospace parts can also benefit from low density space-filling mesh geometries that are unique to AM. For biomedical applications, AM allows the rapid production of implants that are customized to each patient's required geometry[13].

As an emergent metals manufacturing technology, AM has the potential to create unique alloys and microstructures. This design space is the frontier of modern titanium alloy design. Furthering the understanding of the interaction between AM processes and the resulting material facilitates the design of alloys that are lighter, stronger, cheaper, and safer than ever before. The implementation of these novel, optimized alloys can contribute to the development of a healthier and more environmental society.

1.4 Dissertation Content

This dissertation will discuss the additive manufacturing of titanium and titanium alloys and how the addition of soluted carbon affects the microstructure and mechanical properties. Three titanium alloys of different phase stability are used as the base material, and up to 0.2 wt.% carbon will be added to each alloy in the form of titanium carbide (TiC). The base alloys, in order of increasing β-phase stability, are CP-Ti, Ti64, and Ti – 10 wt.% Mo. Each alloy will be produced by laser powder bed fusion (L-PBF) and thoroughly characterized.

The following statements will be proven using these alloys. A stable super-saturated carbon solid solution can be created by using L-PBF. Heat treatment can be effectively used to remove any embrittling artefacts of L-PBF without disrupting the carbon solid solution. The addition of carbon increases the strength of an alloy via the solid solution strengthening effect, and no embrittlement can be observed at a carbon content of 0.1 wt.% or less. Carbon is most effective at strengthening CP-Ti and least effective at strengthening duplex α-β phase microstructures, which are highly resistant to variance in mechanical properties from increased carbon content.

The layout of the remainder of this dissertation is as follows:

Chapter 2 is the literature review. It discusses the background and current state of research for titanium and its alloys, L-PBF and additive manufacturing as a whole, and interstitial strengthening of titanium.

Chapter 3 describes the methods and equipment used in this study. Procedures and common parameters are detailed for reference.

Chapter 4 concerns preliminary investigations into the effect of carbon addition on CP-Ti after heat treatment with regard to microstructure and mechanical properties.

Chapter 5 concerns the effect of carbon addition on Ti64 before and after heat treatment with regard to microstructure and mechanical properties.

Chapter 6 concerns L-PBF production of Ti – 10 wt.% Mo and the effect of carbon thereupon. Process parameters and heat treatments are optimized and explored. The impact of the various parameters on microstructure and mechanical properties are investigated.

Chapter 7 includes a summary of significant findings, recommendations for future research, and concluding remarks.

Chapter 2:
Literature Review

2.1 Materials

2.1.1 Pure Titanium

Titanium is a metallic element. It has the atomic number of 22, with an average atomic mass of 47.867 atomic units. It has an atomic radius of 1.42 Å and a density of 4.51 g/mm^3. The melting temperature of pure titanium is 1670°C. As a crystalline solid, titanium has two equilibrium crystal structures and three common metastable crystal structures.

At room temperature, titanium has a hexagonal close packed (HCP) crystal structure, denoted as the α-phase. The geometry of the α-phase has a space group of $P6_3/mmc$ and can be fully defined by two lattice parameters, *a* and *c* (Fig. 2.1a). Titanium has been measured to have an *a* value of 2.95 Å and a *c* value of 4.68 Å at room temperature[27]. The *c/a* ratio is therefore 1.59, which is lower than the ideal HCP *c/a* ratio of 1.63. The α-phase has a bulk modulus of 113 GPa and a linear elastic modulus of 155 GPa[28]. The thermal expansion coefficients are 9.5×10^{-6} °C^{-1} along the *a*-axes and 5.6×10^{-6} °C^{-1} along the *c*-axis[29].

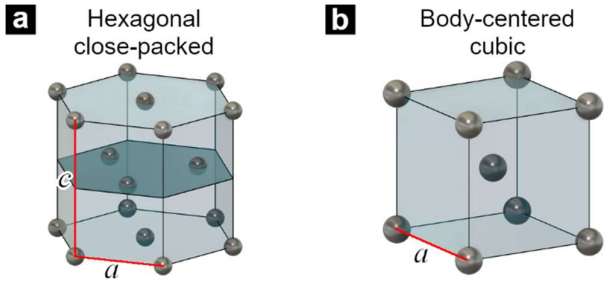

Figure 2.1: Crystal structures. a) HCP, b) BCC.

There are three named planes in an HCP system. The basal plane has hexagonal symmetry, Miller indices of {0001}, and a surface energy of 1.975 J/m^2. The prismatic plane has rectangular symmetry, Miller indices of $\{1\bar{1}00\}$, and a surface energy of 2.013 J/m^2. The first order pyramidal plane has rectangular symmetry, Miller indices of $\{1\bar{1}01\}$, and a surface energy of 1.921 J/m^2. The $\{11\bar{2}0\}$ plane has the lowest surface energy of 1.887 J/m^2.

At temperatures above 882°C but below the melting temperature, titanium exhibits the base centered cubic (BCC) crystal structure, denoted as the β-phase (Fig. 2.1b). The BCC phase has the space group of $Im\bar{3}m$, which is defined by only one lattice constant of *a*. The β-phase is unstable at low temperatures but is extrapolated to have a lattice constant of 3.28 Å at room temperature[30]. The β-phase has a bulk modulus of 105 GPa and a shear modulus of 13 GPa[28]. The thermal expansion coefficients are 9.5×10^{-6} °C^{-1} along the *a*-axes and 5.6×10^{-6} °C^{-1} along the *c*-axis[29].

Two of the metastable crystal structures are martensitic in nature. The first martensitic phase, α′, has an HCP crystal structure, while the second martensitic phase, α″, has an orthorhombic crystal structure. While the cooling rate is slow, the β→α transformation takes time to occur via nucleation and growth mechanisms. When the cooling rate is sufficiently faster than the β to α transformation, the β-phase is undercooled significantly and becomes unstable. The instability of undercooled β-phase makes martensitic transformations to metastable phases energetically favorable, allowing them to occur. Martensitic transformations are characterized by a uniform "shuffle" of crystallographic planes to change crystal structures (Fig. 2.2). These transformations occur when the high temperature β-phase is rapidly cooled.

Both types of martensite maintain the same orientation relationship with the β-phase. The invariant plane is $(011)_\beta$, which becomes $\{0001\}_{\alpha'}$ or $\{001\}_{\alpha''}$. These planes relax to $\{0001\}_\alpha$. The invariant direction is $[11\bar{1}]_\beta$, which becomes $\{11\bar{2}0\}_{\alpha'}$ or $\{110\}_{\alpha''}$ and relaxes to $\{11\bar{2}0\}_\alpha$[31]. In the martensitic transformation, alternating invariant $(011)_\beta$ planes shuffle in the $[110]_\beta$ direction. If the shuffle distance is equal to $\frac{\sqrt{2}}{6}a_\beta$, HCP symmetry can be achieved

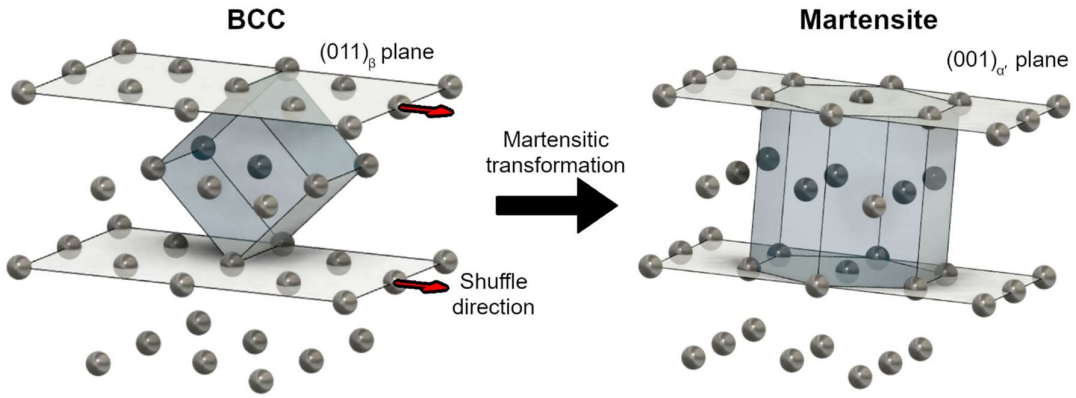

Figure 2.2: The martensitic transformation of titanium.

through lattice relaxation in the $[101]_\beta$ direction, yielding the α′. In the α″ transformation, the shuffle distance is less than $\frac{\sqrt{2}}{6}a_\beta$, so HCP symmetry is not achieved, and the crystal is orthorhombic[32].

The last metastable phase is the ω-phase. The ω-phase has a hexagonal ($P6_3/mmm$) or orthorhombic crystal structure. The lattice constants for the hexagonal crystal are 4.57 Å for *a* and 2.83 Å for *c*[28]. The ω-phase can form either isothermally or athermally. The ω-phase is not an equilibrium phase under ambient conditions but may be the equilibrium phase at high pressures above 2 GPa[33]. Despite its metastability, the ω-phase can have a high nucleation rate at certain temperatures, leading ω-phase nano-precipitates to develop in some titanium alloys.

Commercially pure titanium (CP-Ti) has four primary grades. They are denoted as ASTM Grades 1-4 for titanium[34]. They are distinguished primarily by their oxygen content, with Grade 1 having the lowest oxygen content and Grade 4 having the highest maximum oxygen content. The maximum oxygen content as well as the minimum mechanical specifications are tabulated in Table 2.1. Unless specified otherwise, all following composition percentages will be in weight percent.

Table 2.1: ASTM standards for CP-Ti.

Grade	Max. Oxygen Content [wt.%]	Min. Yield Strength [MPa]	Min. Ultimate Tensile Strength [MPa]	Min. Ductility [%]
1	0.18	138	240	24
2	0.25	275	345	20
3	0.35	380	450	18
4	0.40	483	550	15

CP-Ti deforms primarily through dislocation slip and twinning. The known slip systems for α-phase titanium involve *a*-type dislocations, which have a Burgers' vector in a $[1\bar{1}00]$ direction, or *a*+*c* type dislocations, which have a Burgers' vector in a $[1\bar{1}01]$ direction. The *a*-type screw dislocations are the most common type of dislocation. They can slip along the basal {0001}, prismatic $\{1\bar{1}00\}$, or first order pyramidal $\{1\bar{1}01\}$ planes (Fig. 2.3). The *a*+c type screw dislocations can slip along these planes. Twinning in CP-Ti is known to occur in tension along the $\{10\bar{1}2\}$ habit plane or in compression along the $\{11\bar{2}2\}$ habit plane[35,36].

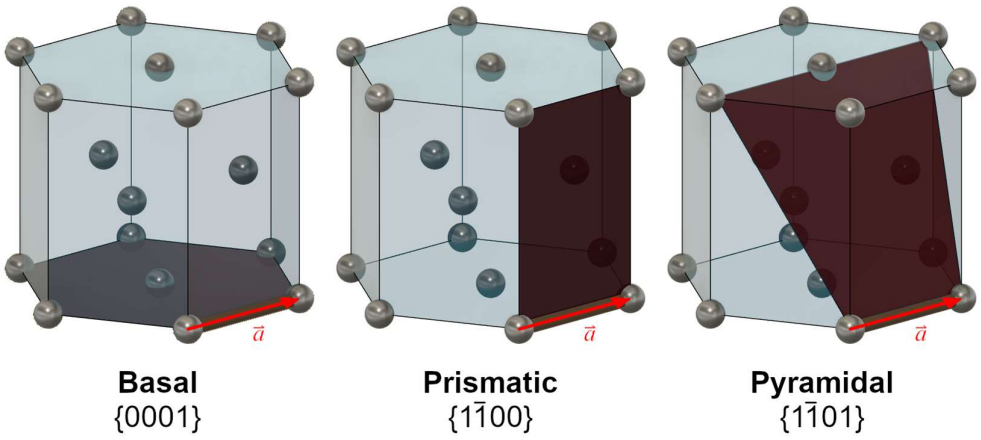

Figure 2.3: Slip planes in the α-phase.

2.1.2 Ti64

Ti-6Al-4V, or Ti64, is by far the most common alloy of titanium. It is composed of 6% aluminum, 4% vanadium, and 90% titanium. Ti64 is also known as ASTM standard Grade 5 titanium, although it may also be compliant with Grade 23 in cases of extra low interstitial content with less than 0.13% oxygen[34]. The addition of aluminum and vanadium dramatically increase the strength of the alloy, allowing titanium to be used in applications with high mechanical demands. However, high intrinsic strength can also by a drawback by reducing machinability and ductility[37]. The near ubiquity of Ti64 across the titanium industry has let it become both a reference standard for mechanical performance as well as a feedstock material for new alloy design[38].

Ti64 is a duplex α+β titanium alloy, with a room temperature phase fraction of 95.9% α-phase and 4.1% β-phase. The α-phase is stabilized by aluminum and has a room temperature equilibrium composition of 93.7% Ti, 6.3% Al, and 1.1×10^{-5}% V. The β-phase is stabilized by vanadium and has a room temperature equilibrium composition of 2.6% Ti, 3.3×10^{-2}% Al, and 97.4% Ti. Compositions were determined using the PANDAT calculated phase diagram software. Ti64 has a measured linear coefficient of thermal expansion of 8.5×10^{-6} °C^{-1} from room temperature to 980°C, which is the measured β transus temperature[39].

Ti64 is the standard for high-strength titanium alloys. The minimum mechanical specifications of Grade 5 titanium are a yield strength of 828 MPa, an ultimate tensile strength (UTS) of 895 MPa, and a ductility of 10%. The true mechanical properties are highly dependent on microstructure and thermal history. By optimizing traditional manufacturing methods, tensile yield strengths of up to 1000 MPa and ductility of 16% can be achieved in Ti64[5]. In compression, yield stresses of 1100-1250 MPa and a maximum true stress of 40% have been reported[40].

Ti64 does not deform uniformly. The β-phase is much softer than the α-phase and will deform preferentially in the duplex microstructure[41]. However, Ti64 is often implemented in primarily α-phase microstructures, so it is critical to understand the deformation of the α-phase. Like CP-Ti, the α-phase in Ti64 has been observed to deform by basal, prismatic, and pyramidal slip of *a*-type dislocations[42]. At room temperature prismatic slip is the dominant slip system, although significant basal slip can be observed at 450°C[43]. Above 550°C, the pyramidal slip system will activate as well[44]. The increase in active slip systems at elevated temperature is reflected in the mechanical performance, begins to deteriorate rapidly at temperatures above 500°C[45]. Twinning along the $\{10\bar{1}2\}$ habit plane has also been detected in deformed Ti64, particularly at higher strain rates[46].

The Hall-Petch equation can be used to predict the mechanical performance of a material from its grain size:

$$\Delta\boldsymbol{\sigma}_{\mathbf{y}}^{\mathbf{HP}} = \boldsymbol{k}_{\mathbf{HP}}\,\bar{\boldsymbol{d}}^{\mathbf{-1/2}} \tag{2.1}$$

Where $\Delta\sigma_y^{HP}$ is the increment in yield stress from the Hall-Petch effect, k_{HP} is the Hall-Petch coefficient, and $\bar{d}$ is the average grain diameter. For room temperature Ti64, k_{HP} has been reported to vary between 628 and 737 $\mu m^{-1/2}$MPa based on grain morphology and β-phase fraction[47]. The variance of the Hall-Petch coefficient is because the model assumes uniform, single-phase grains with a low aspect ratio and isotropic orientation, which is not always the case for Ti64. The duplex phase nature of Ti64 as well as its predilection to form in preferred textures and grain morphologies have led to the development of more modern techniques for predicting mechanical properties[48].

As the mechanical performance of Ti64 is highly dependent on its microstructure, a number of heat treatments for microstructural control have been developed. When heated above the β-transus temperature, Ti64 will quickly develop a fully β-phase microstructure, which is not stable at room temperature. Therefore, the cooling rate, which governs the activity of phase transformations, is the primary determining factor of the post-heat-treatment room temperature microstructure. Ti64 experiences a martensitic transformation of β→α′ when cooling rates are 10°C/s or faster but will decompose through nucleation and growth mechanisms into a duplex α-β microstructure at slower cooling rates[49,50]. The martensitic transformation starts to occur below 850°C and finishes by 720°C[50]. A full continuous cooling transformation (CCT) diagram can be seen in Fig. 2.4.

In heat treatments at sub-β-transus temperatures, grain growth and diffusion govern the change in microstructure. Grain growth in Ti64 is much slower than in CP-Ti because addition of vanadium and aluminum dramatically leads to the solute drag effect[51]. With solute drag, the grain growth rate is limited by the diffusion rate because the different solute elements must be partitioned by diffusion into different phases. The slow grain growth rate allows fine microstructures like martensitic lamella (also known as the Widmanstätten microstructure) to

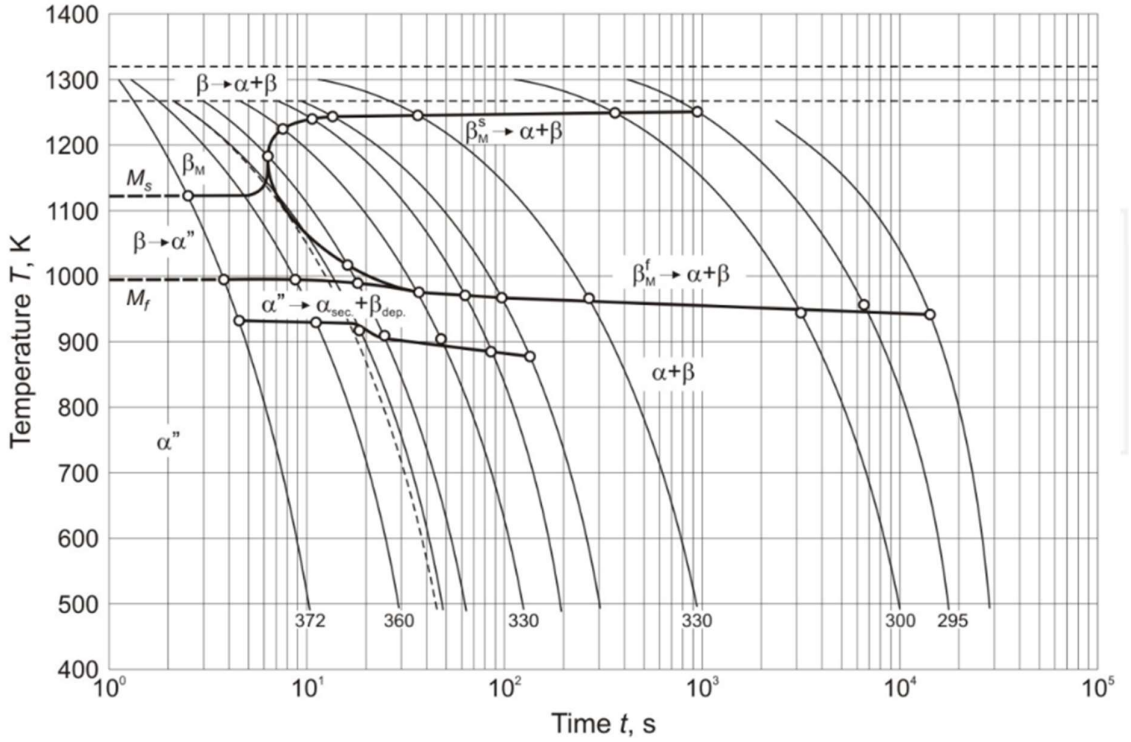

Figure 2.4: A continuous cooling transformation map for Ti64[50].

be retained over the course of a heat treatment[51]. It must also be noted that any heat treatment above the martensitic finish temperature can still develop martensite from β-phase regions during rapid cooling[52].

2.1.3 Near-β alloys

With the addition of enough β-stabilizing elements, fully β-phase titanium alloys can be realized. Iron, chromium, molybdenum, vanadium, and niobium are commonly used to stabilize the β-phase[53]. For multi-component alloys, a molybdenum equivalent Mo_{EQ} is usually used to refer to β-phase stability[54]. An alloy is generally considered "fully β" at a Mo_{EQ} of at least 10%[3]. However, in this context, fully β does not refer to the equilibrium phase composition of the alloy. In fact, the calculated binary Ti-Mo phase stability states that over 80% Mo is required for an alloy that is fully β-phase at room temperature equilibrium[55]. While the equilibrium conditions suggest that alloys with 0.1%-80% Mo_{EQ} alloy are duplex, the kinetics often prevent equilibrium conditions from being achieved. This leads to three categorizations of β stabilized Ti alloys: duplex α-β alloys, near-β alloys, and stable β alloys[3]. Near-β alloys, or metastable-β alloys, have Mo_{EQ} values slightly above 10% and are characterized by being able to exhibit a fully β or duplex α-β microstructure depending on thermal history.

The metastability of the β-phase in near-β alloys leads to a variety of non-equilibrium microstructures. Depending on the heat treatment and composition, α′ martensite, α″ martensite, and ω precipitates can occur[56]. In alloys with low β-phase stability, like Ti64, α′ martensite forms upon rapid cooling. In near-β alloys, α″ martensite and ω precipitates are more common, with ω occurring more frequently at higher Mo_{EQ} concentrations[3,32]. The transition from α′ martensite to α″ martensite occurs because the shuffle of $(011)_\beta$ planes is suppressed by β-phase stabilizing elements. In the β→α′ transformation, the shuffle distance is equal to exactly $\frac{\sqrt{2}}{6}a_\beta$. At a critical concentration of β-stabilizers, the planes are inhibited from shuffling the full distance, so α″ is formed instead. First principles calculations of the Ti-V system show that the shuffle distance is constant in the β→α′ transformation but has an inverse relationship with the concentration of V in the β→α″ transformation [57]. Study of the Ti-Nb system shows that the lattice parameters of α″ are also dependent on β-stabilizer concentration, with Nb reducing the *c/a* ratio[58]. The onset of the martensitic transformation is dependent on both composition and cooling rate. The addition of β-phase stabilizing elements reduces the driving force for the β→α′ or β→α″ transformation, lowering the martensite starting temperature[59,60].

The ω-phase can form isothermally by nucleation and growth or athermally by a shear distortion of the β-phase[61]. It can form within a β-phase grain, at grain boundaries, or together with α″-martensite to accommodate shear[62]. The ω-phase nucleates quickly but does not grow quickly, so it usually takes the form of nano-precipitates within the β-phase matrix[63]. The small scale of the grains makes the ω-phase difficult to detect without advanced microscopy techniques[61,64].

The ω-phase is well known for its adverse effect on the mechanical properties of near-β alloys. The β-phase of Ti has a lower elastic modulus than the α-phase, so near-β alloys are often implemented in low elastic modulus applications such as bone implants[3,28]. Precipitated ω-phase increases the elastic modulus, reversing the advantages gained by using β-phase alloys and reducing its effectiveness[65,66]. Furthermore, large amounts of ω-phase can severely embrittle β-phase titanium alloys to the point where no plastic deformation can occur[67]. The disadvantages of the ω-phase have made controlling ω-phase development a key part of β-phase Ti alloy design and processing.

When carefully controlled, ω precipitates can provide mechanical benefits. The strength of fully β-phase titanium alloys can be very low due to the high symmetry of the BCC crystal structure, so precipitation hardening can effectively improve mechanical performance. This is particularly effective in compressive applications, where crack resistance and toughness are less important[68]. The morphology of ω precipitates is controlled by heat treatment. Classical heat treatment of a near-β alloy first involves a solution treatment of up to 2 h above the β-transus temperature to chemically homogenize the alloy before quenching. When high strength is required, the alloy is then “aged” between room temperature and 700°C for anywhere from

minutes to months until the desired precipitate structure forms[63,64,69]. In duplex aging techniques, aging involves two stages: a low temperature primary heat treatment of 300-500°C to nucleate ω precipitates and a high temperature secondary heat treatment of 450-700°C to coarsen the precipitates and relax them to α-phase[68,70]. A cold working step can also be added in before aging where the alloy is mechanically deformed to promote precipitate formation and recrystallization[71]. When properly heat treated, aged β-phase alloys can have mechanical properties equivalent or superior to Ti64[3,67].

2.1.4 Ti-Mo

The Ti-Mo binary system is a fundamental system to near-β alloy design. As β-stabilizers are compared to molybdenum using the molybdenum equivalent , understanding how molybdenum functions when alloyed into titanium is a fundamental problem for β-phase alloy design.

The binary phase diagram for the Ti-Mo system can be seen in Fig. 2.5[55]. There are no intermetallic compounds, and both elements are completely soluble in the BCC β-Ti phase at high temperatures across all compositions. There is a miscibility gap in the β-phase with a peak at 850°C and a composition of 50% Ti. Mo has very low solubility in the α-phase of titanium, being almost completely insoluble at room temperature. The two-phase α-β region occurs up to 695°C, and there is a eutectoid point at 18% Mo.

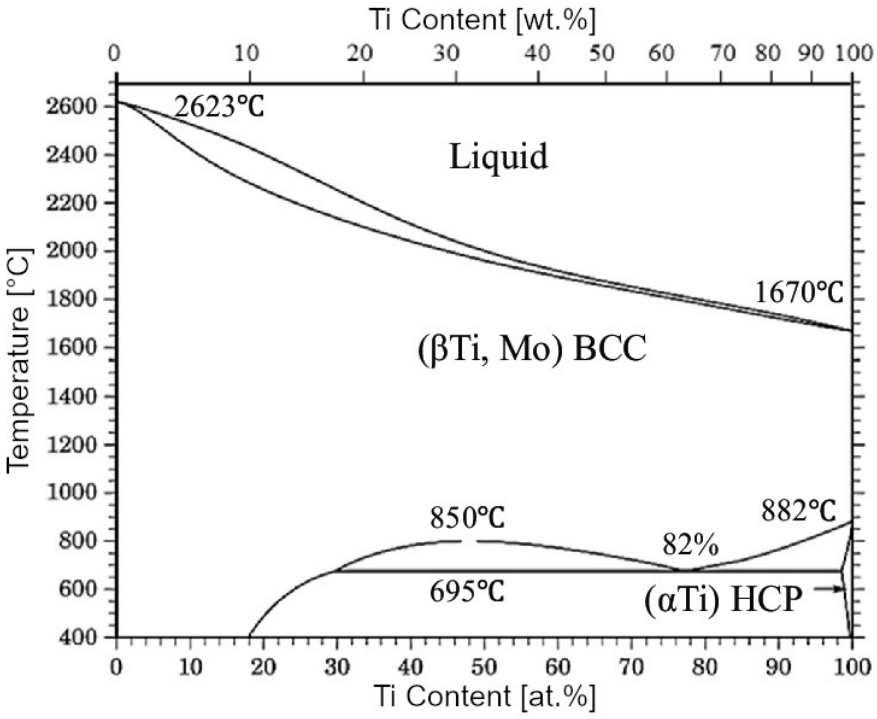

Figure 2.5: The binary Ti-Mo phase diagram[55].

All five of the aforementioned phases can be observed in the Ti-Mo system. In as-cast alloys, martensitic laths can be observed by optical microscopy at compositions of 9% Mo or less[72,73]. The laths are α′ martensite up to a composition of 6% Mo, and α″ at higher Mo concentrations[73]. The α″ martensitic transformation occurs readily at Mo concentrations of up to 9%, but ω precipitates are more common than α″ laths at Mo concentrations above 9%[74]. The ω-phase in the Ti-Mo system has been determined to have orthorhombic symmetry[74,75]. Molybdenum is not stable in the ω-phase and will be preferentially excluded from ω precipitates[76].

Alloys of Ti and Mo can deform via any combination of dislocation slip, twinning induced plasticity (TWIP), and transformation induced plasticity (TRIP)[77–79]. In TWIP, the β-phase deforms through the creation of {332}(113) twins[80,81]. In TRIP, the β-phase deforms via the shear caused by a martensitic transformation[82,83]. This tends to occur when the β-phase is extremely unstable and the martensitic start temperature is close to room temperature[84,85]. TRIP and TWIP deformation modes are most common in microstructures with a β-phase fraction close to 100%, as they are inhibited by the ω-phase[86].

The reported mechanical properties of the Ti-Mo system are as follows. The Hall-Petch coefficient of Ti-15Mo deforming by TWIP was determined to be 1112 $\mu m^{1/2}MPa$[87]. The elastic modulus was found to decrease with increasing molybdenum content up to 13% Mo, where the elastic modulus is 80 GPa[88]. Solution treated Ti-12%Mo has shown a low tensile yield strength of 480 MPa and a ductility of over 40% true strain, but the strength improved by ω-phase precipitation to 730 MPa when aged for 60 s at 150°C[89]. Solution treated Ti-11%Mo has shown a tensile yield strength of 800 MPa and a ductility of 70%, and the strength gradually improved to 1300 MPa while the ductility gradually reduced to 0% when aged for 200 h at 350°C[67].

2.1.5 TiC

The last material used in this study, titanium carbide, is a ceramic. It has a rock salt cubic crystal structure with a space group of $Fm\bar{3}m$[90]. The single lattice parameter *a* has a length of 4.33 Å. It has a bulk modulus of 253 GPa and a linear elastic modulus of 425 GPa [28]. TiC solidifying from a melt has been documented as growing near-spherically or along the close packed {111} facets[91].

2.2 Additive Manufacturing

2.2.1 An Introduction to Additive Manufacturing

Additive manufacturing, commonly referred to as 3D printing, can be defined as a manufacturing technique in which feedstock material is incrementally added to the workpiece. This can be contrasted with traditional methods of subtractive manufacturing, like machining and tooling, in which material is removed from the workpiece, or consolidative methods, like

casting, in which the workpiece is produced uniformly from the feedstock. The general principles of additive manufacturing are not a new technology; bricklayers have been additively generating structures for millennia. However, the ability to motorize and automate additive processes has led to an explosion of additive technologies over the past 40 years. Producers can design the geometry of the part they desire, input that geometry into a computer, and then the part is manufactured with minimal manual operation of the machine by the producer.

Modern additive manufacturing (AM) of metallic materials is usually traced back to C. R. Deckard's work at the University of Texas, Austin[92]. There, he designed a "selective laser sintering" technique for polymers, where a part was built up layer by layer through the fusion of feedstock powder by a laser. This technique was soon extrapolated to metallic materials, where it became known as selective laser melting[93]. From there, a suite of metallic additive techniques were developed.

The advantages of metallic AM are in both the geometry and the material. Many geometries that are straightforward to manufacture additively cannot be manufactured by traditional methods. For example, a 3D-mesh or gyroid space-filling structure can dramatically reduce the weight of a part but is nearly impossible to manufacture using traditional methods without a many-part assembly (Fig. 2.6). With additive methods, the manufacturing time is a function of part volume and independent of geometric complexity, making AM the most efficient way to manufacture highly complex parts[94]. Furthermore, no material is removed from the workpiece during AM, which has the potential to dramatically reduce cost and waste. With expensive alloys, only the amount needed for the part itself need be purchased, rather than larger stock geometries that will be shaped through subtractive methods. The reduction in waste material also reduces the cost of recycling or the environmental impact of disposal.

In some high-performance alloys, it is not the material cost but the manufacturing cost that is reduced by AM techniques. The most notable of these are titanium and nickel-based alloys, which have high strength but low elastic moduli, making them difficult and slow to

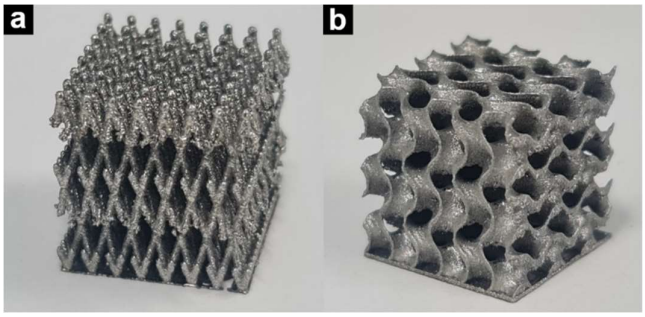

Figure 2.6: Unique additively manufactured structures: a) mesh, b) gyroid. Samples were manufactured using L-PBF by Ammarueda Issariyapat.

machine conventionally. These properties do not affect AM, making titanium and nickel systems amongst the most popular classes of alloys for AM[95,96].

AM can enhance or reduce the desired mechanical properties of metals. Most metallic AM techniques consist of localized heating and melting of the metal followed by rapid cooling and solidification[95]. The layer-by-layer construction of AM parts also causes a cyclic heating of each point as the layers immediately above it are heated and cooled[97,98]. This unusual thermal profile can give rise to fine microstructures that are unique to AM and often have higher strength than their conventionally manufactured counterparts[99,100]. When a metal is locally heated and cooled quickly and inhomogeneously, there is an imbalance between thermal expansion and geometric constraints. For example, a locally heated melt pool will solidify at high temperature in geometric coherency with the surrounding cool material. However, as the prior melt pool cools down to room temperature, it contracts due to thermal expansion. The surrounding material was not heated as much, so it does not contract as much. The inhomogeneous thermal expansion and contraction can lead to high residual stresses in as-printed materials, potentially causing localized plastic deformation or embrittlement. Residual stresses can also affect the dimensional stability of the as-printed part, causing them to deform when polished or removed from the printing substrate[101–103]. Residual stresses can be readily reduced or removed through simple heat treatment[104].

The final advantage of AM is not related to the production of parts at all, but instead alloy design. While 3D printing is known for its rapid prototyping of geometries, it also can rapidly prototype alloys. In most metallic AM techniques, the feedstock material is a fine metal powder that gets melted. If the feedstock powder is composed of multiple component powders, they will be melted and alloyed in-situ[105]. In-situ alloying of pre-mixed powder allows for rapid production of new alloys with tightly controlled composition. Determining efficacy of additive manufacturing for rapid alloy design will be left to the discretion of the reader as they continue through this dissertation.

2.2.2 Types of Additive Manufacturing

The two most common types of AM for the production of metallic materials are direct energy deposition (DED) and powder bed fusion (PBF). Due to the recent development of these technologies and continuous development of additional types, the naming conventions are not well standardized. DED includes the technologies known as laser metal deposition (LMD), direct metal deposition (DMD), laser engineered net shaping (LENS), and wire arc additive manufacturing (WAAM). PBF includes the technologies known as selective laser melting (SLM), laser beam melting (LBM), direct metal laser sintering (DMLS), or laser metal fusion (LMF).

In DED, feedstock metal is deposited directly into the melt pool from an external source. In most cases, the feedstock metal is a fine powder, and the melt pool is generated by a laser. A DED machine of this type involves a laser and powder-spraying nozzle attached to a robotic arm and a powder hopper connected to the nozzle. For reactive metals, an inert cover gas can be dispersed locally at the melt pool or throughout the build chamber. Due to the mobility of the powder source and laser, no specific build chamber is required. DED geometry is only limited by the range of motion of its robotic arm, making it the most scalable and geometrically diverse AM method.

In most DED, the feedstock powder is mechanically sprayed into the melt pool through the nozzle. The geometry of the powder spray is limited by the nozzle design and can have quite a large area of incidence with the workpiece. DED is therefore characterized by having relatively large melt pools and track widths. The advantage of large melt pools is that DED can create larger structures very quickly, but at the cost of lower geometric precision and a larger minimum feature size. The large melt pools also cool relatively slowly, reducing residual stress formation but also leading to more conventional microstructures. DED materials often have good ductility as-printed, reducing the need for a post-processing heat treatment[106]. Another advantage of a hopper-fed powder source is that powders can be mixed in-situ through the use of multiple hoppers with different component powders. With in-situ powder mixing, the relative volume fraction of each component powder can be adjusted during the printing process. By smoothly changing feedstock powder composition over the course of the print, functionally graded materials can be successfully created[107–110]. Functionally graded materials can also be created by more exotic types of DED, such as wire-fed methods[111].

In PBF, an incident heating beam rasters across the surface of a bed of feedstock powder, welding the surface layer together in a specific pattern. The powder bed and substrate are then lowered and recoated with a new layer of fresh powder, and the process begins again (Fig. 2.7).

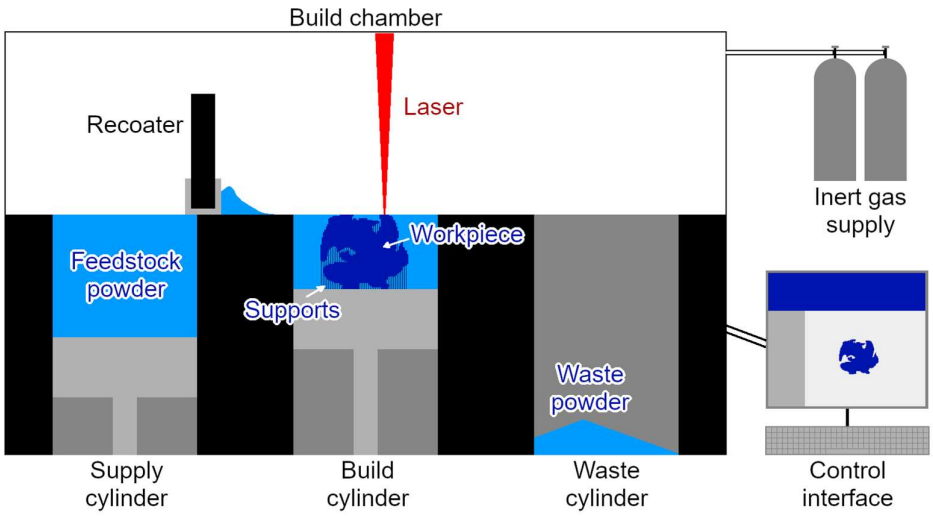

Figure 2.7 Schematic of the L-PBF process.

The part can either be printed directly onto a substrate or on thin support structures that can easily be removed during post-processing[112]. When fusion is finished, the part is removed from the powder bed and excess powder is reused[113]. Powder bed fusion can use either an electron beam (E-PBF) or laser (L-PBF) as its heat source. Electron beams have higher penetration depth than lasers, leading to larger melt pools and more uniform heating and cooling. E-PBF generally has larger grains and less residual stress than L-PBF.

L-PBF is the preferred AM technique for small, highly detailed parts. The workpiece dimensions are limited by the size of the powder bed, preventing the production of massive parts. The melt pool size is on the order of 10s to 100s of microns, so detailed features can be achieved. Because of the small melt pool size, L-PBF has the fastest cooling rate of any of the discussed AM techniques, which can yield unique microstructures but has high residual stresses.

2.2.3 L-PBF Parameters

L-PBF is highly sensitive to the process parameters, of which there are several. Some of the more common process parameters are listed in Tables 2.2 and 2.3, along with a basic description of the property most affected by each process parameter.

The feedstock powder primarily affects the composition and density of the part. First and foremost, the material composition of the powder governs the material composition of the part. There may be slight compositional changes during printing due to vaporization in the melt pool or absorption of the atmosphere or substrate for alloys with high chemical reactivity, but for the most part the material input determines the material output. When multiple powders are used for in-situ alloying, the particle size is important for homogeneity. Homogeneity is improved by smaller powder particles and a well-mixed powder[114]. The shape and size

Table 2.2: Material parameters.

Category	Parameter	Primary affected property
Phase	Melting temperature	Heat flow
	Heat of fusion	Heat flow
	Phase stability	Phase transformations
Thermal	Laser absorptivity	Heat flow
	Thermal conductivity	Heat flow
	Thermal expansion	Residual stresses
Chemical	Reactivity	Part composition

Table 2.3: L-PBF parameters.

Category	Parameter	Primary effect
Powder	Powder composition	Part composition
	Powder flowability	Part density
	Powder shape	Part density
	Powder size	Part density, chemical homogeneity
	Powder density	Heat flow
Laser	Wavelength	Laser absorption
	Power	Heat flow, solidification
	Spot size	Laser absorption
Scanning	Scan speed	Heat flow, solidification
	Hatch distance	Heat flow, density
	Layer thickness	Heat flow, density
	Layer time	Heat flow
	Scan pattern	Residual stresses
Part geometry	Wall thickness	Heat flow
	Build angle	Part stability
	z-height	Heat flow
Substrate	Substrate material	Heat flow
	Substrate temperature	Heat flow
	Substrate size	Heat flow
Supports	Support size	Heat flow
	Support shape	Part stability
	Support laser conditions	Support removal
Ambient	Temperature	Heat flow
	Humidity	Part density
	Atmosphere	Part composition

distribution of the powder determines flowability which in turn affects part density. If the powder has low flowability, recoating is less reliable and thickness variations or even gaps in the powder bed can develop, reducing density. High ambient humidity can promote particle adhesion and reduce flowability as well.

Input of heat into the system is controlled by the laser itself. Laser power is the most important laser parameter, as it governs the rate at which energy is being introduced into the material. However, not all of that energy is absorbed. It is important to select a laser with a wavelength that will be efficiently absorbed by the powder and not reflected. For example, near infrared (NIR) lasers are well absorbed by titanium but not by copper. Powder morphology can also affect laser absorptivity, with rougher and smaller particles having higher absorptivity.

The geometry of the melt pool is tunable through the laser power P and laser scan speed v. Together, they can be used to define a composite linear energy density (LED) parameter:

$$LED = \frac{P}{v} \tag{2.2}$$

The melt pool is defined as the region of liquid metal created by the laser at any given instant. Increasing the LED increases the size of the melt pool in all directions, as well as the surrounding temperature gradient[115]. The high-temperature region around the melt pool induces a heat-affected zone (HAZ) in the surrounding material. There are two types of melt pool profiles: conduction and keyhole. Conduction-type profiles have an elliptical cross section and occur at low LED (Fig. 2.8a). Keyhole-type profiles have a double-elliptical cross section and occur at high LED (Fig. 2.8b). The keyhole effect occurs when the LED is high enough such that a region of air and vaporized metal is created in the laser's path. The absorptivity of this gaseous region is very low, so the laser can penetrate much farther, leading to deeper melt pools. If LED is too high, keyhole defects can develop[116]. Keyhole defects are round pores that form when part of the gaseous region remains trapped inside the material after solidification.

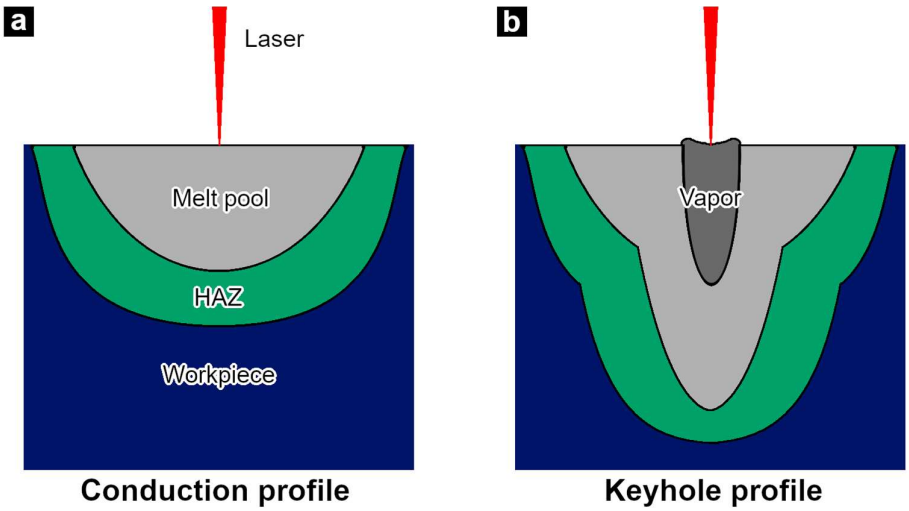

Figure 2.8: Melt pool cross sections of with a) conduction profile and b) keyhole profiles

Penetration depth can also be increased by preheating the material so that the differential between the ambient and melting temperatures is smaller and the laser can melt the material more easily[117]. In in-situ alloying, it is important to have a high LED so that there is sufficient energy to mix the melted powders and achieve good homogeneity[118].

The scan strategy can be used to manipulate residual stresses. While any space-filling pattern is possible, linear patterns where the laser rasters back and forth over the area are the most popular because they are easy to program and actuate. A purely linear scan strategy in one orientation over all layers will lead to the accumulation of residual stresses, particularly along the scan direction[103]. The residual stresses can be reduced by rotating every layer by 90° to distribute the stresses over multiple directions. Residual stress can be reduced even further by using an island scan strategy[103,119]. In island scan strategies, small regions, or "islands", are melted then allowed to cool before the neighboring regions are melted. The island scan strategy allows for a more even temperature distribution, reducing large differences in thermal expansion and consequently residual stresses. The most common island scan strategy is the "chessboard" strategy, where each island is a square with a scan direction rotated 90° to all four adjacent squares.

Most of the remaining parameters govern heat flow. With a multi-faceted system like L-PBF, the exact thermal history of each point can vary based on its surroundings. A layer printed directly onto a cold, dense substrate will experience faster cooling than a thin wall surrounded by low thermal conductivity powder. The effects of edge conditions and thin walls are outside the scope of this study. Instead, these thermal effects will be standardized by studying thick-walled regions that have reached steady state conditions.

Steady state thermal conditions of a single material are often summarized by four parameters: laser power P, laser scan speed v, hatch width h, and layer thickness t. Together they can create a single summary parameter, volumetric energy density (VED):

$$VED = \frac{P}{vht} \tag{2.3}$$

Volumetric energy density, which uses the units of J/mm^3, can be thought of as the amount of laser energy input into the system to make a unit volume. Prints with a high VED will often reach high steady-state temperatures and therefore have slower cooling rates. The VED parameter is particularly useful for predicting the densification of a part[120]. If VED is low, there is insufficient energy to melt all the powder, and lack-of-fusion defects will develop[116]. Lack-of-fusion defects are irregularly shaped voids in a printed material caused by unmelted powder particles being unable to completely pack together. These defects can be extremely detrimental to the mechanical performance of a material[121].

VED is the most useful single parameter to compare materials produced using different parameters[122]. However, density is rarely the only output variable being optimized, so a more comprehensive approach than comparing only a single parameter must be taken. Basic

optimization of print parameters usually involves the component parameters of VED: laser power, laser scan speed, and hatch width[123,124]. Research into these optimizations is ongoing, expanding the database of process parameter inputs and resulting material property outputs. With enough data points, the relationship between process parameters and printed properties will soon be understandable and optimizable by machine learning methods[125].

2.2.4 L-PBF Solidification

Each point of L-PBF begins as solid powder, is melted by the laser, then solidifies again. Melt pools are fairly turbulent, with surface tension and inhomogeneous heating driving Marangoni flow[117]. Solidification begins at the rear of the melt pool and the solidification direction is normal to the melt pool edge (Fig. 2.9)[126]. The two major transitions that govern solidification are the columnar-to-equiaxed transition (CET) and the oriented-to-misoriented transition (OMT).

The CET describes a change in solidified grain morphology from high aspect ratio to low aspect ratio by changing how new grains nucleate. Columnar grains occur when the boundary grains of the melt pool grow epitaxially into the melt pool, while equiaxed grains occur when there is continuous nucleation of new grains along the solidification front. Equiaxed grains are known to occur at low thermal gradients and high solidification velocities[127,128]. With low thermal gradients, the volume of supercooled melt ahead of the solidification front increases, increasing the chance that nucleation events will occur[129]. At high solidification velocities, the cooling rate is increased, which also promotes nucleation[130].

The OMT describes a change in crystal orientation from textured to untextured[131]. Every crystalline material has specific crystallographic orientations that will grow faster than others. Therefore, columnar materials that grow continuously in one direction will tend to have a preferred texture in the growth direction as grains with the fastest-growing orientations will

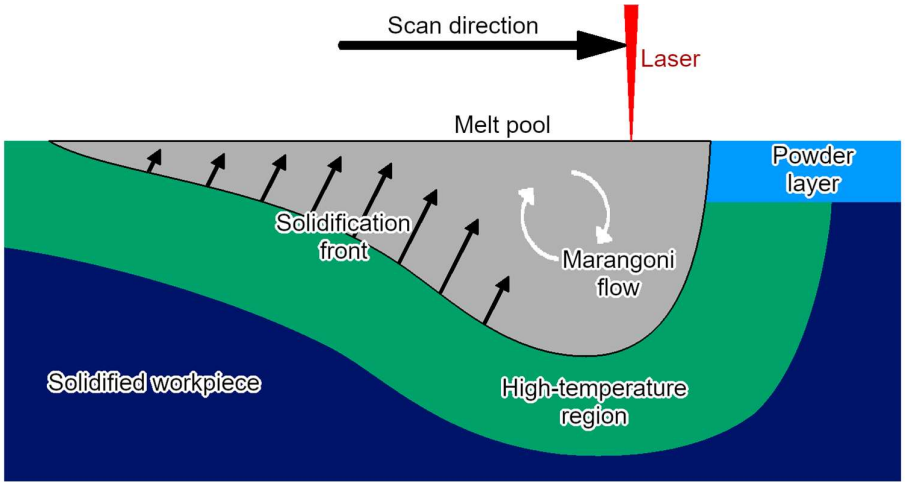

Figure 2.9: Anatomy of a melt pool.

outcompete misoriented grains[132]. In L-PBF materials, there can also be secondary textures in the scan directions[133]. The OMT and CET occur under similar conditions because equiaxed heterogeneous nucleation promotes misoriented grains. However, equiaxed but oriented grains have been reported[134].

The CET and OMT help determine the isotropy of the material. Columnar grains have a high aspect ratio in the solidification direction. Oriented grains will have their preferred orientation in the same direction. In L-PBF materials, that direction is the build direction, also commonly referred to as "up". L-PBF Ti64 printed under oriented, columnar conditions is consistently shown to solidify with preferred build direction orientation of $\{100\}_\beta$[135]. It then experiences a martensitic transformation $\beta \rightarrow \alpha'$ during cooling. Martensitic transformations preserve the texture of parent-β grain because they can only occur along fixed habit planes. Because of the fixed orientation of transformation, L-PBF Ti64 printed under oriented, columnar conditions has shown anisotropic mechanical properties. Tensile testing shows that tensile strength is slightly lower, but ductility is higher in the build direction than the transverse direction[136,137]. Fracture toughness is also anisotropic, with fracture along the build plane being reported as requiring half the energy of fracture along a vertical plane due to the delamination of build layers[138].

Many techniques for inducing the CET or OMT have been developed. Of course, print parameters that increase solidification velocity and reduce thermal gradient can be applied[127]. Additionally, ultrasound, re-melting of layers, distributing nucleation site powders, and scanning discontinuously have been shown to induce the CET or OMT[139–142].

Solidification can also be affected by the composition of melt pool. Congruent solidification, where the solid and liquid have the same equilibrium composition, only happens at very specific compositions, like perfectly pure titanium. In alloys, the melt and the solid have different equilibrium compositions. The phase segregation of component elements causes columnar grains to form dendritic structures with non-homogeneous compositions at low solidification rates[143]. At sufficiently fast solidification rates, such as those often seen in L-PBF, planar, diffusionless solidification can occur with complete solute trapping[143,144]. The dissipation of driving force Gibbs energy by diffusion, also known as the solute drag effect, suppresses nucleation of new grains[145].

2.2.5 Post-processing

As-printed L-PBF materials can have highly strained and defect-ridden microstructures, so post-processing is often the most efficient way to improve the performance of the material. The simplest post-processing technique is heat treatment. Heat treatment can lead to residual stress relief, dislocation annihilation, and grain growth, which lowers strength and increases ductility. This makes it particularly applicable in high-strength alloys like Ti64, which have

naturally low ductility. The heat treatment of Ti64 after SLM typically involves a heat treatment of 0.5 - 3 hours at between 700°C and the β-transus temperature to achieve good mechanical properties[104,146–148]. Hot isostatic pressing (HIP) can also be used to heat treat a material and improve its density at the same time[149].

Post-processing can also be used to manipulate isotropy. Residual stresses have preferred orientations, so basic heat treatment does improve mechanical isotropy[134]. However, crystallographic isotropy can also be improved. Heat treating of a DED titanium alloy with columnar and equiaxed regions has shown a reduction in texture via the preferential growth of equiaxed grains[150]. However, HIP has been the only way shown to change the texture of a fully columnar material[151].

2.3 Interstitial Strengthening

2.3.1 The Interstitials of Titanium

The four common elements that are interstitially soluble in titanium are hydrogen, carbon, nitrogen, and oxygen. Of these, carbon, nitrogen, and oxygen behave similarly. They are traditionally considered undesirable elements in titanium with embrittling effects[152]. The true relationship between the interstitial composition and mechanical performance of titanium is much more subtle and diverse.

Documenting the impact of these carbon, nitrogen, and oxygen in pure titanium began in the 1950s, where it was shown that they can increase strength at the cost of ductility[153,154]. Eventually, Ogden and Jaffee developed the oxygen equivalent O_{EQ} model[155]:

$$\boldsymbol{O_{EQ} = \frac{2}{3}[C] + 2[N] + [O]} \tag{2.4}$$

Where $[X]$ represents the concentration in wt.% of element X. The oxygen equivalent model postulates that the mechanical properties of titanium are a function of a linear combination of these three interstitial elements, with nitrogen having the strongest influence and carbon having the weakest. This work would be continued by H. Conrad, who considered interstitial mechanics the governing factor for HCP deformation dynamics[156]. He would go on to compile the most in-depth experimental quantification and summary of how the three interstitials affect every mechanical property of pure Ti[157]. Concurrently, a model for solid solution strengthening was developed by R. Labusch:

$$\boldsymbol{\tau_c b = \frac{[X]^{2/3} f_0^{4/3} w^{1/3}}{(4T)^{1/3}} C} \tag{2.5}$$

Where τ_c is the critical resolved shear stress, b is the Burgers length, $[X]$ is the solute concentration, w is the characteristic solute interaction distance, T is the line tension, and f_0 and C are non-dimensional parameters. This model states that the yield stress is proportional to the concentration of any dilute solute atom in an amount proportional to the concentration of that

solute to the two-thirds power as well as the amount of lattice distortion caused by that solute atom.

Modern first-principles simulation work has given more insight into the nature of interstitial carbon, nitrogen, and oxygen. All three elements are α-phase stabilizers. Within the α-phase, they are most stable in the octahedral void interstitial site (Fig. 2.10). In the octahedral site, carbon has the highest energy of formation and oxygen has the lowest[158]. The calculated formation energy trend is consistent with solubility, as oxygen is highly soluble in titanium whereas carbon is not. Soluted oxygen and nitrogen have been documented as increasing the *a* and *c* lattice parameters of the α-phase as well as the *c*/*a* ratio[159].

The interstitials can diffuse rapidly through titanium. The measured Arrhenius activation energies of diffusion for carbon, nitrogen, and oxygen through the α-phase are 130, 225, and 200 kJ/mol^{-1} respectively[160]. While nitrogen and oxygen have higher activation energies than carbon, unlike carbon they are metastable in hexahedral voids, allowing additional diffusional jump pathways[161]. Oxygen has been shown to be shunted into hexahedral voids during interaction with dislocation slip, potentially leading to slip plane softening[162].

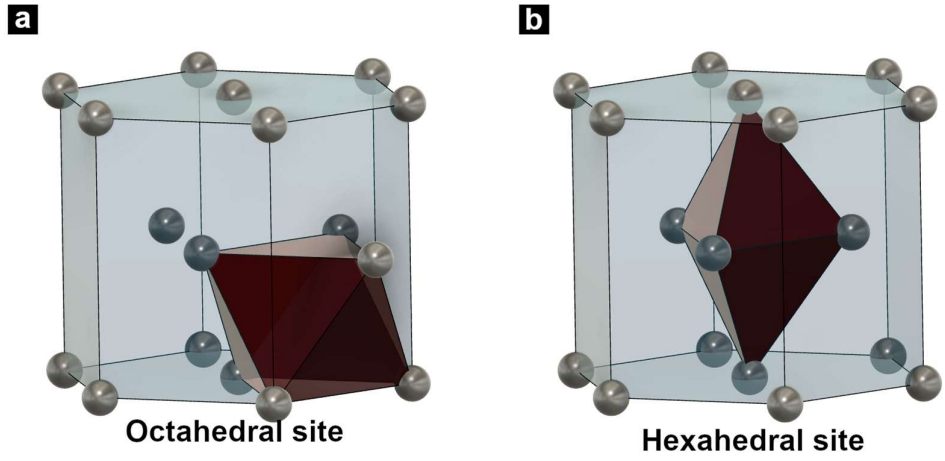

Figure 2.10: Common interstitial sites in an HCP crystal: a) octahedral, b) hexahedral.

2.3.2 Recent Work

While interstitial elements have classically been considered unwanted contaminants in titanium alloys, recent work has shown that nitrogen and oxygen can yield good improvements to mechanical performance when carefully controlled. Comparison of L-PBF CP-Ti shows that the as-printed strength increases with increasing grade number, which correlates with increasing oxygen content, at no cost to ductility up to Grade 3[163]. The L-PBF Grade 4 titanium did show signs of oxygen embrittlement but had high strength and reasonably good ductility. The grade system only shows a range of potential oxygen values for an individual titanium

sample, so techniques have been developed to reintroduce oxygen and also nitrogen back into high-purity titanium in exact quantities[164].

L-PBF is a popular method for the controlled reintroduction of interstitial elements into titanium because of the ease of in-situ alloying. Both nitrogen and oxygen can be introduced by printing under an atmosphere containing nitrogen and oxygen and allowing the atmosphere to react with the melt pool[165,166]. Oxygen can also be added into the feedstock powder in the form of intermixed TiO powder[167]. A technique for homogeneously disbursing nitrogen was developed by Issariyapat et al. in which CP-Ti powder was heated under a nitrogen-rich atmosphere before printing to preemptively nitrogenate the powder[168,169]. For both oxygen and nitrogen, strength and ductility were found to simultaneously increase with the addition of small amounts of interstitial solute before becoming embrittled at higher solute concentrations (Fig. 2.11).

While interstitial solid solution strengthening is the primary benefit of interstitial addition, it can also improve the phase stability of β-phase titanium alloys. The interstitials do preferentially stabilize the α-phase over the β-phase, but at low concentrations this effect is small. Most importantly, interstitials may inhibit the precipitation of the embrittling ω-phase. First principles calculations show that the energy barrier to the formation of ω-phase is increased significantly by the presence of an interstitial solute, with certain formation geometries being completely destabilized[170]. The suppression of ω-phase formation by oxygen has been confirmed experimentally as well[171,172].

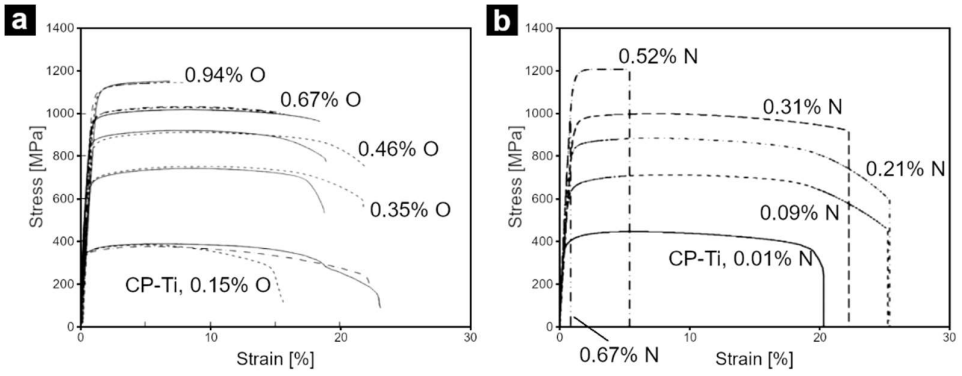

Figure 2.11: Stress strain curves of L-PBF CP-Ti with added a) oxygen and b) nitrogen.

2.3.3 The Titanium-Carbon system

In titanium, interstitial carbon is much less studied than the other interstitials for several reasons. It has negligible solubility in the α-phase at room temperature, so a super-saturated solid solution must be created in order to study it (Fig. 2.12)[173]. It also does not occur in high quantities in the air yet, making atmospheric absorption during high temperature processing a non-issue.

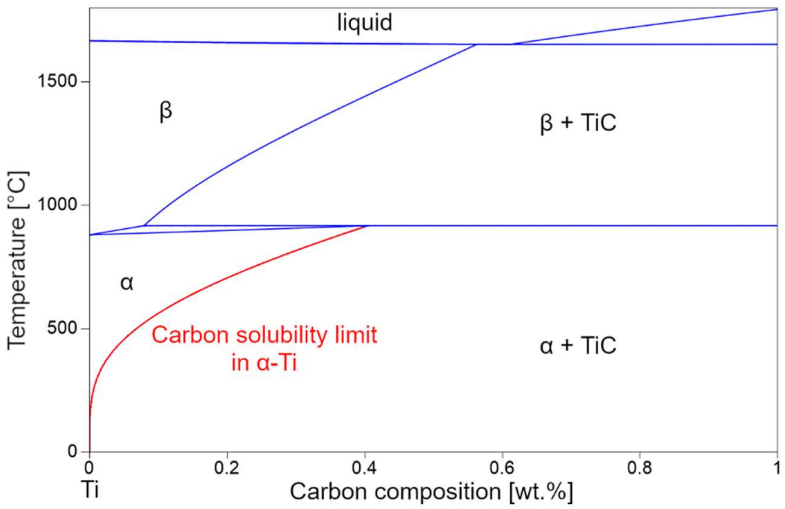

Figure 2.12: The Ti-C binary phase diagram.

While interstitial carbon is not well studied, precipitated carbon is a popular topic. TiC is an effective precipitate for high strength composites due to its high hardness and good interfacial bonding with titanium[174]. Carbon can be introduced to the titanium alloy natively as graphite or graphene oxide, or already in the form of TiC[175–178]. It can also be introduced alongside other elements such as B_4C and Mo_2C, in which the additive compound will decompose during formation and precipitate back out as TiC[178–182]. Carbon can be added to titanium atmospherically by printing under a methane atmosphere[183]. Precipitation strengthening creates excellent composites for ultra-high strength applications[184]. This is particularly useful in β-phase alloys, which tend to have lower strength[185]. However, due to extreme brittleness, these composites are more popular for their tribological properties as wear-resistant materials rather than as load-bearing parts[186–188].

While carbon is well understood for precipitation strengthening, it also has great potential for solid solution strengthening. It has been repeatedly suggested that the dissolved carbon is the dominant strengthening mechanism for Ti-TiC rather than the TiC precipitates[109,189]. Not only are the TiC particles suggested to provide only marginal improvement to strength, but they also severely reduce ductility by promoting void nucleation[190]. First principles calculations have also suggested that carbon can improve ductility by promoting partial dislocation emission from perfect dislocations to a greater degree than oxygen or nitrogen[191]. This dissertation will use in-situ L-PBF alloying to explore the effect of interstitial carbon on the mechanical properties of titanium and its alloys.

Chapter 3:
Methods

3.1 Experimental Overview

The experiments done in this study show the effect of dissolved carbon on the mechanical performance of titanium and its alloys. Materials were produced by L-PBF in order to reliably induce a super-saturated solid solution of carbon. Commercially pure titanium (CP-Ti) and the two alloys Ti64 and Ti-10Mo were investigated as matrix materials in order to robustly show the effect of carbon across a range of alloys. The experimental layout shown in Fig. 3.1 arranges these three matrix materials in order of increasing β-phase stability, rarity, and cost. CP-Ti and Ti64 are well established materials for L-PBF, so the parameters and properties without carbon addition required no in-depth investigation. Ti-10Mo is a more modern alloy, so a detailed optimization and characterization of the alloy without carbon addition was performed to provide a reliable baseline.

In order to create a carbon solid solution, TiC was added in small, incremental quantities to all three matrix materials. By performing the characterization techniques detailed in this chapter, the effect of dissolved carbon on mechanical performance was clarified in terms of both its quantitative impact on mechanical properties as well as the mechanisms behind these mechanical improvements.

3.2 Powder Preparation

Feedstock powder was obtained from Osaka Titanium Technologies Co., Ltd and Kojundo High-Purity Chemicals. Osaka Titanium Technologies Co. provided titanium powder

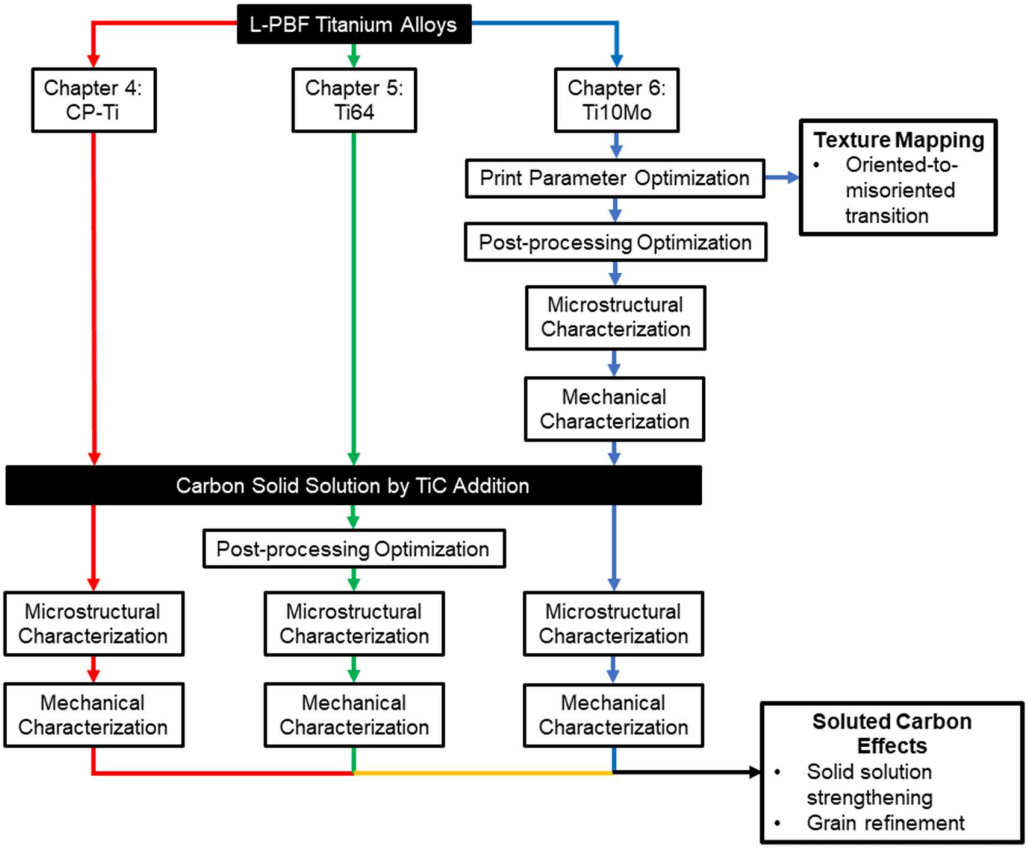

Figure 3.1: Flowchart of experiment design.

from their Titanium Low Oxygen Powder (TILOP) series. TILOP-45 is a CP-Ti powder compliant with ASTM Grade 2, and TILOP64-45 is a Ti64 powder compliant with ASTM Grade 23, as listed in ASTM standards B265 and B348[34]. Both powders are produced as gas-atomized spheres (Fig. 3.2 a-b) and have a listed maximum diameter of 45 µm. TILOP-45 has an average size of 24 µm, and TILOP64-45 has an average diameter of 25 µm. Kojundo High-Purity Chemicals provided both titanium carbide powder (TII02PB) and molybdenum powder (MOE03PB). The titanium carbide had an approximate size range of 2-5 µm, and the molybdenum powder had an average size of 3 µm.

Powders mixtures were prepared in batches of 500-1000g of total powder. Appropriate weights of the component powders were added to a polypropylene bottle along with approximately 10 wt.% of 5 mm ZrO_2 balls. The powder and balls were loaded into a rocking mill (SEIWA GIKEN, RM-5) and shaken at 60 Hz for 1 hour. The ZrO_2 balls were removed with a steel strainer, and the powder was stored in the polypropylene bottle under vacuum.

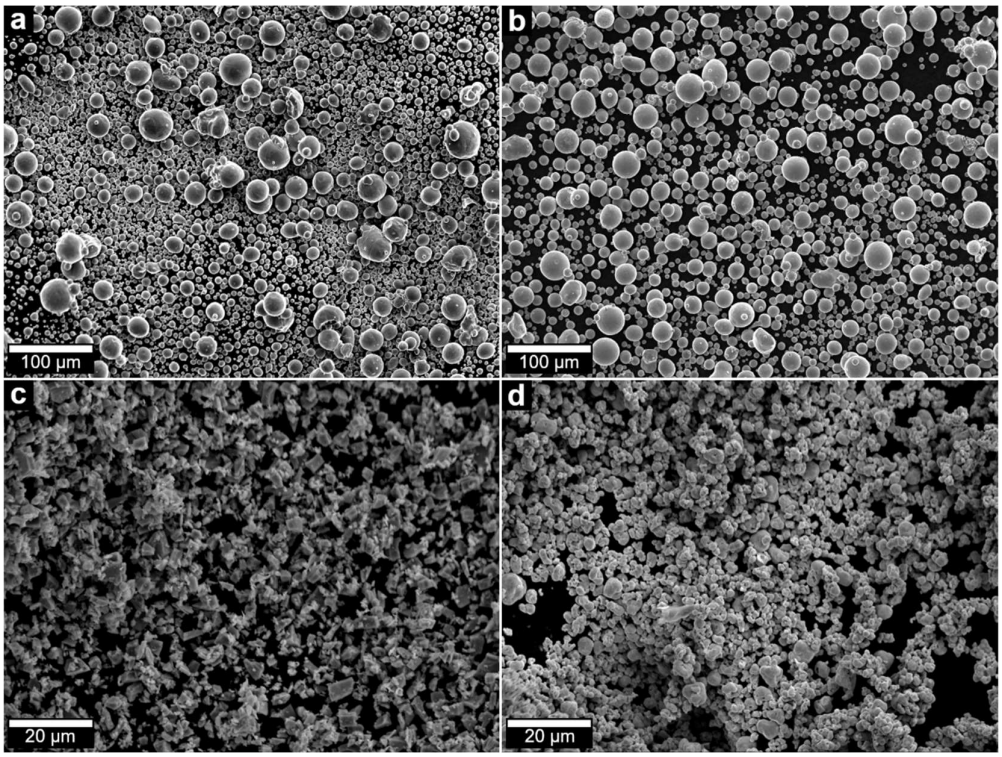

Figure 3.2: As-received powder morphology of a) TILOP-45, b)TILOP64-45, c) TiC, d) Mo.

3.3 Manufacturing and Consolidation

3.3.1 Additive Manufacturing

Laser powder bed fusion was performed by the TruPrint 1000 3D printer by TRUMPF (Fig. 3.3). The TruPrint 1000 is a self-contained L-PBF printer for small-scale metallic additive manufacturing. The printer uses a YAG continuous fiber laser rated for up to 200 W with a wavelength of 1070 ± 10 nm. Printing is supported under high purity argon or nitrogen atmospheres, but only argon was used. The build space is cylindrical, with a 100 mm diameter and a maximum build height of approximately 170 mm.

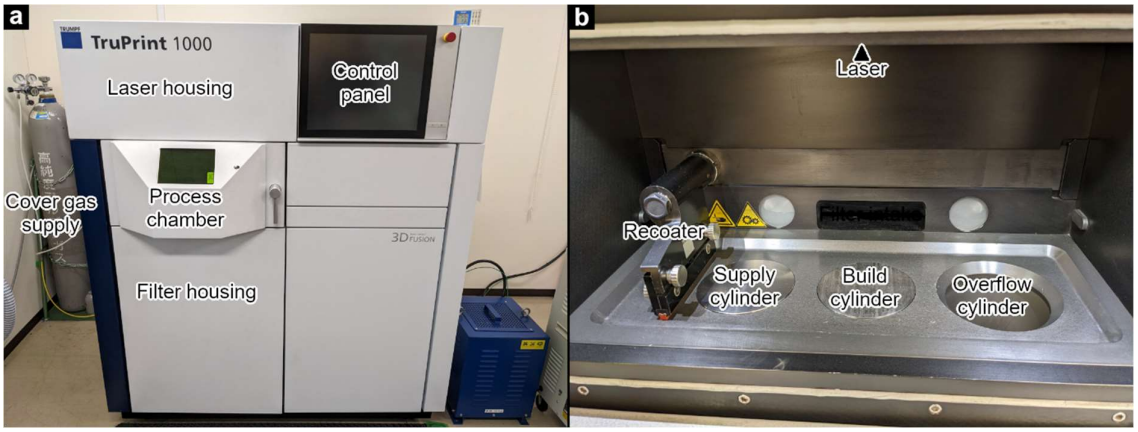

Figure 3.3: The TRUMPF TruPrint 1000 printer a) exterior, b) build chamber.

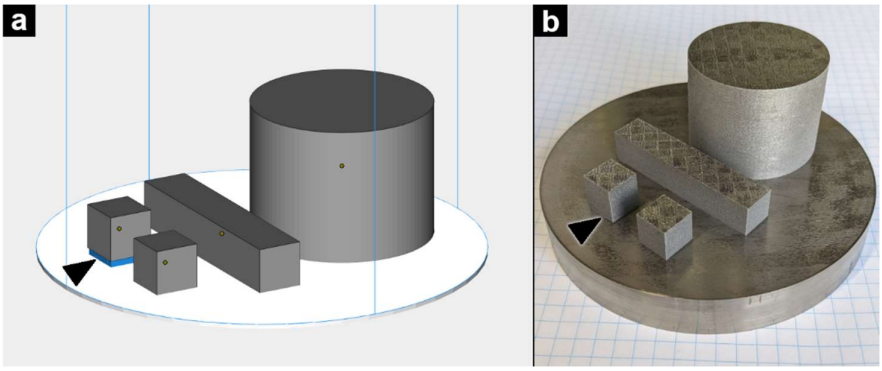

Figure 3.4: Characteristic printed part shapes. Support structures are marked with a black triangle. a) CAD interface, b) as-printed samples.

Print geometry was designed using the Materialize Magics 23.01 software. This software enabled computer aided design (CAD) of basic geometric shapes as well as the importing of pre-made .stl files. The parts could be generated, dimensioned, and manipulated freely across the build space. Support structures could be generated between parts and the substrate, or the parts could be printed directly onto the substrate (Fig. 3.4a).

While the program allows for a near limitless number of print configurations, a few standard geometries were used (Fig. 3.4). The geometry for manufacturing tensile test samples was a 50×10×10 mm rectangular prism. The geometry for microstructure observation and characterization was a 10×10×10 mm cube. Cylinders with a diameter of 40 mm and a height of 30 mm were printed for additional post-processing analysis. Both supported and unsupported geometries were used. When supports were used, a mesh type support structure was generated with thickness of a 1.5 mm.

Print parameters were also set via the Materialize Magics software. Parameters could be applied individually to each part in the build volume or in bulk to the whole build. Some parameters, such as layer thickness or cover gas velocity, could only be applied to the whole build. Layer thickness was held at a constant 20 µm over the course of the project. Cover gas speed was 2.5-3 mm/s. The build surface was located near the focal point of the laser, where the beam diameter is approximately equal to the wavelength of 1070 nm.

Laser power, laser scan speed, and hatch width were adjusted as appropriate per experiment. Laser powers of 140 to 180 W, scan speeds of 450 to 2500 mm/s, and hatch widths of 21 to 320 µm were used over the course of this project. The primary print condition for CP-Ti alloys and Ti64 alloys was a power of 160 W, a scan speed of 535 mm/s, and a hatch width of 110 µm, leading to a VED of 136 J/mm^3. The primary print condition for Ti-10 Mo alloys was a power of 160 W, a scan speed of 500 mm/s, and a hatch width of 123 µm, leading to a VED of 130 J/mm^3. The parameters are listed in Table 3.1.

The scan strategy was an alternating offset chessboard with outline. Each layer would begin with a low LED scan of the outline of each part's cross section to improve surface quality

Table 3.1: Primary L-PBF parameters for each matrix material.

Matrix material	Chapter	Laser power [W]	Scan mpeed [mm/s]	Hatch [µm]	Layer thickness [µm]	VED [J/mm^3]
CP-Ti	4	160	535	110	20	136
Ti64	5	160	535	110	20	136
Ti-10Mo	6	160	500	123	20	130

and keep the powder in place. Then the bulk would be filled in with a chessboard pattern (Fig. 3.5). To fill in each 3.96 mm chessboard panel, the laser would raster through parallel hatches in a zig-zag pattern. The hatches of adjacent chessboard panels are rotated 90°. When filling in an area, every other chessboard panel in a straight line would be filled in sequence across the length of the sample, then the in-between panels would be filled in sequence before moving to the next line. The chessboard pattern of each subsequent layer was offset by 2.73 mm in one chessboard direction and 3.22 mm in the other to prevent accumulation of chessboard panel edge defects. This pattern was part of the parameters recommended by TRUMPF for the processing of titanium alloys and had been optimized for low residual stresses and good surface quality.

Once the part geometry and print conditions were set, the print details were exported to a machine-specific .WZA file. This file was then transferred from the CAD computer to the printer interface.

For the physical preparation of each print, a bottle of pre-mixed powder was poured into the supply cylinder, then carefully leveled with a straightedge such that the as-poured packing density was preserved. A substrate was then mounted in the build cylinder via the substrate mounting jig. The cylindrical substrates were made of CP-Ti or Ti64 and had

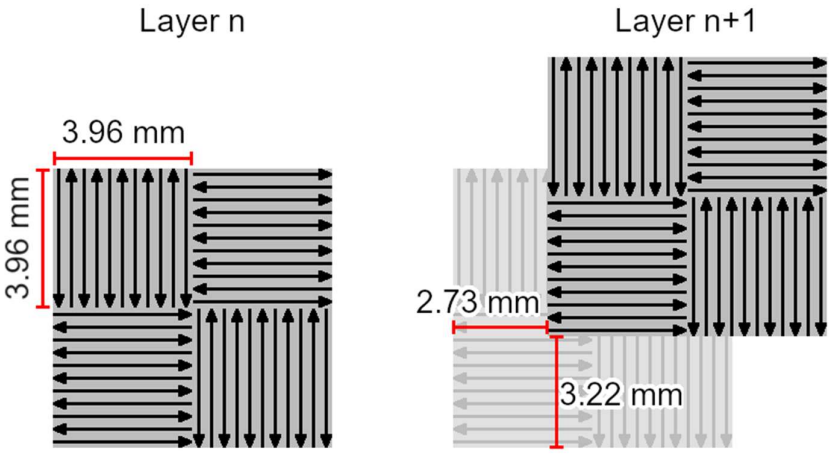

Figure 3.5: Chessboard scan strategy.

diameters of 99 mm and thickness ranging from 10 mm to 40 mm. The substrates were manually brought to level with the process chamber floor for their initial state. Finally, the rubber recoater was bolted to the recoating mount. The process chamber was ensured to be clean and clear before being sealed and flooded with high-purity (>99.999%) argon gas. Printing began once the oxygen content was below 200 ppm, and argon was supplied as necessary to keep the steady-state oxygen content below 100 ppm.

Once the print had finished and cooled off, the substrate was removed from the mounting jig. Samples fixed to the substrate by support structures were removed via careful application of a hack saw and a hammer. Samples printed directly onto the substrate without supports were removed via wire electric discharge machining (EDM) using a Sodick AG-130L.

3.3.2 Post-processing

While the as-printed behavior of the various alloys was observed, most samples also went through some form of post-processing to further improve their mechanical performance. In most cases, this took the form of heat treatment, although hot extrusion was also used.

Heat treatment was performed in a vacuum furnace (FULL-TECH, FTV-1200R-250). A medium vacuum of under 200 Pa was achieved before heat treatment began and was maintained throughout the treatment to prevent oxidation. The sample was heated to the holding temperature at a rate of 20°C/min. The internal furnace temperature was verified by thermocouple. The standard holding temperature and time was 700°C for 3 hours, but many other heat treatments were investigated. After the holding time, one of three different cooling methods was applied. With furnace cooling, the sample was held in the vacuum until the internal furnace temperature was less than 100°C. With air quenching and water quenching, the sample was quickly removed from the furnace chamber and immersed in the relevant room temperature fluid until it also reached room temperature.

Hot extrusion was performed using the cylindrical billet (Fig. 3.6). The 30×ϕ40 mm billet was pre-heated for 10 minutes at 1100°C. It was then mounted into a pre-heated steel chamber on a 2000 kN hydraulic press (Shibayama Kikai, SHP-200-450). The billet was then extruded through a round die with an outer diameter of 42 mm and an inner diameter of 15 mm, giving an extrusion ratio of 7:1.

3.2.3 Spark-Plasma Sintering

Additional sample consolidation was performed via spark-plasma sintering (SPS). For each sample, approximately 75 g of pre-mixed powder was loaded into a cylindrical graphite die with a 30 mm diameter. This die was then loaded into an SPS machine (NJS SPS Center, SPS-1030S), where a medium vacuum of less than 5 Pa was held. The sample was raised to a temperature of 1000°C under a pressure of 15 MPa at a heating rate of 20°C/s. The sample was

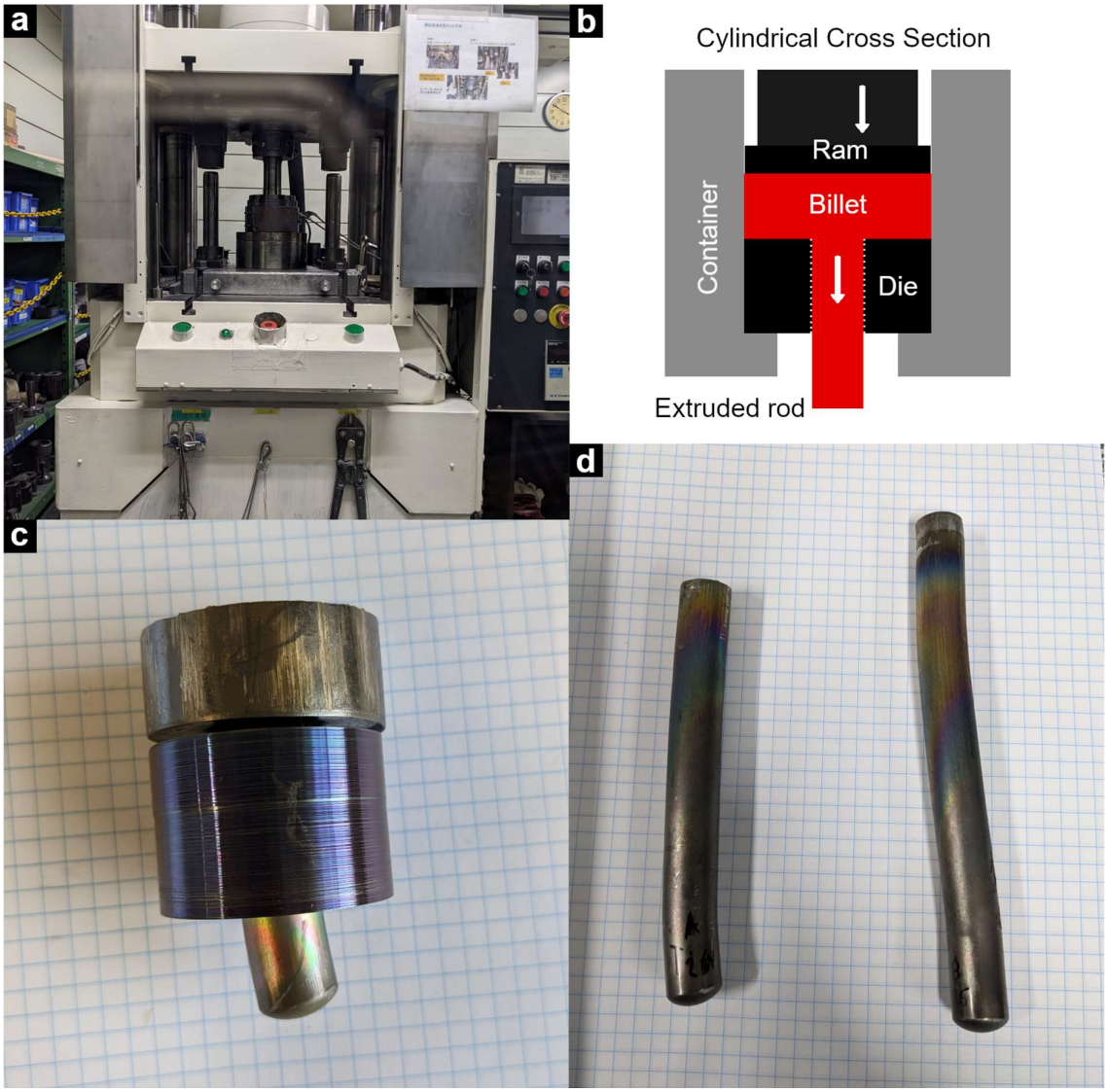

Figure 3.6: Hot extrusion. a) the hydraulic press, b) a schematic of hot extrusion, c) a partially extruded billet with die, d) fully extruded rods.

Figure 3.7: A section of a sample produced by spark-plasma sintering.

then held at 1000°C for 30 min at a pressure of 30 MPa to fully consolidate it. After furnace cooling, the sample was mechanically pushed out of the die (Fig. 3.7).

3.4 Characterization

3.4.1 Sample Preparation

Each material was extensively characterized with respect to composition and microstructure. Cross sections were cut using a rotary fine cutter with SiC disks (HEIWA TECHNICA, SS-31). The samples were then mounted in a conductive carbon-epoxy puck using the BUEHLER SIMPLIMET 1000. These pucks were then ground clean using SiC grinding paper on a rotational polishing table (IMT, IM-P2). Grinding paper grits of 80 to 4000 were used, and each sample was rotated 90° every time a finer grit was used. After grinding, the sample was polished for 5-10 min using a 0.1 μm Al_2O_3 suspension on a cloth polishing pad on the rotational polishing table.

The final polish could be achieved by vibratory or electrochemical polish, depending on the material composition. For vibratory polishing, 0.06 μm colloidal silica (BUELHER, MasterMet) was used as the polishing medium in the BUEHLER Vibromet 2 vibratory polisher. Polishing times of 4-16 hours were used as appropriate for each sample. For electrochemical polishing, a solution of 95% acetic acid and 5% perchloric acid was used[192,193]. The sample was connected to the anode of a power supply and immersed in the polishing solution with the desired face turned towards the cathode. A low current was run through the solution for 2-5 minutes, until the desired face had a mirror finish. The polishing solution was continuously mixed with a stir magnet.

3.4.2 General Characterization

The composition of interstitial elements was determined for each material. The concentration of oxygen, nitrogen, and hydrogen was determined using a HORIBA EMGA 830 analyzer. The concentration of carbon was determined using a HORIBA EMIA-221 analyzer. For each analysis, three samples of 0.4-1.0 g were manually cut from the material using the fine cutter and bolt cutters. Each sample was then loaded into a crucible and covered in a low-reactivity metal. The non-weighted average composition was then used.

Density was determined using the Archimedes principle. The dry weight of the sample in air was measured. Next, the sample was immersed in water and agitated to remove residual bubbles. The submerged sample was then weighed while underwater. By comparing the dry weight (m_{dry}), the submerged weight (m_{wet}), and the density of water (ρ_{water}), the density (ρ) could be calculated by equation 3.1:

$$\rho = \frac{m_{\text{dry}}\ \rho_{water}}{m_{\text{dry}} - m_{\text{wet}}} \tag{3.1}$$

Crystallographic data was obtained using a SHIMADZU XRD-6100 X-ray diffractometer (XRD). X-rays were generated using a copper source and filtered to the K_α wavelength of 1.54 Å. Diffracted X-rays were detected through a 0.3 mm receiving slit for 0.60 seconds per data point. Each material was scanned from 2θ angles of 30° to 80°. For CP-Ti and Ti64 alloys, the scan speed was 1°/min and the sampling pitch was 0.01°. For Ti-10Mo alloys, the scan speed was 2°/min and the sampling pitch was 0.02°. High-resolution scans were also performed from 34° to 40° using a scan speed of 0.2°/min and a sampling pitch of 0.002°. The data was lightly processed by the program to remove background noise and exported to a .txt file.

XRD data was analyzed using a custom MATLAB program using the R2021a edition of the MATLAB software. Peaks were identified by applying a linear average smoothing filter over the raw data. The filter smoothed over an increasing number of points until the number of local maxima was stable. Local maxima and minima of the smoothed data were identified. Local maxima below a threshold background value were not considered in this analysis. Gaussian peaks were then fit to each smoothed local maximum using the raw data spanning between the two adjacent local minima. The center of this gaussian was taken as the 2θ location of the peak, and the maximum value of all raw data in this span was taken as the peak intensity. An estimated peak pattern was generated from approximate lattice parameters by using Bragg's law:

$$n\lambda = 2d \sin\theta \tag{3.2}$$

Where n is an arbitrary positive integer, λ is the X-ray wavelength, d is the spacing between atomic planes, and θ is the detector angle. In this study, n was taken as unity. Real peaks were then assigned to the relevant phase and crystallographic plane families by proximity to the estimated peak location. To determine the real lattice parameters, a minimization function was run over all possible lattice parameters such that the root mean squared of the difference between the estimated peak locations and true peak locations was minimized.

3.4.3 Microscopy

Optical microscopy (OM) was performed using a SHIMADZU SPM-9600 scanning probe microscope. The accelerating voltage was 15 kV, yielding a current of approximately 90 μA. Photographs were taken using the dynamic focus function.

Scanning electron microscopy (SEM) was performed using the JEOL JSM-7100F and the JEOL JSM-6500F field emission scanning electron microscopes. Four different imaging modes were used: secondary electron imaging, backscattered electron (BSE) imaging, energy dispersive X-ray spectrometry (EDS), and electron backscatter diffraction (EBSD). Secondary electron imaging gives primarily topography-based contrast, so it was used for powder morphology observation. BSE imaging has a strong compositional contrast as well as weak

crystallographic contrast, so it was used for some microstructural observation. The compo imaging technique was used alongside the BSE imaging.

For EDS, the JEOL JED-2300 detection system was added to the SEM. The EDS was performed at a working distance of 10 mm. EDS peaks were automatically indexed by the software to the elements nominally included in each alloy. EDS compositional imaging was performed to show elemental compositional contrast across an image. Point, line, and area scan techniques were used to quantify elemental composition.

EBSD used a TSL and EDAX SC-200 detector and imaging software. The working distance was 20 mm. Kikuchi patterns were identified and indexed for each point in a selected area. This data was then processed using the EDZX OIM Analysis 8 software.

Transmission electron microscopy (TEM) was performed using a JEOL JEM-2100F Transmission Electron Microscope. TEM foils were prepared by focused ion beam (FIB), using a JEOL JIB-4500.

3.4.4 Mechanical Testing

Uniaxial tensile testing was the primary method of mechanical performance evaluation. Tensile testing was performed using dogbone-type samples with a rectangular cross section (Fig. 3.8). These samples had a thickness of 1 mm, a gauge width of 2 mm, and a gauge length of 10 mm. There were 1 mm radius shoulders at the ends of the gauge length, and 2 mm shoulders located 7 mm away from the gauge where the sample was mounted into the tensile tester. The dogbones were manufactured by Miyakojima Seisakusyo Co., Ltd via with a lightly polished finish. For L-PBF material, three dogbones were cut for each material from near the center of 10×10×50 mm rectangular bar in a horizontal orientation. The 1 mm thickness was parallel to the build direction, and the shoulders were curved in the build plane. The top and bottom 1 mm of the rectangular bar were not used to avoid sampling boundary conditions.

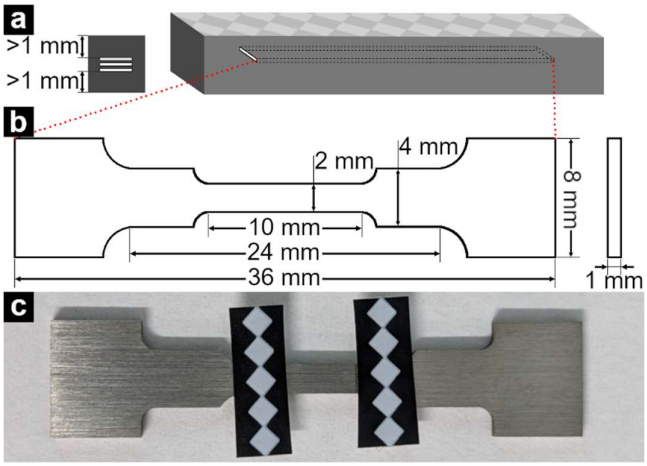

Figure 3.8: A tensile test dogbone. a) dogbone source location, b) dimensions of the dogbone, c) dogbone with DIC stickers and machined surface finish.

The uniaxial tensile tests took place on a Shimadzu Autograph AG-X 50 kN. Force was measured by a 50 kN load cell. Displacement was measured using the built-in digital image correlation (DIC) software. Black and white DIC identification stickers were attached to the tensile sample at either end of the gauge length, approximately 8 mm apart (Fig. 3.8c). The dogbone with stickers was filmed during the tensile test so that displacement could be evaluated by DIC. All three dogbones were tested to ensure data fidelity. The average width and thickness of the rectangular gauge cross section was measured by micrometer before every test. The stroke rate was 5 μm/s, and the sampling rate was every 0.1 seconds. There was no pre-loading.

Tensile data was evaluated by a custom MATLAB program. Engineering stress was calculated by dividing the load by the gauge cross section area as measured by micrometer. Engineering strain was calculated by dividing the DIC displacement by the original DIC length. Effective elastic modulus was evaluated by finding the average stress to strain ratio over 1000 consecutive data points. The 1000 consecutive points with the highest average stress to strain ratio was taken to be the linear elastic region (Fig. 3.9). This average stress to strain ratio of the linear elastic region was used as the effective elastic modulus. To remove the effects of pre-loading, the linear elastic region was extrapolated to zero stress, and strain was offset such that the extrapolation intercepted the origin. Fracture was determined to occur when the change in stress between two adjacent data points was at a minimum (greatest negative change). The strain value immediately preceding this change was taken to be the elongation to failure. Data after this change were not considered.

The stress values were then smoothed by a 5-point linear average filter to remove noise. Ultimate tensile stress (UTS) was determined by the maximum of the smoothed stress values. Yield stress was determined using the 0.2% offset method (Fig. 3.9). A line with a slope equal to the effective elastic modulus and a strain-intercept of 0.002 was defined. The intercept of

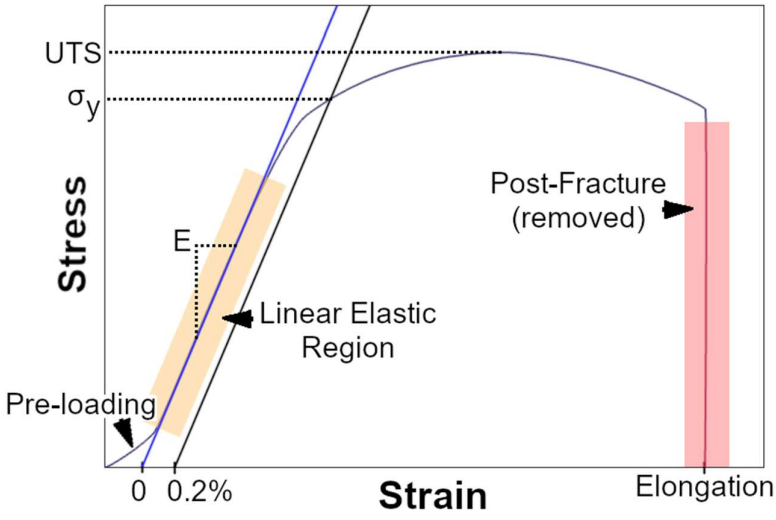

Figure 3.9: Representative stress strain curve showing various processing regions and characteristic values.

this line with the stress-strain curve was taken to be the yield stress. Yield stress, UTS, elongation to failure, and effective elastic modulus for a material was defined as the average over all three samples. For plotting purposes, representative stress-strain curves are taken from the samples with the elongation to failure closest to the material average.

Chapter 4:
L-PBF Soluted Carbon in Pure Titanium

4.1 Experimental Overview

To understand the effect of carbon on titanium's alloys, the binary carbon-titanium system must first be understood. This chapter contains preliminary collaborative research done by the Department of Composite Materials Processing. The data provide proof-of-concept for L-PBF titanium alloys containing a carbon solid solution by demonstrating feasibility of production and viability of heat treatment parameters. The resulting materials give experimental evidence of dramatically enhanced mechanical properties via carbon addition. Furthermore, this chapter provides the template for experimental design and analysis that is used for subsequent alloys.

All ASTM grades of commercially pure titanium (Grades 1-4) are allowed to contain up to 0.08% carbon, but the powder used in this study had no measurable carbon content (<0.02%). To increase the carbon content, supplemental carbon was added in the form of titanium carbide. TiC powder was added to the CP-Ti powder at quantities of 0.25 wt.%, 0.5 wt.%, and 1 wt.%. The mixed powder as well as unalloyed CP-Ti was then printed into rectangular 50×10×10 mm bars using the 136 J/mm^3 print condition listed in Table 3.1. Two bars were printed at each composition. One bar was printed with supports and heat treated for 1 hour at 500°C[†], and the other was printed without supports and heat treated for 3 hours at 700°C.

[†]Experiments and data collection for the 1 hour at 500°C samples were performed by Eri Ichikawa.

4.2 Characterization

4.2.1 Interstitial Composition

Interstitial compositional analysis was performed after heat treatment. The results are listed in Table 4.1. Nominally, 1% TiC is equal to 0.2% C, but the exact carbon content was measured to account for experimental error. The measured carbon content in each sample is similar to the expected nominal amount, indicating excellent stability of carbon addition via TiC. There is no evidence of evaporation of carbon during the L-PBF process. Notably, the nitrogen content of the 0.5 and 1% TiC samples heat treated for 3 h at 700°C is significantly higher than the other samples. This is due to the nitrogen accumulation problem discussed in Appendix A.

Table 4.1: Interstitial composition of CP-Ti with TiC.

Nominal TiC [wt.%]	Heat treatment	Hydrogen [wt.%]	Nitrogen [wt.%]	Oxygen [wt.%]	Carbon [wt.%]
0	1 h at 500°C	0.004	0.008	0.155	0.021
0.25	1 h at 500°C	0.006	0.011	0.164	0.091
0.5	1 h at 500°C	0.006	0.017	0.162	0.156
1	1 h at 500°C	0.003	0.027	0.175	0.248
0	3 h at 700°C	0.006	0.026	0.195	0.001
0.25	3 h at 700°C	0.004	0.016	0.158	0.067
0.5	3 h at 700°C	0.004	0.060	0.179	0.114
1	3 h at 700°C	0.004	0.049	0.181	0.226

Equilibrium TiC stability can be observed by the calculated phase diagram (Fig. 4.1). At equilibrium, carbon has negligible solubility at room temperature, but its solubility in the α-phase increases rapidly with increasing temperature. At 500°C, TiC concentrations of 0.5% and 1% are not fully soluble, but lower concentrations are soluble. At 700°C, 0.5% TiC is fully soluble, and 1% TiC is nearly fully soluble.

4.2.2 Microstructure

All samples heat treated for 1 h at 500°C showed exclusively α-phase XRD peaks and no TiC peaks, indicating full dissolution of TiC (Fig. 4.2). A fully α-phase titanium matrix is as-expected because carbon is an α-stabilizer[154]. The α lattice parameters were calculated using Bragg's law (Eq. 3.2). The *a* lattice parameter showed no significant trend with increasing

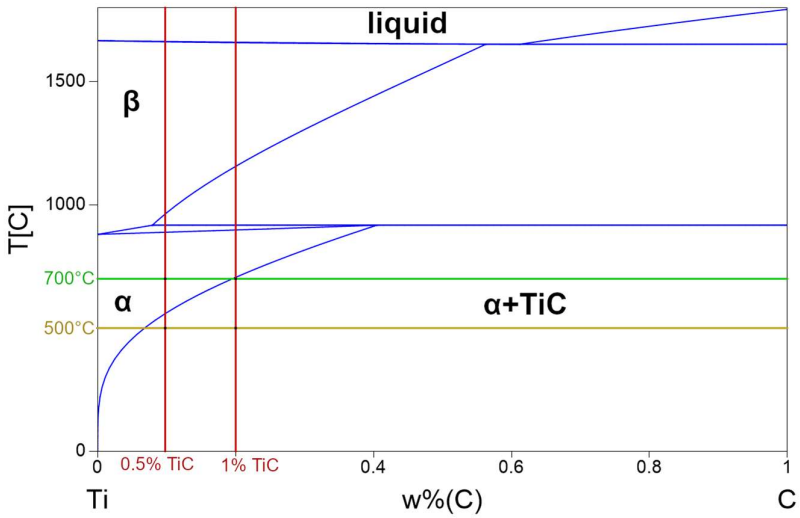

Figure 4.1: Calculated binary phase diagram of titanium and carbon.

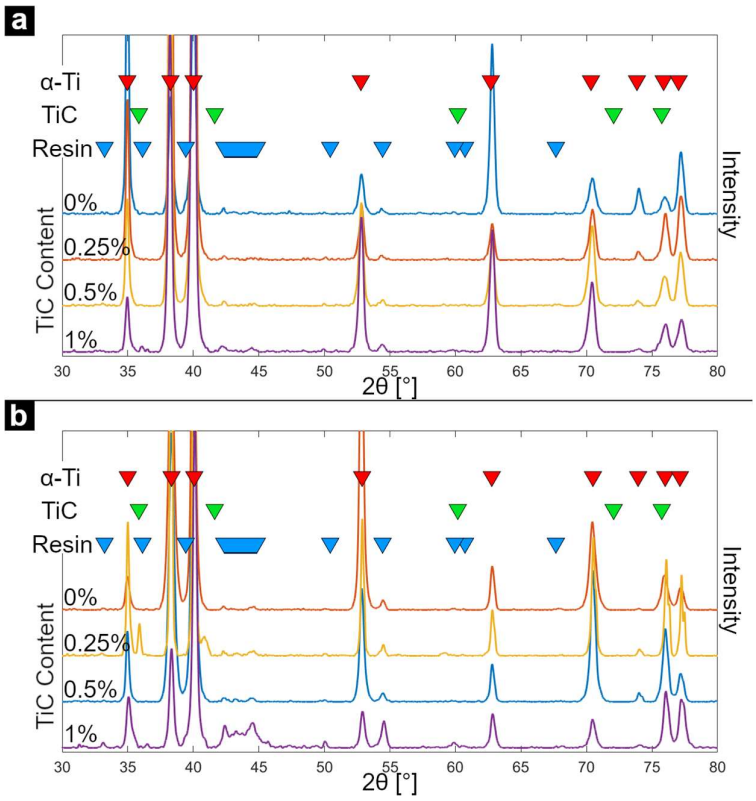

Figure 4.2: X-ray diffraction of CP-Ti with TiC mounted in resin after heat treatments of a) 1 h at 500°C, b) 3 h at 700°C.

carbon content (Fig. 4.3a). The *c* lattice parameter was shown to expand with increasing carbon content. Expansion of the *c*-axis with increasing carbon content is a well-established phenomenon. Carbon is reported to increase the c/a ratio from 1.588 to 1.589 with the addition of 0.16% C[157]. First principles calculations of dissolved carbon in Ti show this is because carbon can exist as a metastable solid solution in octahedral voids in the α matrix[191]. L-PBF of the Ti-C system involves hyper-rapid solidification, leading to complete solute trapping. These results confirm that a super-saturated carbon solid solution is formed in titanium by this L-PBF processing method, and no notable TiC precipitation has occurred.

Unusually, TiC peaks were observed in the 0.25% TiC sample heat treated for 3 h at 700°C (Fig. 4.2b). This is unexpected because the calculated phase diagram showed that TiC is highly soluble in titanium at 700°C and no TiC peaks are observed in any other sample. The peaks are considered to be from a sampling outlier of a TiC agglomeration and not representative of the bulk composition of this sample. This sample is a useful reference for comparison with the other samples because it demonstrates the sensitivity of XRD analysis to the presence of TiC and confirms that TiC is not present in any other sample.

Heat treatment for 3 h at 700°C led to a similar lattice parameter behavior (Fig. 4.3b). The *a* lattice parameter showed no correlation while the *c* lattice parameter showed a constant increase with increasing TiC content. The *c* lattice parameter in the samples heat treated for 3 h at 700°C are consistently lower than those of the equivalent samples treated for 1 h at 500°C. Th reduction in *c* is due to incomplete relaxation of α′ martensite, which has a larger *c* lattice parameter, in the samples heat treated for 1 h at 500°C.

EBSD micrographs of samples heat treated for 1 h at 500°C show that carbon has a strong grain-refinement effect on CP-Ti (Fig. 4.4). As will be shown in the next chapter, the 1 h at 500°C heat treatment is merely for relief of residual stresses and has a negligible effect on microstructure. Therefore, the micrographs shown in Fig. 4.4 are considered representative of the as-printed microstructure. CP-Ti printed by L-PBF shows a microstructure of large, columnar α grains. With the addition of 0.25% TiC, the microstructure switches from a

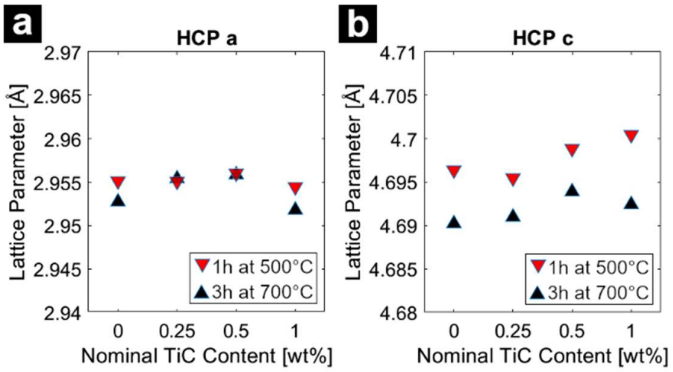

Figure 4.3: Lattice constants of CP-Ti with TiC after heat treatments of a) 1 h at 500°C, b) 3 h at 700°C.

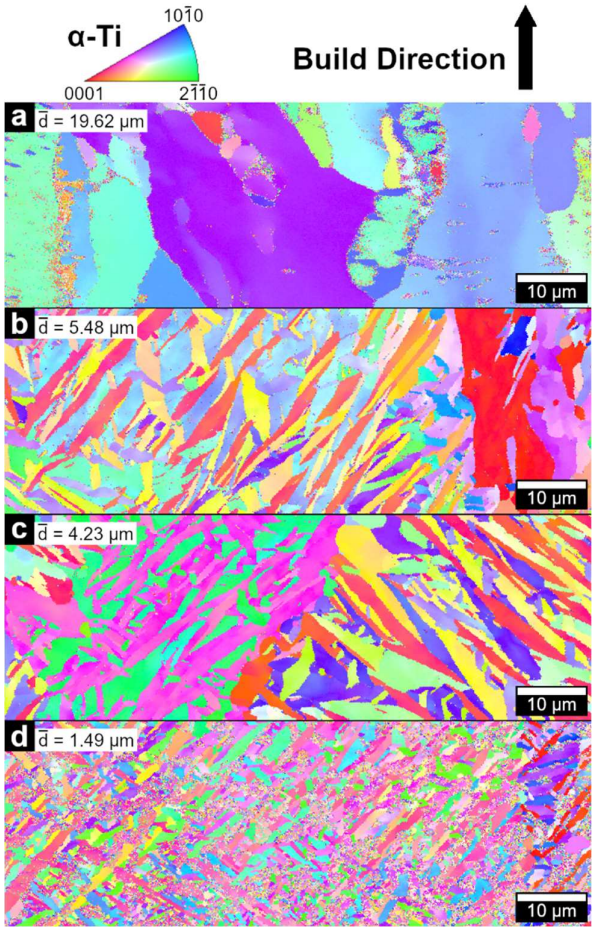

Figure 4.4: EBSD of CP-Ti with TiC after 1 h at 500°C. a) 0% TiC, b) 0.25% TiC, c) 0.5% TiC, d) 1% TiC.

columnar-type structure to a martensitic-type structure. Carbon promotes the transformation from β to α′ martensite by destabilizing the β phase and raising the martensite start temperature[54]. The grain refinement with increasing carbon is also a product of increasing α′ stability. There is greater nucleation of martensitic laths, so the higher density of laths leads to smaller grain size[100].

Heat treating the samples for 3 h at 700°C led to microstructures that were incompatible with the available sample preparation techniques. Indexing these samples with EBSD showed large areas of interference, likely from a corrosion product or local deformation, shown as black in Fig. 4.5. Despite the poor image quality, the overall microstructure and grain size can still be observed. No TiC was observed in any sample, indicating the solid solution is stable throughout this heat treatment condition.

The samples heat treated for 3 h at 700°C show globularization of α grains and significant grain growth, which is the typical behavior for martensitic titanium undergoing these heat treatment conditions[134]. For the 0, 0.25, and 0.5% TiC samples, the grain size after

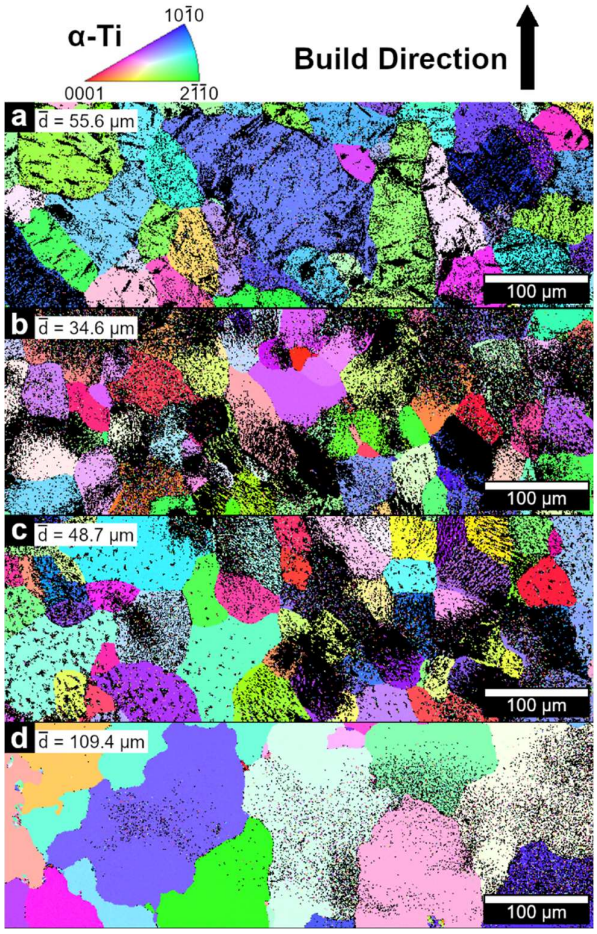

Figure 4.5: EBSD of CP-Ti with TiC after 3 h at 700°C. a) 0% TiC, b) 0.25% TiC, c) 0.5% TiC, d) 1% TiC. Black areas could not be indexed.

3 h at 700°C was consistently about 40 µm greater than the grain size after 1 h at 500°C, indicating a constant grain growth rate.

The grains of the 1% TiC sample are 108 µm larger in the sample heat treated for 3 h at 700°C than in the sample heat treated for 1 h at 500°C, significantly more than the other samples (Fig 4.6). The constant grain growth rate across the other samples suggests that the increased grain size is not due to a faster grain growth rate. In fact, the solute drag phenomenon posits that the grain growth rate should be slightly slower with increased carbon content[144]. The grain borders are also much more irregular than the other compositions, which is inconsistent with rapid grain growth. Therefore, it can be concluded that these massive grains are fusions of smaller, martensitic grains with similar orientations. The 1% TiC sample heat treated for 1 h at 500°C showed a martensitic microstructure with only a select few grain orientations. During grain growth at 700°C, these similarly oriented grains can fuse if they share a grain boundary[194]. Therefore, the unusually large grain size is due to carbon promoting the fusion of similarly oriented grains during grain growth.

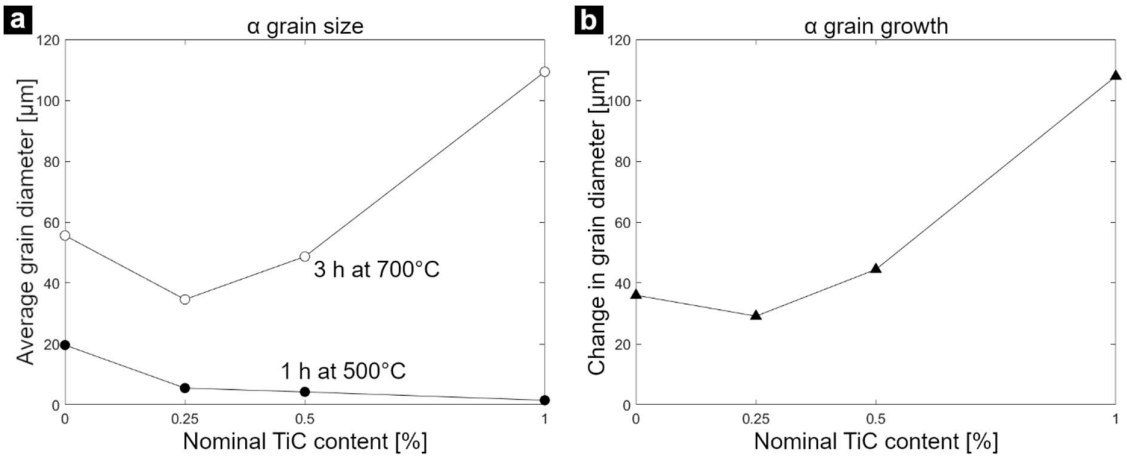

Figure 4.6: Grain size properties of CP-Ti + *x*% TiC. a) Average grain diameter at each heat treatment and composition, b) the difference in average grain diameter between the two heat treatments.

4.3 Mechanical Properties

Uniaxial tensile testing of the samples heat treated for 1 h at 500°C showed a remarkable increase in yield strength (Fig. 4.7). Mechanical properties are listed in Table 4.2. Yield strength and ultimate tensile strength (UTS) increased continuously from 328 MPa and 392 MPa respectively in CP-Ti to 660 MPa and 746 MPa with the addition of 1% TiC. The ductility had the unusual trend of increasing from 26.3% to 29.0% elongation to failure when 0.5% TiC was added to CP-Ti. Further addition of TiC reduced ductility.

The yield stress was decomposed into the incremental contributions of various factors through the linear combination of several models (Fig. 4.7b). The effect of grain size was modeled using the Hall-Petch equation (Eq. 2.1), using EBSD to measure average grain

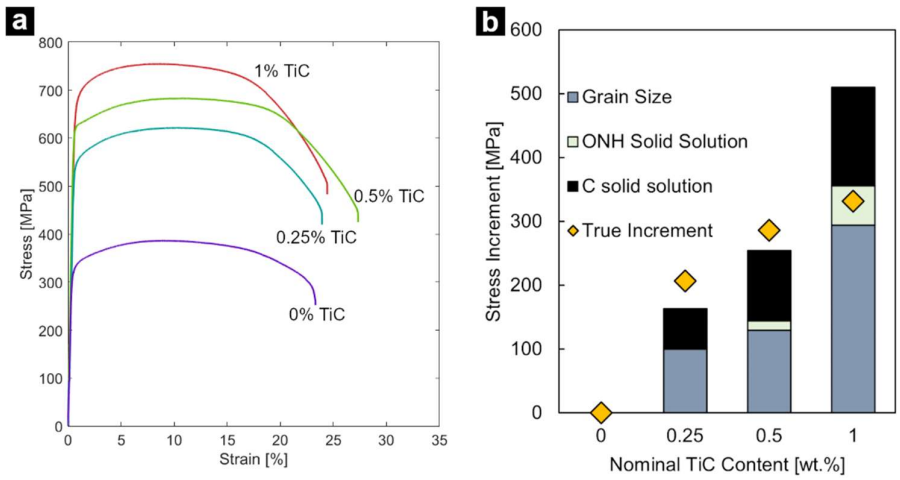

Figure 4.7: Mechanical properties of CP-Ti + *x*% TiC heat treated for 1 h at 500°C: a) tensile test stress-strain curves, b) yield stress decomposition.

Table 4.2: Mechanical properties of CP-Ti + *x*% TiC heat treated for 1 h at 500°C.

TiC addition [wt.%]	Yield stress [MPa]	UTS [MPa]	Ductility [%]
0	328	392	26.3
0.25	535	616	25.2
0.5	614	679	29.0
1	660	746	27.1

diameter. For CP-Ti, Hall-Petch coefficients of 204 to 1200 $\mu m^{1/2}$MPa have been reported, trending to higher k_{HP} values with higher interstitial content[163]. A constant value of 496 $\mu m^{1/2}$MPa was used[4].

To model the effect of interstitial carbon, nitrogen, oxygen, and hydrogen, the experimentally derived equations of Harwig et. al were used[195]. These equations use an oxygen equivalency equation in the style of Eq. 2.4 as well as a second order function of the yield stress increment. The coefficients of these equations were determined by performing regression on a large dataset of titanium properties.

To apply the Harwig model to the L-PBF data, measured interstitial concentrations in wt.% were converted using the modified oxygen equivalency:

$$\boldsymbol{O_{EQ} = [O] + 2.69[N] + 1.12[C] - 6.95[H]} \tag{4.1}$$

which has the associated second order yield strength improvement function:

$$\boldsymbol{\Delta\sigma_y^{O_{EQ}} = c_1(O_{EQ}) + c_2(O_{EQ})^2} \tag{4.2}$$

where the coefficients are $c_1 = 1011.74$ MPa(wt. %)$^{-1}$ and $c_2 = -528.24$ MPa(wt. %)$^{-2}$. In order to isolate carbon's contribution in this non-linear model, the yield stress increment from oxygen, nitrogen, and hydrogen with no carbon must be considered:

$$\boldsymbol{\Delta\sigma_y^{ONH} = \Delta\sigma_y^{O_{EQ}}([C] = 0)} \tag{4.3}$$

which can then be removed to isolate carbon's contribution:

$$\boldsymbol{\Delta\sigma_y^{C} = \Delta\sigma_y^{O_{EQ}} - \Delta\sigma_y^{ONH}} \tag{4.4}$$

The Hall-Petch model and Harwig oxygen equivalency model are linearly combined into:

$$\boldsymbol{\Delta\sigma_y^{total} = \Delta\sigma_y^{HP} + \Delta\sigma_y^{C} + \Delta\sigma_y^{ONH}} \tag{4.5}$$

Through this combined model, the yield stresses of 3 h at 700°C heat treated samples can be resolved into components. For simplicity of comparison, the minimum value of each component is subtracted out. For example:

$$\boldsymbol{\Delta\sigma_y^{HP,shown}([TiC]) = \Delta\sigma_y^{HP,calculated}([TiC]) - \min(\Delta\sigma_y^{HP,calculated})} \tag{4.6}$$

The yield stress increment is also normalized to pure titanium.

This model can explain the remarkable performance enhancement achievable through the addition of small amounts of TiC. By adding 0.5% TiC, strength was improved by 87% and ductility was also improved by 10%. This behavior does not follow the typical tradeoff of metallic materials where ductility must be sacrificed to increase strength. Yield strength decomposition shows the nature of this increase. The concentrations of oxygen, nitrogen, and hydrogen were all low and changed only slightly, so their effects were negligible. The majority of the improvement to yield strength was split between being due to grain refinement and carbon solid solution. These can both be attributed to the addition of TiC because the grain refinement was an effect of carbon promoting the martensitic transformation. However, while grain refinement normally decreases ductility, an increase in ductility is seen[163]. This implies that solid solution carbon is in fact increasing ductility. This phenomenon will be discussed in detail in the next chapter.

Tensile testing of samples heat treated for 3 h at 700°C showed increased strength and ductility compared to equivalent samples heat treated for 1 h at 500°C (Fig. 4.8). Properties are listed in Table 4.3. The overall trends in strength and ductility were as before, with the addition

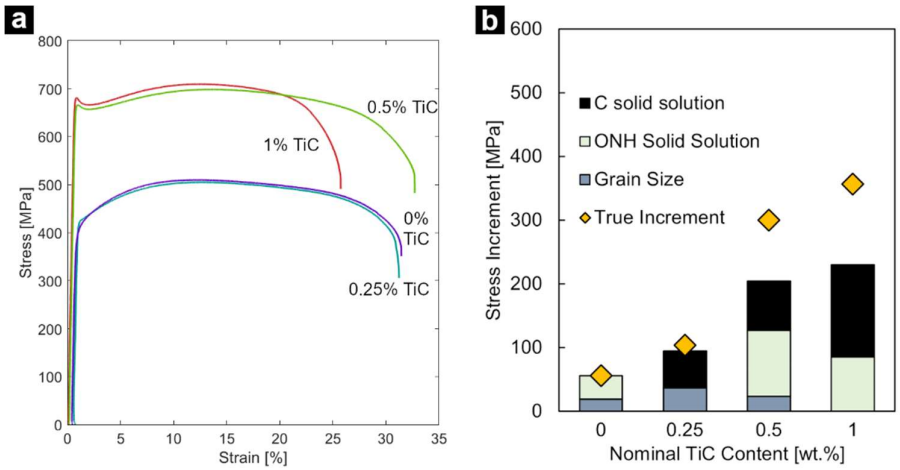

Figure 4.8: Mechanical properties of CP-Ti + *x*% TiC heat treated for 3 h at 700°C: a) tensile test stress-strain curves, b) yield stress decomposition.

Table 4.3: Mechanical properties of CP-Ti + *x*% TiC heat treated for 3 h at 700°C.

TiC addition [wt%]	Yield stress [MPa]	UTS [MPa]	Ductility [%]
0	385	497	29.8
0.25	433	513	32.4
0.5	629	665	32.2
1	688	713	23.4

of 0.5% TiC yielding dramatic improvement in strength but also increasing ductility. However, the high nitrogen content of these samples must be deconvoluted.

Yield stress decomposition was performed as before (Fig. 4.8b). The results still support that carbon has a significant effect on yield strength. However, the effect of nitrogen is also significant in the 0.5 and 1% TiC samples. The model underestimates the true yield stress in these two samples. However, unlike for the other samples, the tensile curves of both these high-nitrogen samples display a primary yielding hump and a secondary lower yielding. This suggests that the large amount of nitrogen changes the yielding mechanism of the material, preventing accurate interpretation by this model. If the effect of nitrogen is removed, the yield stress of the 0.5% TiC alloy is estimated as 430-526 MPa, and the yield stress of the 1% TiC alloy is estimated as 474-600 MPa. The lower bound is calculated by only using $\Delta\sigma_y^{HP}$ and $\Delta\sigma_y^{C}$ in the estimated yield stress value, and the upper bound is calculated by subtracting $\Delta\sigma_y^{ONH}$ from the measured yield stress. The large range of estimated yield stress is due to the large deviation between the model's estimated yield stress and the true yield stress.

4.4 Conclusions

Preliminary investigation into carbon solid solutions in titanium manufactured by L-PBF showed the potential of interstitial element in titanium alloys. Up to 1% TiC was added to CP-Ti and printed by L-PBF then heat treated for either 1 h at 500°C or 3 h at 700°C. The following conclusions were drawn:

- A complete solid solution of carbon in an α-Ti matrix is formed during L-PBF when up to 1% TiC is added to CP-Ti.

- The addition of any TiC led to the formation of a lamellar, martensitic microstructure in the as-printed material with the addition of more TiC yielding smaller laths.

- Heat treatment for 3 h at 700°C led to significant grain growth and a globular microstructure, with carbon promoting grain fusion.

- Tensile testing of samples heat treated for 1 h at 500°C, shows that TiC addition dramatically increases strength with negligible loss to ductility. The addition of 0.5% TiC led to an increase in yield strength from 392 to 679 MPa and an increase in ductility from 26.3% to 29.0%.

- Tensile testing of samples heat treated for 3 h at 700°C, also showed that up to 0.5% TiC addition can increase strength without loss of ductility. The addition of 0.5% TiC led to an increase in yield strength from 497 to 665 MPa and an increase in ductility from 29.8% to 32.2%.

Chapter 5:
L-PBF Soluted Carbon in Ti-6Al-4V

5.1 Experimental Overview

In this chapter, the effect of introducing a carbon solid solution into a Ti64 matrix is examined. This project explores the Ti64-TiC system without precipitation hardening and shows how post-processing and carbon content can be used to optimize mechanical properties using only solid solution strengthening.

This project had two parts. First, appropriate post-processing conditions were identified for L-PBF Ti64 + 0.75% TiC that would preserve the carbon solid solution and yield good mechanical properties. Only post-processing conditions were investigated because the optimal print conditions for Ti64 matrix materials have been thoroughly studied[116,123,135]. Next, TiC concentration was varied using these conditions to isolate the effect of the carbon solid solution on microstructure and mechanical performance.

5.2 Post processing of Ti64 + 0.75% TiC

5.2.1 Sample Preparation

During L-PBF, the laser induces localized heating and rapid cooling, allowing for the super-saturation of carbon. However, the imbalance in thermal expansion leads to high residual stresses and even deformation-induced defects. These residual stresses and certain defects, such as dislocations, strengthen the part, but they can also cause severe embrittlement. Post-processing must be carefully selected to alleviate embrittlement while minimizing sacrifices to

strength and increases to cost. For the purpose of isolating the effect of soluted carbon, the post-processing must also avoid precipitation of TiC.

For post-process investigation, 0.75% TiC was used in a Ti64 matrix. To ensure full TiC dissociation, a high VED of 162 J/mm^3 was used. The laser power was 160 W, the laser speed was 450 mm/s, the hatch width was 110 μm, and the layer thickness was 20 μm. Samples were printed without supports as 10×10×50 mm horizontally oriented bars and a 30×ϕ40 mm cylindrical billet. The bars underwent a comprehensive set of heat treatments listed in Table 5.1. The cylindrical billet was hot extruded as an alternative form of post-processing. It was pre-heated to 1100°C for 10 min before being quickly transferred to a hot extrusion press. The 2000 kN press extruded the hot billet through a round die to a diameter of 15 mm, an extrusion ratio of 7:1.

Table 5.1: Heat treatment conditions for Ti64+ 0.75% TiC.

Condition	Abbr.	Holding temperature [°C]	Holding time [min]	Approximate cooling rate [°C/s]
As-printed	AP	-	-	-
Stress relieved	SR	500	60	0.1
3 h temper	T3	700	180	0.1
12h temper	T12	700	720	0.1
24h temper	T24	700	1440	0.1
Furnace cooled	FC	1100	60	0.1
Air quenched	AQ	1100	60	10
Water quenched	WQ	1100	60	100
Water quenched + 3 h temper	WQT3	1100, 700	60, 180	100, 0.1
Hot extruded	Ex	1100	10	Extruded

5.2.2 Microstructure

All samples in this study showed a martensitic structure of the same texture before heat treatment (Fig. 5.1). To elucidate the martensitic texture, parent-β grains were mathematically reconstructed using titanium's preferential martensitic transformation planes: $\{110\}_\beta \rightarrow \{0001\}_{\alpha'}$ and $\{1\bar{1}1\}_\beta \rightarrow \{11\bar{2}\,0\}_{\alpha'}$. Reconstruction in monolithic Ti64 revealed a clear β texture of $\{100\}_\beta$ in the build direction (Fig. 5.1b). Within the build plane, the parent-β grains have no significant orientation. The parent-β grains are columnar in the build direction and have widths on the order of the 110 μm hatch spacing. The high vertical aspect ratio combined with vertical texture shows that during printing, the melt pool solidifies vertically, with $\{100\}_\beta$ as the

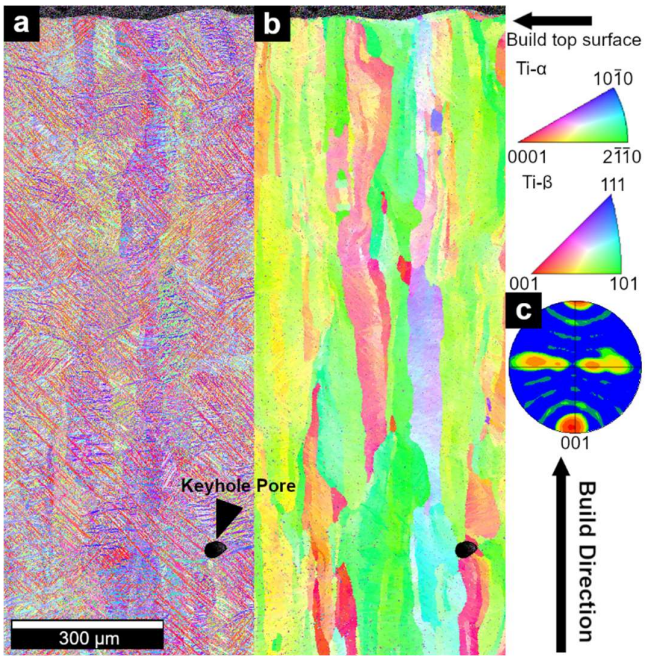

Figure 5.1: a) Characteristic martensitic structure near the build surface. b) Reconstructed parent-β grains. c) Pole figure of $\{001\}_\beta$ facets showing a strong texture in the build direction.

preferred grain growth direction. This columnar solidification mechanism is often found in L-PBF material with high energy densities[128,130], which is followed by a transformation to α′ martensite in Ti64[100]. This reconstruction method confirms that all grains in the true grain structure are oriented at angles consistent with a martensitic transformation.

Heat treatment of Ti64 + 0.75% TiC led to four distinct categories of microstructure (Fig. 5.2-3). The untempered acicular category is defined to include the as-printed, stress relieved, and water quenched samples. These conditions show a fine, martensitic-type grain structure that forms during the rapid cooling from L-PBF and water quenching. The as-printed case has fine, martensitic grains of relatively uniform width and a high aspect ratio, with the described $\{100\}_\beta$ texture. During L-PBF, each region is exposed to cyclic heating and cooling. Each cycle allows for additional martensitic transformation, leading to a relatively uniform α′ martensitic structure[100]. With the stress relieved heat treatment, there was a slight coarsening of the grains, but the overall microstructure was unchanged. Unlike the L-PBF cases, the water quenched case had a bimodal grain distribution, containing large martensitic laths with fine, poorly defined regions in between. This sample was normalized fully into the β phase before quenching, so it lost all of the L-PBF martensite. However, the lack of cyclic cooling allows for only primary and secondary martensitic structures[100]. The slower cooling of water quenching allows the primary martensitic grains to be larger than L-PBF laths. Notably, there was no evidence of TiC precipitation. The dissolved carbon remained stable in solution across high temperatures and phase changes.

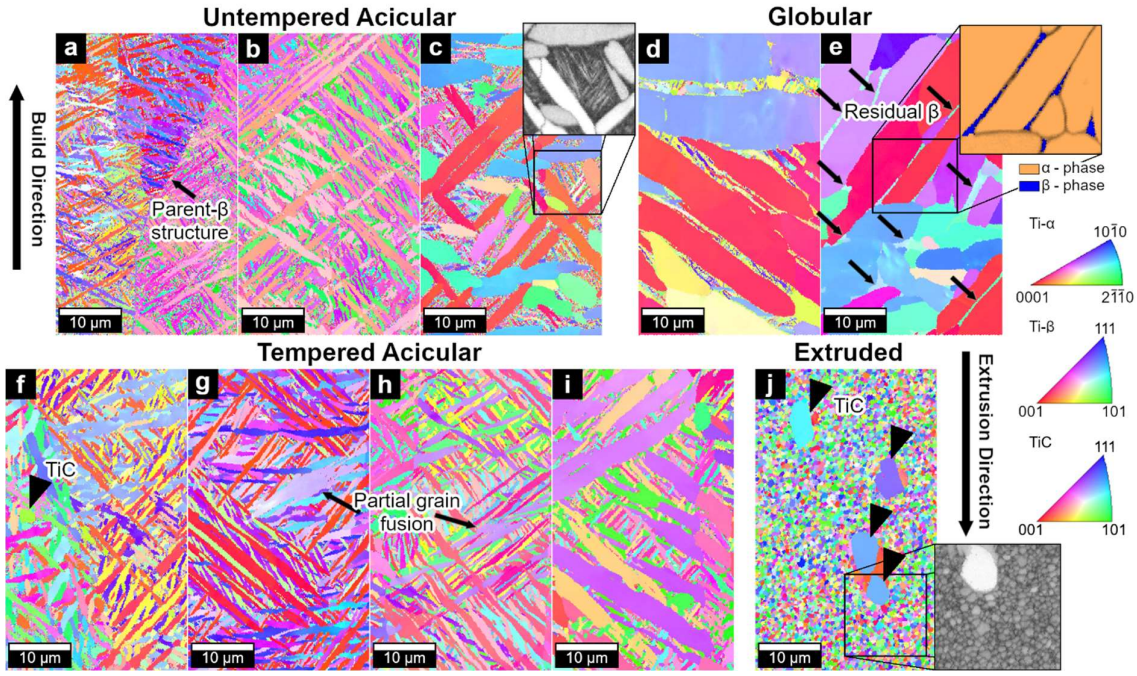

Figure 5.2: Vertical EBSD IPF maps of heat treated Ti64 + 0.75% TiC. a) As-Printed, b) Stress Relieved, c) Water Quenched with IQ inlay showing secondary martensite, d) Air Quenched, e) Furnace Cooled with combined phase map and image quality inlay, f) 3h Temper, g) 12h Temper, h) 24h temper, i) Water Quenched + 3h Temper, j) Hot Extruded with IQ inlay.

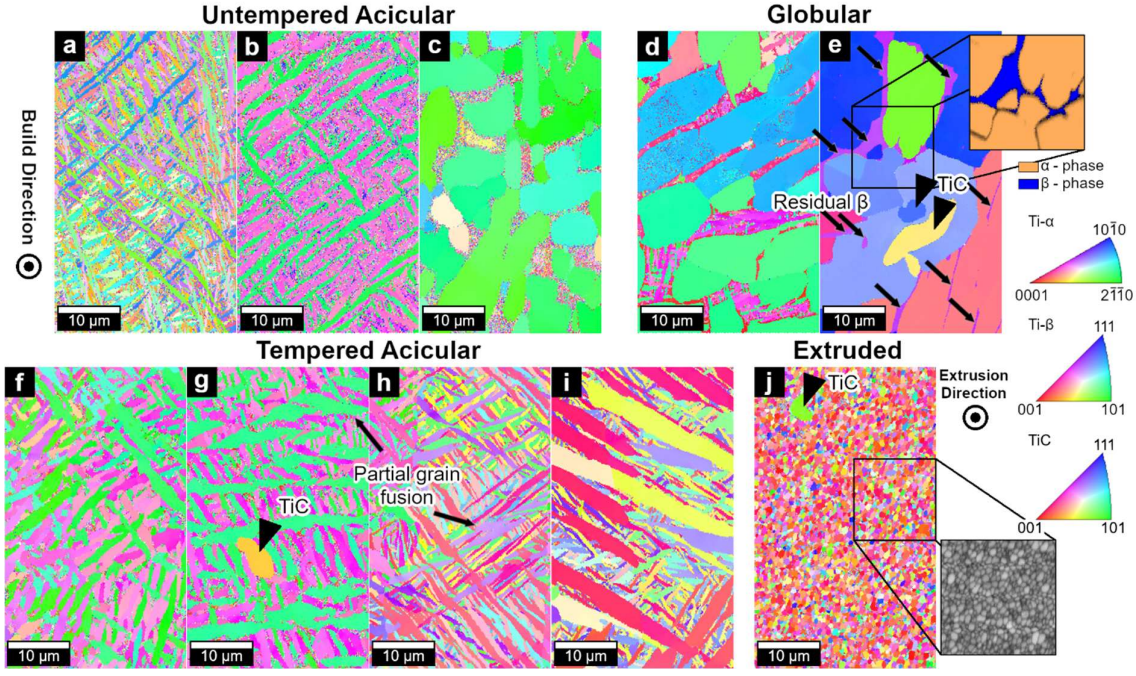

Figure 5.3: Horizontal EBSD IPF maps of heat treated Ti64 + 0.75% TiC. a) As-Printed, b) Stress Relieved, c) Water Quenched, d) Air Quenched, e) Furnace Cooled with combined phase map and IQ inlay, f) 3h Temper, g) 12h Temper, h) 24h temper, i) Water Quenched + 3h Temper, j) Hot Extruded with IQ inlay.

Air quenched and furnace cooled samples both have much larger, rounder grains, and are thus categorized as globular structures. These microstructures indicate dominance of a nucleation and growth mediated transition from the β-phase instead of a martensitic transformation. The parallel, high aspect ratio, large grains have a relatively even spacing with an intergranular region of a different phase. This implies a diffusion mediated pearlite-type growth behavior. In the air quenched samples, the cooling rate is fast enough such that the intergranular region contains martensitic structures. In the furnace cooled condition, the intergranular region remained in the β-phase. All residual β-phase shown has the same crystallographic orientation, indicating it is residual from a single massive β grain formed during heat treatment.

The tempered acicular category, which includes the 3 h, 12h, and 24h tempers as well as the water quenched + 3 h temper samples, shows martensitic structures similar to the untempered cases, but with coarser grains. Increasing the duration of the temper increases the degree of grain growth. By 12 hours of tempering, there is partial fusion of neighboring grains of similar orientation, which is further seen after 24 hours. When the water quenched sample is tempered for 3 hours, the secondary martensitic grains grow considerably. These secondary grains become much better defined by EBSD, indicating that defect-rich regions are annihilated or consumed by grain growth. The large primary grains grow as well, maintaining the bimodal α structure.

The hot extruded condition is categorized independently due to its finely sized but round grains and strong {0001} texture in the extrusion direction. The round grains are smaller than any acicular structure and have a relatively even size distribution. The hot working of extrusion induces dynamic recrystallization throughout the sample, and the metal flow causes the texture. Most notable is the prevalence of TiC precipitates. These precipitates occur at a high density, compared to only trace amounts of TiC being found in the as-printed condition and all other heat treatments. This indicates that the carbon precipitates out of solution during extrusion. While other samples had similar thermal histories without precipitation, it can be deduced that the massive deformation during extrusion provided the energy for nucleation of TiC particles. This sample can therefore be used to compare the effect of precipitation hardening versus solid solution strengthening on mechanical properties using a fixed carbon concentration.

5.2.3 Tensile Behavior

The tensile behavior followed the microstructural classifications (Fig. 5.4). The untempered acicular samples displayed the highest strengths, but by far the lowest ductility. As-printed, the alloy had a yield strength of 1267 MPa and a ductility of 3.1%. The stress relieved heat treatment removed the embrittling residual stresses inherent to L-PBF. This

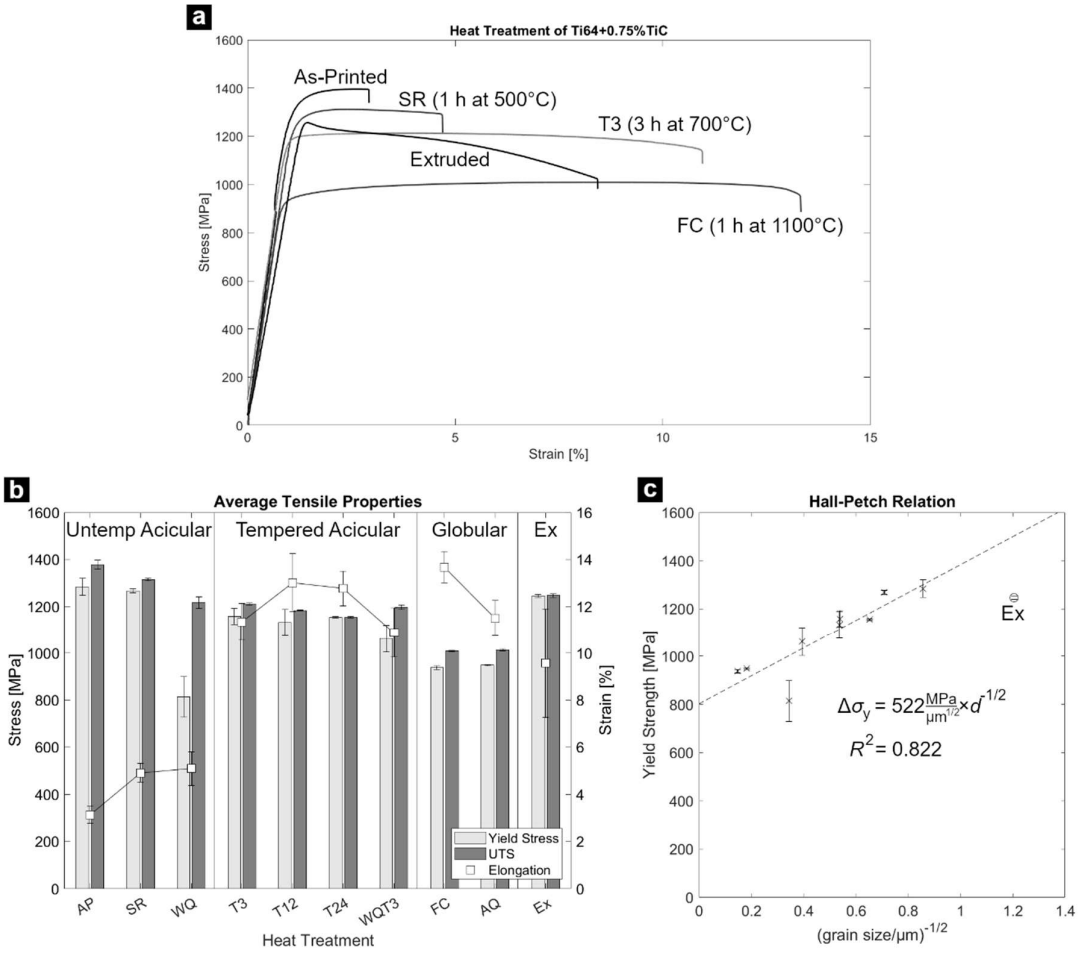

Figure 5.4: Tensile properties of heat treated Ti64 + 0.75% TiC. a) Representative tensile curves, b) average properties, c) Hall-Petch Correlation.

increased ductility by 57% with no change in yield strength compared to the as-printed condition. The water quenched sample had a yield strength that was 18% lower than the other two untempered acicular samples, despite having a ductility similar to the stress relieved condition. The reduction of yield strength can be attributed to the retained β-rich intergranular region, exemplifying how the hyper-rapid cooling conditions of L-PBF can produce extremely favorable microstructures for high-strength applications.

Once tempered, the acicular samples performed similarly irrespective of temper time or initial condition. The 3 h temper increases ductility by 280% from the as-printed state while reducing yield strength from 1267 MPa to 1172 MPa. Increasing the temper time from 3 to 24 hours only increases ductility by an additional 7%, indicating two main phases to the tempering process. In the first phase, which occurs within the first 3 hours, there is rapid annihilation of unnecessary residual stresses, dislocations, and other defects, slightly reducing yield strength and drastically improving ductility. In the second phase, defect annihilation slows and there is only moderate grain growth or grain fusion, which ultimately has little impact on the

mechanical properties. In the water quenched + 3 h temper sample, the β-rich intergranular region was replaced by martensitic structure, which significantly increased yield strength and ductility and allowed this condition to perform similarly to the other tempered acicular samples.

The remaining globular and extruded samples had poorer mechanical properties than previous samples. The large grains present in the globular samples led to low strength with no significant increase in ductility. While the extruded sample did display high strength and moderate ductility, it also had a very low work hardening rate and therefore necked immediately after yielding (Fig. 5.4a).

The Hall-Petch model (Eq. 4.1) is commonly used to predict how the yield strength σ_y of a material is changed as a function of average grain size $\bar{d}$. The Hall-Petch constant k_{HP} for this material can be calculated by using the various grain sizes and tensile results (Fig. 5.4c). The average grain diameter was chosen to represent grain size rather than the α-phase lath width, as not all samples had martensitic laths. As the extruded sample displayed a markedly different texture, plastic behavior, and carbon strengthening mechanism, it was not considered in the calculation. Linear regression of the remaining samples yielded:

$$\Delta\sigma_y^{HP} = 522 \frac{\mathbf{MPa}}{\mathbf{\mu m^{1/2}}} \bar{d}^{-1/2} \tag{5.1}$$

The coefficient of determination was R^2=0.822. The extruded sample has a much lower strength than what is predicted by the Hall-Petch function, showcasing how precipitation hardening is a less efficient strengthening mechanism than solid solution strengthening.

Of the post-processing methods examined, the stress relieved (1 h at 500°C) and 3 h temper (3 h at 700°C) heat treatments resulted in the best mechanical performance. With a heat treatment of 1 h at 500°C, the high strength of the as-printed condition was unchanged, and ductility was improved considerably, making it the most suitable for high-strength applications. All tempered acicular samples showed a similarly excellent balance of strength and ductility. The 3 h at 700°C treatment is most favorable, as it is the fastest and most efficient method to achieve this balance. Both the stress relieved and 3 h temper conditions were used for studying the effects of carbon concentration.

5.3 Varying TiC Content

5.3.1 Sample Preparation

For TiC variation experiments, TiC powder was added to Ti64 powder at concentrations of 0.25, 0.5, 0.75, and 1%, with monolithic Ti64 being used as a control. During L-PBF, a faster laser speed of 535 mm/s was used to reduce keyhole defect formation, yielding an invested energy density of 136 J/mm^3. The print parameters can be found in Table 3.1. A rectangular bar of each composition underwent each of the two optimized heat treatment conditions of 1 h at 500°C or 3 h at 700°C followed by furnace cooling.

5.3.2 Carbon Dissolution

TiC dissociated into a carbon solid solution through L-PBF across all tested compositions. While a few TiC particles could be found by microscopy, they were so dilute that their concentration could not be measured. Direct compositional measurement of carbon content shows that the carbon concentration of the printed and heat-treated material is consistent with the nominal amount of TiC added. Given that the added carbon is retained in the alloy after L-PBF, but TiC particles only occur in trace amounts, it can be concluded that the carbon has dissolved.

Lattice parameter analysis also supports carbon dissolution. Bragg's law (Eq. 3.2) was applied to the fitted XRD peaks to calculate the two lattice parameters *a* and *c*. In §4.2.2, carbon was shown to expand the *c*-axis in CP-Ti. The calculated lattice parameters of the Ti64 solutions show a steady increase in the *c*-lattice parameter of up to 1 pm and a steady decrease of the *a*-axis lattice parameter of 0.5 pm with the addition of up to 0.3% carbon from 1% TiC (Fig. 5.5). Increasing the heat treatment from 1 h at 500°C to 3 h at 700°C had no notable effect on the *a*-axis lattice parameter but caused the *c*-axis to expand as martensite relaxes into the α-phase. These correspond to a *c*/*a* ratio increase of 1.592 to 1.598 from 1 h at 500°C and 1.596 to 1.598 from 3 h at 700°C.

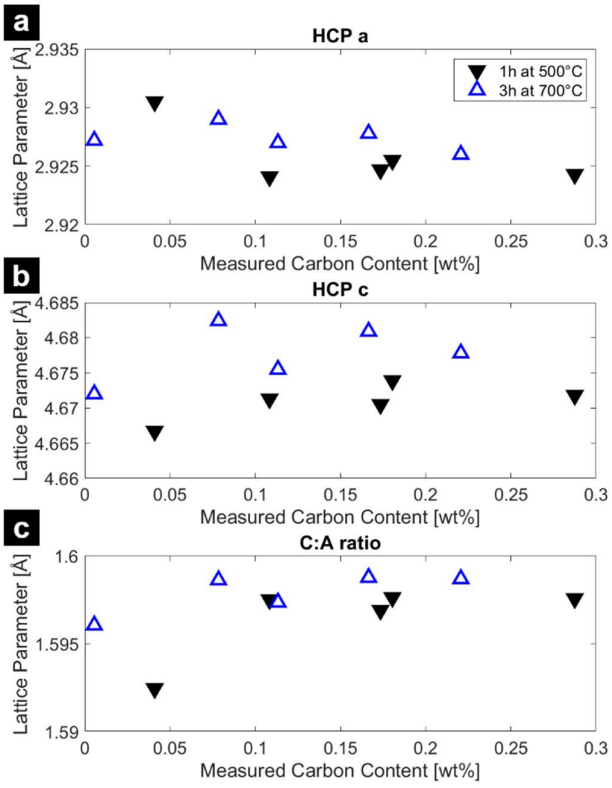

Figure 5.5: Lattice distortion as a function of carbon composition and heat treatment, as derived from XRD.

5.3.3 Microstructure

To better understand the heat-treated microstructure, the as-printed structure was examined first. In the as-printed condition, the addition of carbon led to finer grains. Average grain size decreased rapidly with small additions of TiC but had diminishing returns with larger additions of TiC (Fig. 5.6-7). Carbon appears to promote martensite nucleation, reducing lath width and length during L-PBF's rapid cooling. Other than grain size, there were no microstructural discrepancies between different compositions. The $\{100\}_\beta$ texture remains prevalent, as the addition of carbon has no significant effect on the parent-β grains.

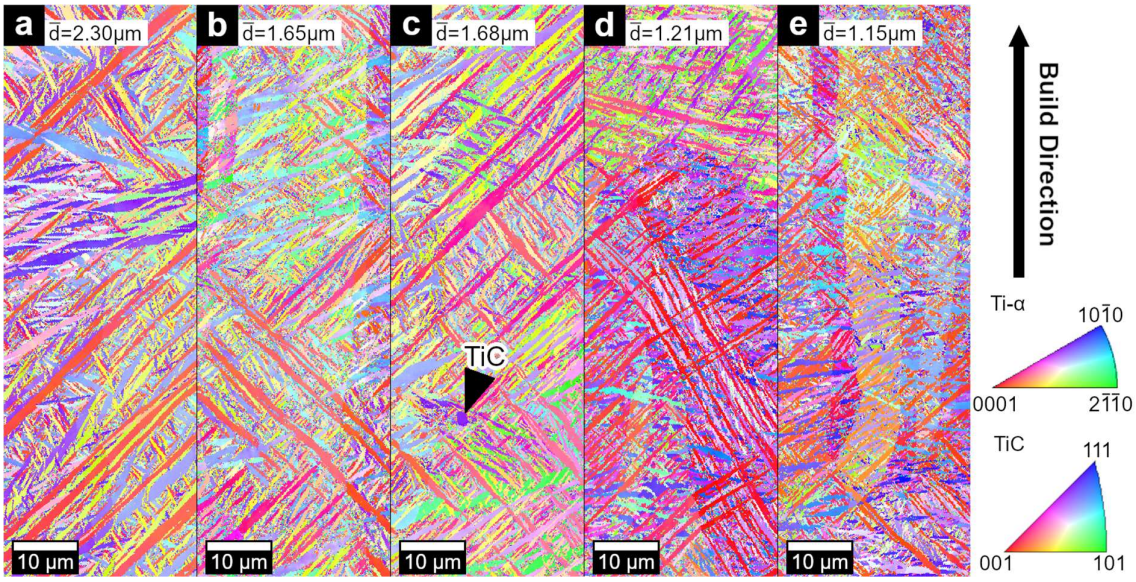

Figure 5.6: EBSD of vertical cross sections in the as-printed condition. a) 0%, b) 0.25%, c) 0.5%, c) 0.75%, e) 1% nominal TiC content.

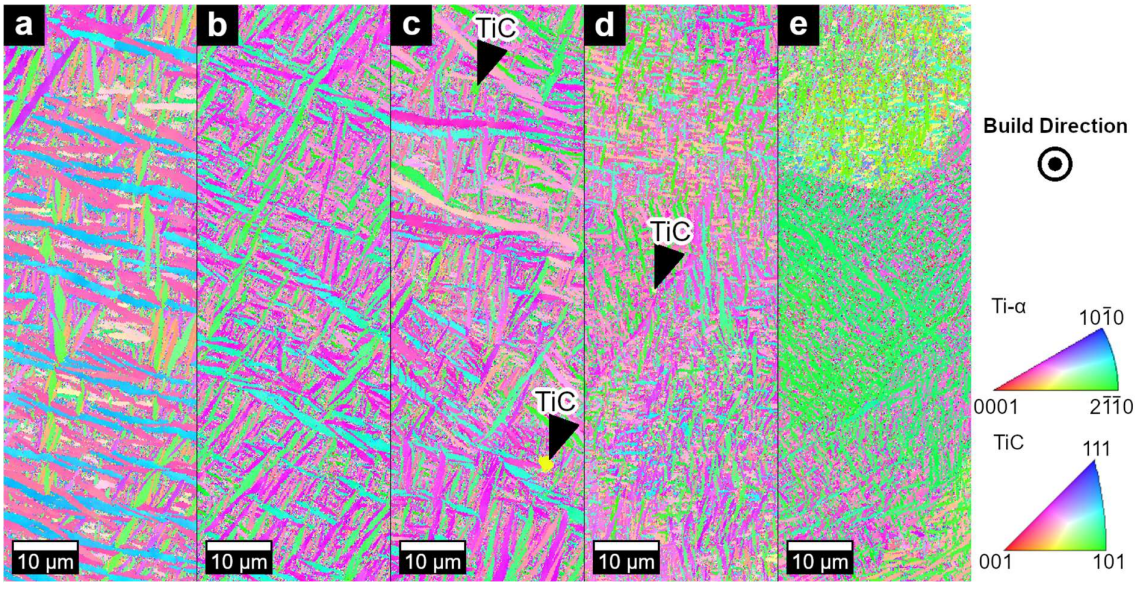

Figure 5.7: EBSD of horizontal cross sections in the as-printed condition. a) 0%, b) 0.25%, c) 0.5%, c) 0.75%, e) 1% nominal TiC content.

With a heat treatment of 1 h at 500°C, the grain structure remains similar to the as-printed condition, albeit with mild grain growth (Fig. 5.8-9). As there is no phase change, texture is also unchanged. There is only a slight increase in average grain size across all TiC compositions due to the slow grain growth rate at 500°C. In addition to grain growth, another factor contributing to the increased average grain size was the annihilation of defect rich regions at the grain boundaries. During heat treatment, these regions are absorbed by the neighboring grains. Defect annihilation increased EBSD quality, allowing for previously unreadable regions to contribute to grain size.

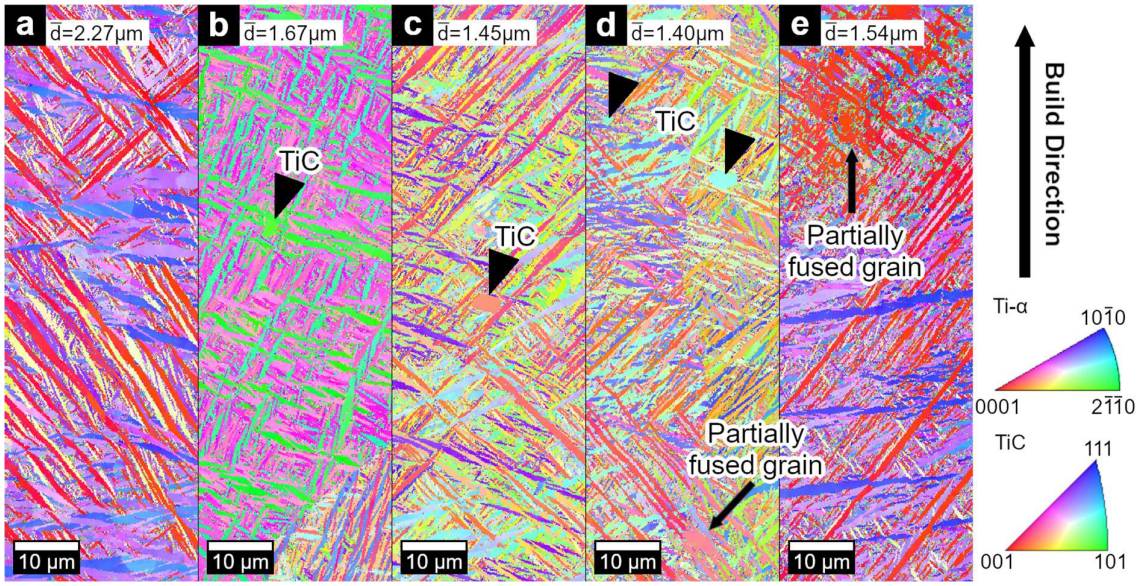

Figure 5.8: EBSD of vertical cross sections after 1h at 500°C heat treatment. a) 0%, b) 0.25%, c) 0.5%, c) 0.75%, e) 1% nominal TiC content.

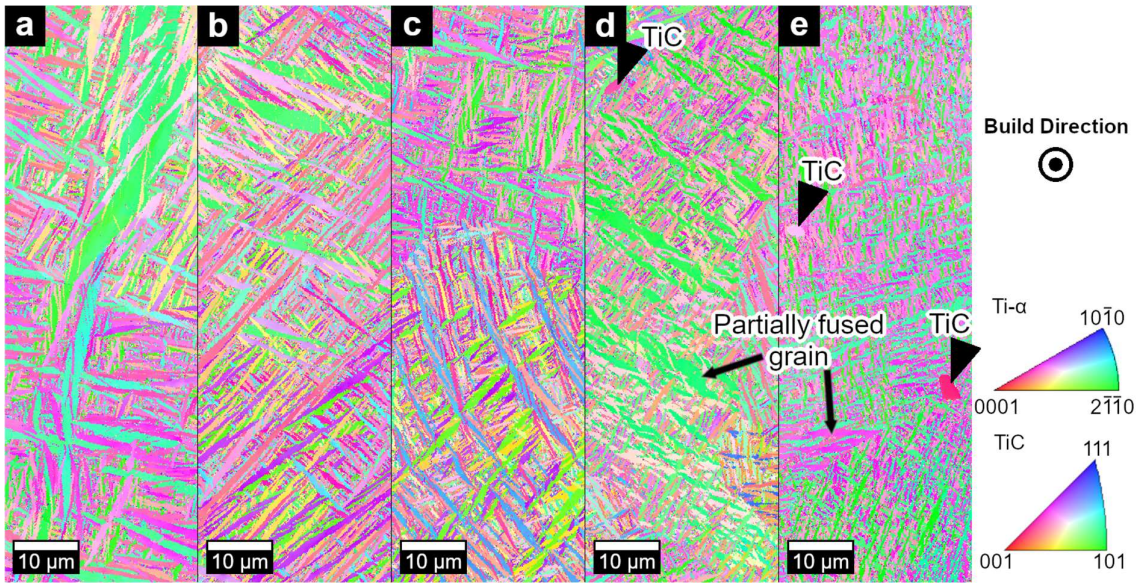

Figure 5.9: EBSD of horizontal cross sections after 1h at 500°C heat treatment. a) 0%, b) 0.25%, c) 0.5%, c) 0.75%, e) 1% nominal TiC content.

The 3 h at 700°C heat treatment induces more significant grain growth, which is assisted by the addition of carbon (Fig. 5.10-11). With increased heat treatment time and temperature, grains grow faster in all directions, increasing average grain size and lath width. There was more grain growth with higher carbon content, indicating that carbon facilitates grain growth. Carbon has a fast diffusion rate in Ti64, preventing solute drag[161,196]. At TiC concentration of 0.75% and 1%, grain growth was such that parallel martensitic grains with similar orientations were able to fuse together into significantly larger grains (Fig. 5.10e). Carbon induces finer grains in the as-printed condition but increases grain size by promoting grain fusion during heat

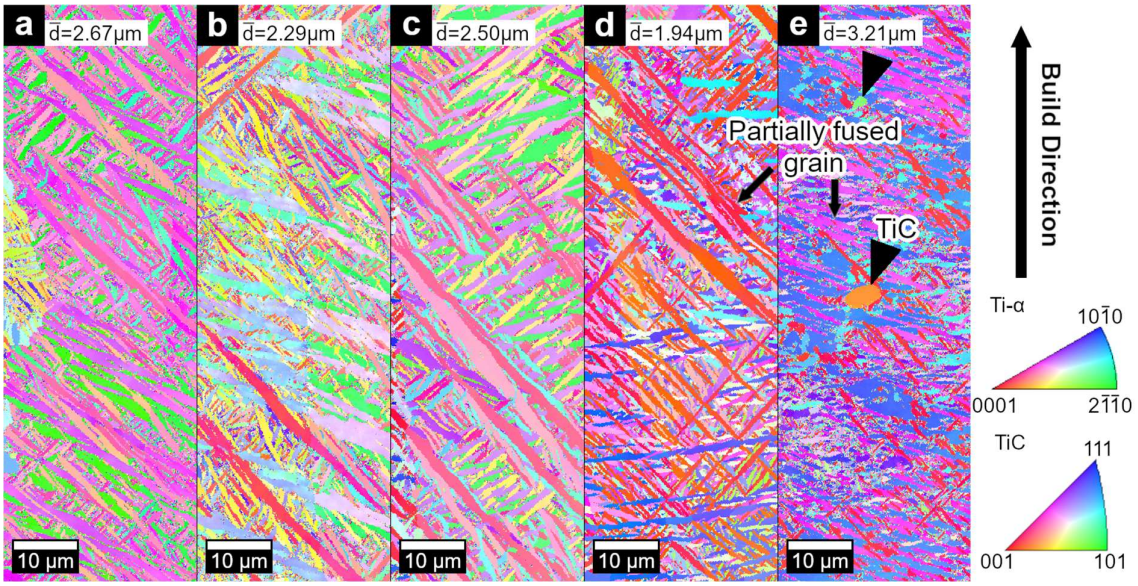

Figure 5.10: EBSD of a vertical cross section after 3h at 700°C heat treatment. a) 0%, b) 0.25%, c) 0.5%, c) 0.75%, e) 1% nominal TiC content.

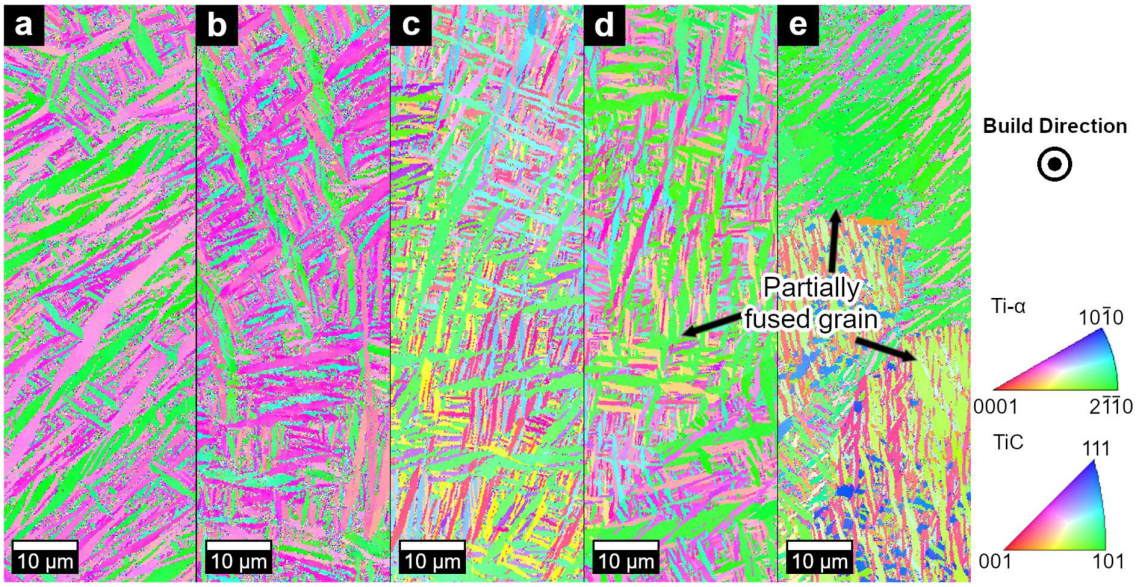

Figure 5.11: EBSD of a horizontal cross section after 3h at 700°C heat treatment. a) 0%, b) 0.25%, c) 0.5%, c) 0.75%, e) 1% nominal TiC content.

treatment. This led to a curved average grain size distribution after 3 h at 700°C with a minimum at 0.25% TiC (Fig. 5.12). Grain size average and standard deviation were calculated from the combination of 30×90 µm horizontal and vertical sections.

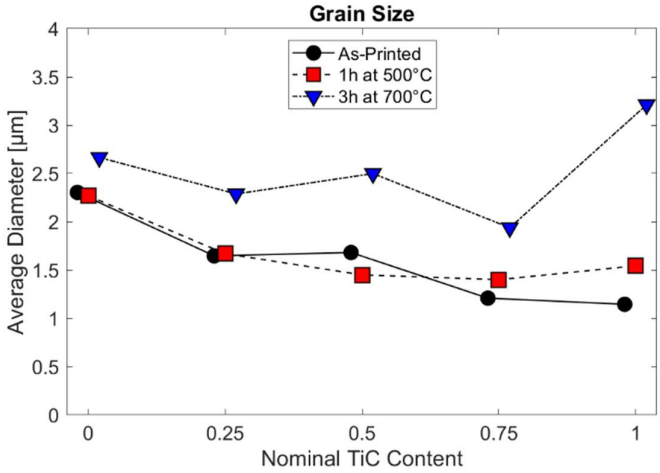

Figure 5.12: Average grain size vs TiC content in the as-printed case and both heat-treated cases. Plots are slightly offset to show detail.

5.3.4 Tensile Behavior

The retained dislocations and defects of the 1 h at 500°C condition led to extremely high yield strengths while still allowing for some ductility. Average properties are listed in Table 5.2, with stress-strain curves shown in Fig. 13 and Fig. 14. The properties of monolithic Ti64 are consistent with the literature for the stress relieved martensite microstructure[135]. The addition of carbon in this heat treatment unilaterally led to increased strength and decreased ductility. The addition of TiC led to a 27% increase in yield strength, larger than what can be achieved in Ti64 through microstructural refinement alone. While ductility decreased at higher

Table 5.2: Average mechanical properties.

Heat treatment	Nominal TiC content [wt.%]	Yield stress [MPa]	Ultimate tensile stress [MPa]	Elongation at fracture [%]
1 h at 500°C	0	1130±9	1225±2	8.0±0.7
	0.25	1167±14	1249±2	8.0±0.7
	0.5	1236±12	1308±11	6.7±0.5
	0.75	1298±31	1405±2	4.6±0.3
	1	1429±49	1490±8	3.0±0.4
3 h at 700°C	0	1053±12	1119±7	11.0±0.6
	0.25	1089±22	1161±6	11.2±0.7
	0.5	1139±8	1170±6	11.5±0.4
	0.75	1213±15	1242±8	9.7±0.3
	1	1247±3	1262±1	8.1±0.7

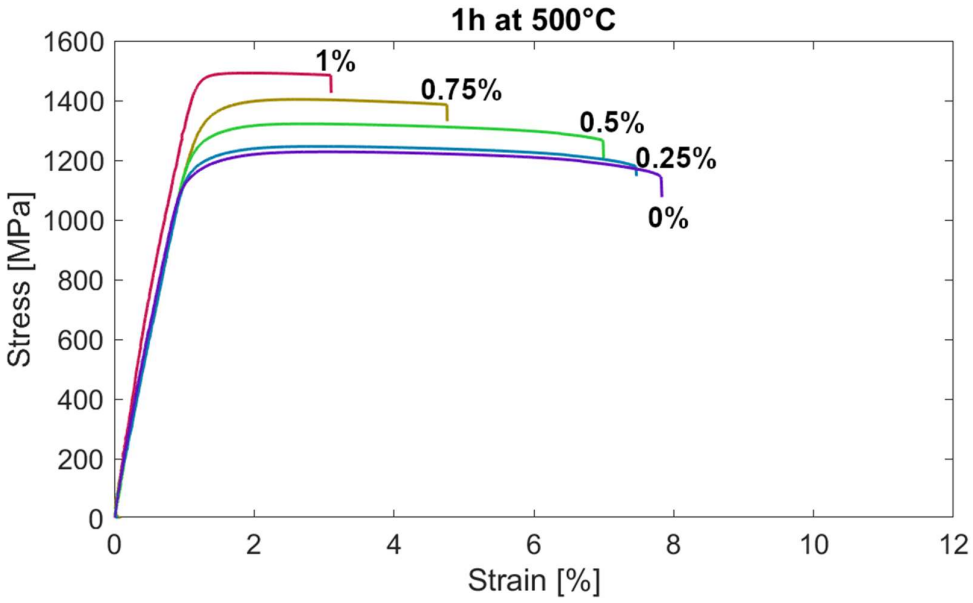

Figure 5.13: Representative tensile tests of the 1 h at 500°C heat treatment.

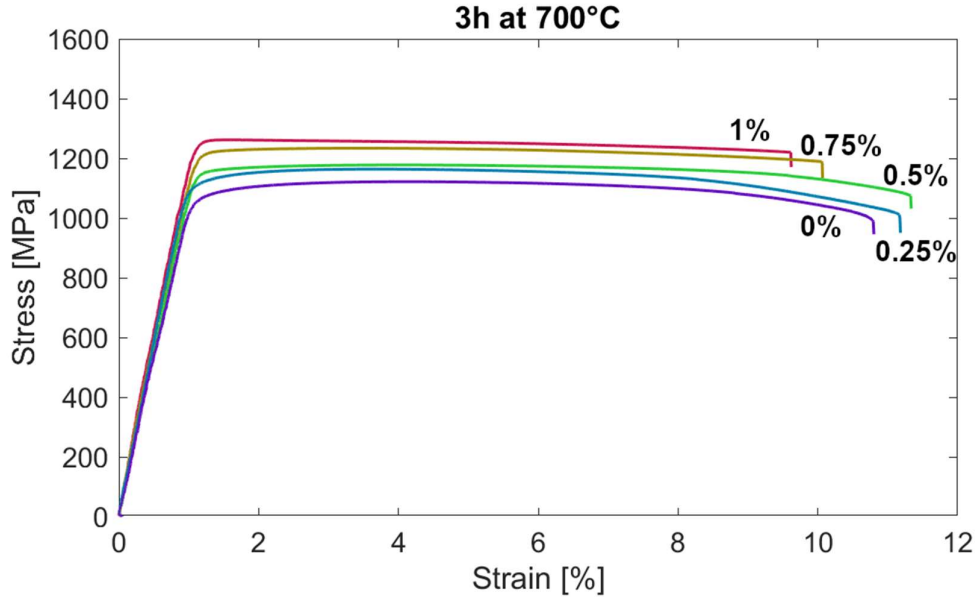

Figure 5.14: Representative tensile tests of the 3 h at 700°C heat treatment.

carbon concentrations, even the highest strength sample showed some plastic deformation, making this a superior set of alloys for high-strength applications.

Tempering the printed material yields a dramatic increase in ductility at a slight cost to strength. With no addition of TiC, Ti64 has a 38% increase in ductility with a 7.6% decrease in yield strength when exposed to the longer 3 h at 700°C heat treatment. Remarkably, the addition of up to 0.5% TiC increased both strength and ductility compared to monolithic Ti64. At higher TiC concentrations, strength continued to increase, but ductility began to decrease

slowly. Notably, ductility in the 3 h at 700°C condition was higher than in the 1 h at 500°C condition at comparable strengths.

The mechanical properties of the 0.75% TiC samples printed with a laser speed of 535 mm/s can be compared to those from the §5.2.3 printed at 450 mm/s (Fig. 5.4). With a heat treatment of 1 h at 500°C, increasing the laser speed increased yield stress by 6% and decreased ductility by 3%. With a heat treatment of 3 h at 700°C, increasing the laser speed increased yield stress by 3% and decreased ductility by 6%. These changes are consistent with a decrease in keyhole porosity and an increase in residual stresses at faster laser speeds.

5.3.5 Strengthening Mechanisms

TEM imaging of 0.5% TiC samples show how heat treatment affects the dislocation density and leads to the shown mechanical properties (Fig. 5.15). As-printed, both entangled dislocation networks and twins can be observed. The localized heating of L-PBF causes deformation from thermal expansion, leading to dislocation formation. While Ti64 does not readily form twins under normal deformation, the hyper-rapid nature of the cooling increases thermal expansion strain rate, encouraging twinning[46]. After 1 h at 500°C, twins can no longer

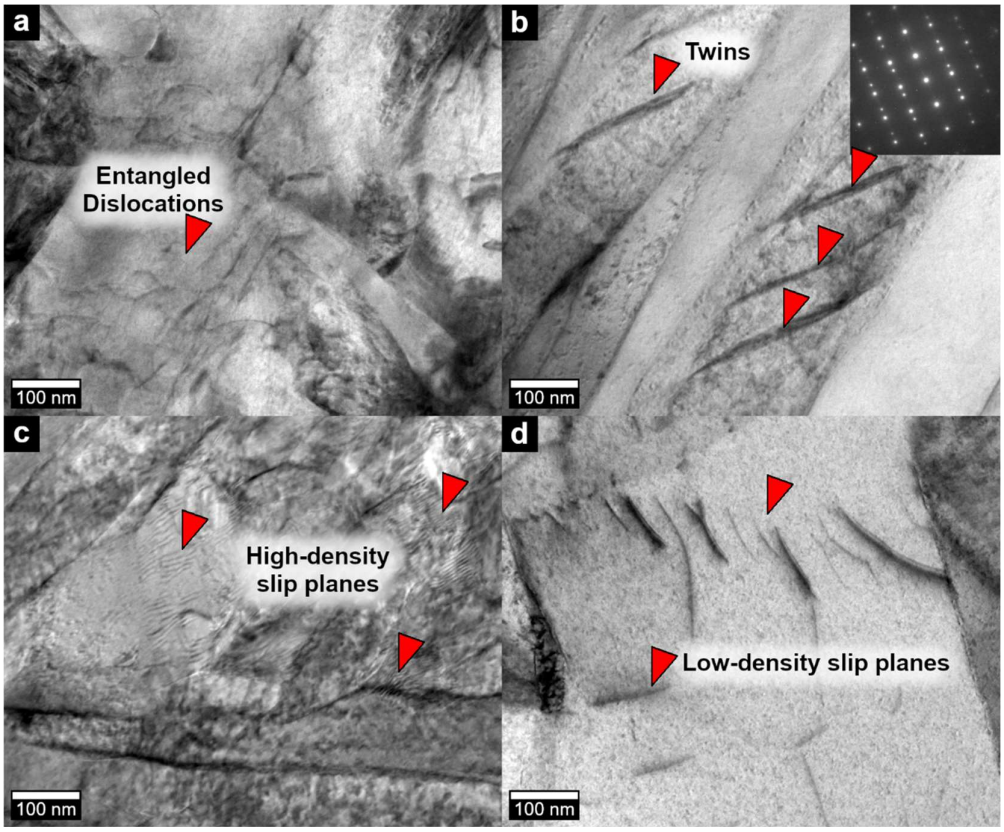

Figure 5.15: 200kx magnification TEM of dislocation densities in Ti64 + 0.5% TiC. a) Entangled dislocation network in as-printed condition. b) Twinning in as-printed condition with SAD inlay. c) Preferential dislocation slip planes after 1h at 500°C. d) Slip planes after 3h at 700°C.

be found, and the previously chaotic dislocation networks align along preferential slip planes. By 3 h at 700°C, the dislocations still appear along preferential slip planes, but their density has been reduced dramatically. This dislocation density reduction is consistent with the reduced strength and improved ductility from the 1 h at 500°C samples. The samples were carefully examined under TEM for nano-TiC precipitates, but none were found in the as-printed sample or after either heat treatment. This confirms the stability of the carbon solid solution.

To examine how carbon concentration affects mechanical properties, the yield stress decomposition model (Eq. 4.6) discussed in §4.3 was used. Measured interstitial compositions for the calculation of $\Delta\sigma_y^C$ and $\Delta\sigma_y^{ONH}$ are listed in Table 5.3 and Fig. 5.16. $\Delta\sigma_y^{HP}$ was calculated using the Hall-Petch relation derived in Equation 5.1. The minimum value of each component was subtracted out as before (Eq. 4.7).

Table 5.3: Interstitial composition.

Heat treatment	Nominal TiC content [wt.%]	Carbon [wt.%]	Oxygen [wt.%]	Nitrogen [wt.%]	Hydrogen [wt.%]
1 h at 500°C	0	0.041±0.005	0.241±0.025	0.025±0.005	0.011±0.002
	0.25	0.108±0.008	0.211±0.003	0.033±0.003	0.010±0.001
	0.5	0.174±0.010	0.208±0.009	0.022±0.003	0.009±0.001
	0.75	0.180±0.009	0.232±0.004	0.067±0.005	0.007±0.003
	1	0.288±0.007	0.224±0.006	0.027±0.003	0.007±0.0003
3 h at 700°C	0	0.006±0.001	0.261±0.011	0.040±0.012	0.006±0.0004
	0.25	0.078±0.008	0.245±0.013	0.027±0.001	0.006±0.0006
	0.5	0.113±0.005	0.252±0.008	0.039±0.006	0.006±0.0002
	0.75	0.167±0.012	0.230±0.006	0.049±0.015	0.008±0.0002
	1	0.221±0.010	0.264±0.008	0.053±0.006	0.006±0.0002

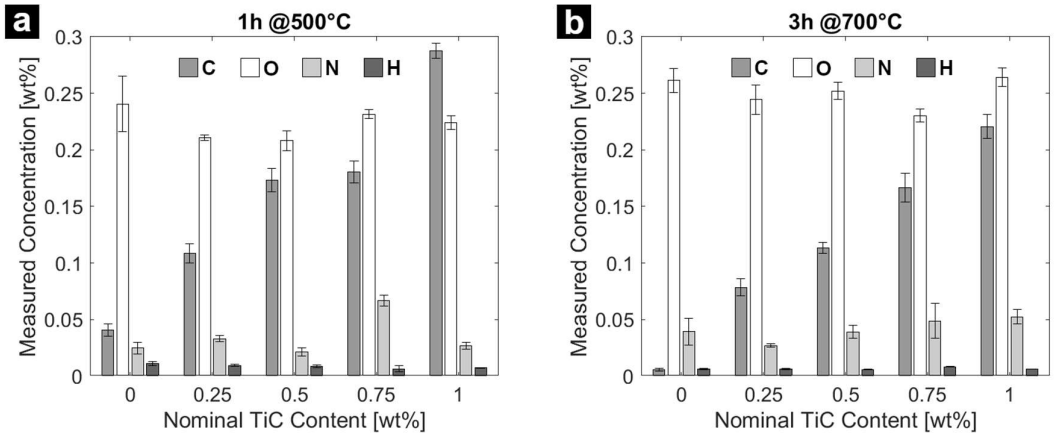

Figure 5.16: Carbon, oxygen, nitrogen, and hydrogen content of each sample heat treated at a) 1 h at 500°C, b) 3 h at 700°C.

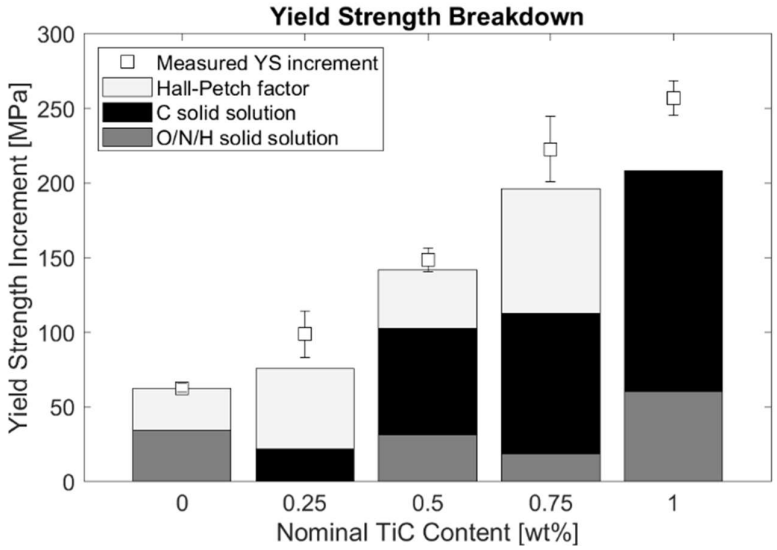

Figure 5.17: Decomposition of the yield stress increment into grain size and solid solution strengthening components by Hall-Petch and experimental models.

Through this combined model, the yield stresses of 3 h at 700°C heat treated samples can be resolved into components (Fig. 5.17). The yield stress increment is also normalized to monolithic Ti64. It can be seen that solid solution strengthening is the dominant strengthening mechanism and increases with TiC concentration. The largest deviation in experimental yield stress from the model comes at 1% TiC, where strength is underestimated. This discrepancy is due to the unusual morphology of the large, fused grains. As they retain some features from their martensitic components, they have a very high grain boundary area for their size. As grain boundaries are obstacles to dislocation motion, this fused morphology has an increased strengthening potential. The Hall-Petch model assumes convex grains with a low aspect ratio and low grain boundary area, causing it to underestimate the yield stress increment.

Strain hardening rate analysis provides some insight into the mechanism of the ductility improvement shown in 0.25% and 0.5% TiC samples after 3 h at 700°C (Fig. 5.18). The initial strain hardening rate at the onset of plastic deformation is lower for high-carbon samples due to higher yield stresses. Carbon's notable effect comes after yielding, where the strain hardening rate is more stable with increased carbon content. This strain hardening stabilization effect increases the strain value of the x-intercept, an indication of the onset of necking. By delaying necking, carbon addition is able to improve ductility as well as strength.

To understand the stabilization mechanism, EBSD analysis was performed on tensile specimens after fracture in the uniform deformation bulk regions (1.5 mm from fracture) and necking region adjacent to the fracture surface. Schmid factor analysis was then calculated by the EBSD software using basal {0001} and prismatic $\{1\bar{1}00\}$ slip of *a*-type ($\mathbf{b}=\langle 11\bar{2}\,0\rangle$) dislocations, as those are the dominant slip systems in Ti64[43]. For comparison, the area of low

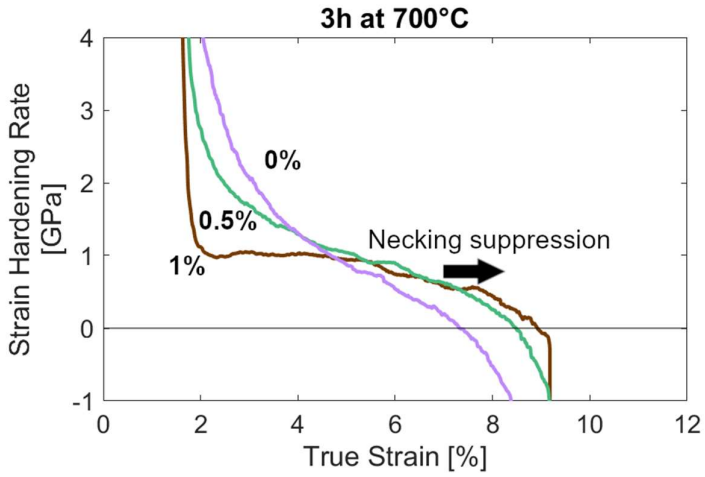

Figure 5.18: Calculated strain hardening rates of representative tensile tests.

(*SF*<0.3), medium (0.3≤*SF*<0.4), and high (0.4≤*SF*≤0.5) Schmid factor for each slip system was calculated. The ratio of prismatic area (Fig 5.19) to basal area (Fig. 5.20) was calculated for each Schmid factor bin (Fig. 5.21). In the uniform deformation bulk regions, the as-printed texture is retained. The dominance of prismatic area in the medium Schmid factor bin but basal area in the high Schmid factor bin is attributed to this texture. There were no significant trends in the uniform deformation region.

In the necking region, deformation is sufficient for grains to reorient slightly such that dominant slip systems have higher Schmid factors. With no added TiC, Ti64 experiencing necking shows preferred deformation along the prismatic slip system. Microvoids near the fracture surface can also be observed in prismatic slip areas (Fig. 5.19d), indicating that is where plastic deformation is higher. With the addition of carbon, reorientation towards prismatic slip is reduced. With 0.5% TiC, there is still a slight reorientation of grains, as evidenced by the trend in Schmid factor area ratio (Fig. 5.21b), but it is significantly reduced from the 0% TiC condition. The 1% TiC sample fractured almost immediately after the onset of necking (Fig. 5.19f), so there was insufficient plasticity to induce grain reorientation. Therefore 1% TiC shows no preference towards prismatic slip at the fracture surface.

It has been suggested that prismatic slip is more strongly pinned by interstitial atoms than basal slip[157,162,191]. Furthermore, prismatic slip through an interstitial site has been shown to induce a preferential slip plane[162]. Planar dislocation slip causes dislocation pileup, which may lead to crack or microvoid initiation, reducing ductility. Therefore, it is proposed that the addition of dissolved carbon is able to improve both strength and ductility by suppressing prismatic slip.

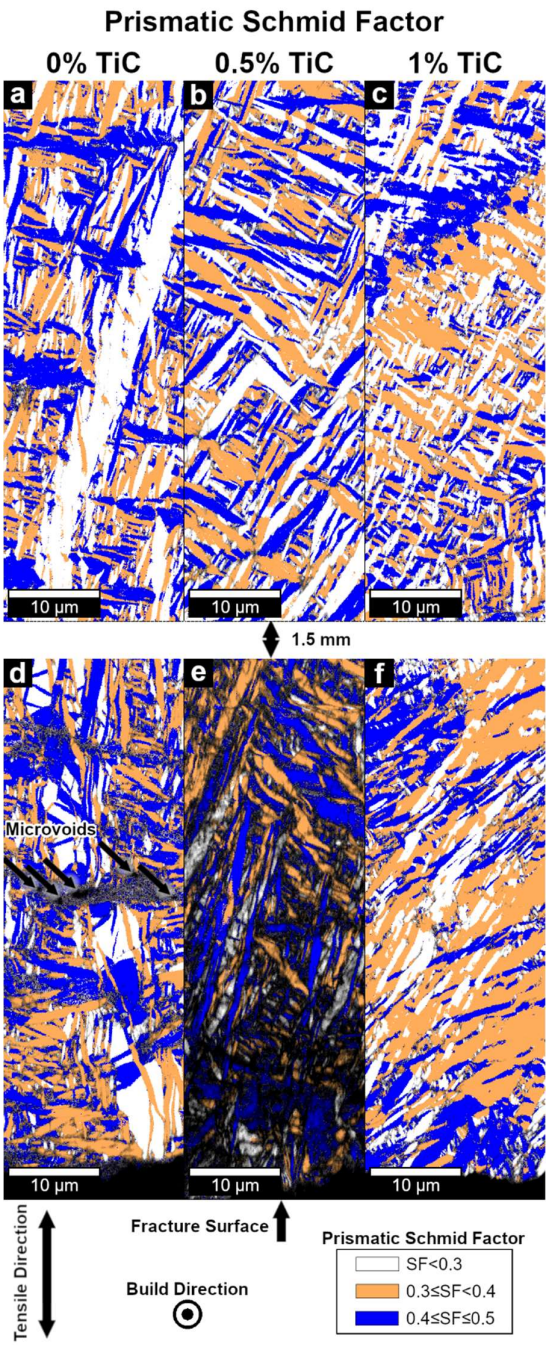

Figure 5.19: Build plane false-color prismatic Schmid factor mapping with image quality overlay with a, d) 0%, b, e) 0.5%, and c, f) 1% TiC addition. a-c) the homogeneous deformation region. d-f) the necking region.

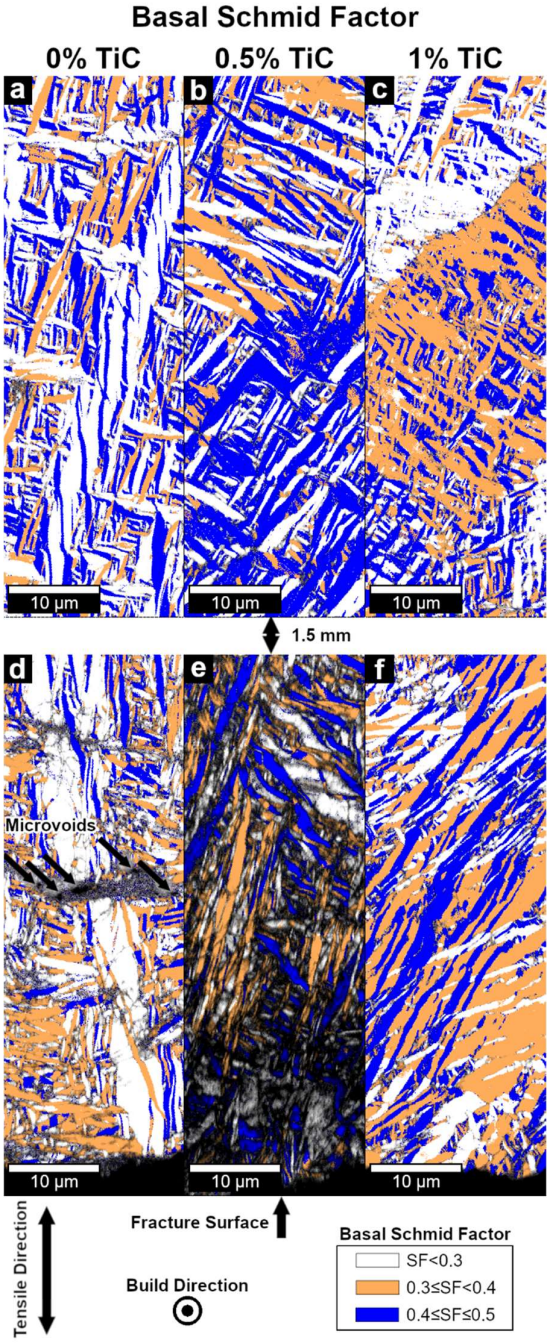

Figure 5.20: Build plane false-color basal Schmid factor mapping with image quality overlay with a, d) 0%, b, e) 0.5%, and c, f) 1% TiC addition. a-c) the homogeneous deformation region. d-f) the necking region.

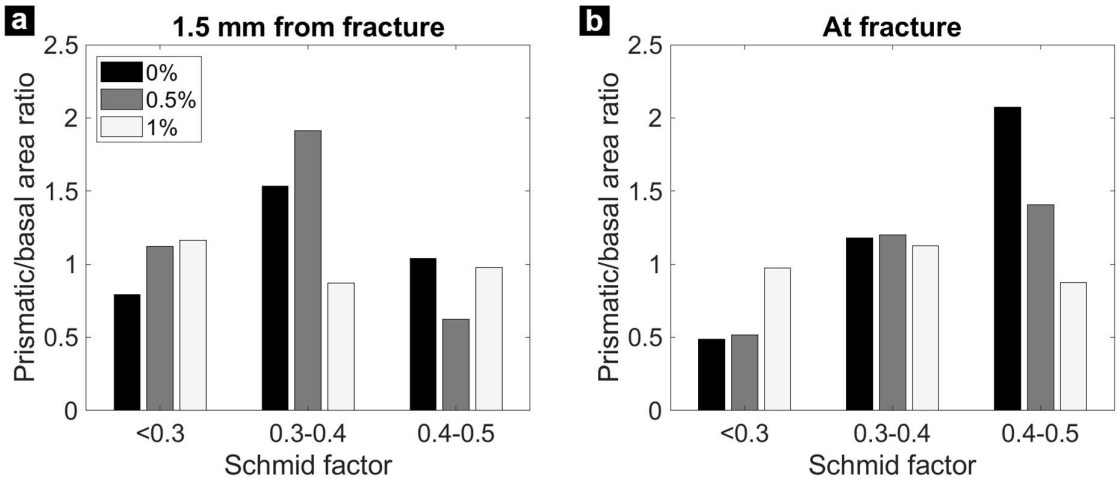

Figure 5.21: Prismatic to basal area fraction ratios for each Schmid factor range for a) the homogeneous deformation region and b) the necking region.

5.4 Conclusions

Ti64 was processed with small amounts of TiC using L-PBF to create carbon solid solutions with excellent mechanical properties. Appropriate post-processing conditions were determined for the optimization of mechanical performance. Carbon addition was found to be an effective method for safe, low-cost improvement of L-PBF Ti64's mechanical properties. The nature of carbon's improvement of a Ti64 matrix was successfully determined. Through microstructural characterization and mechanical testing, the following conclusions were obtained:

- Dissolving 0.75 wt.% TiC into Ti64 using L-PBF yields a solid solution that is stable for at least 1 h at 1100°C or 24 h at 700°C, but the TiC will precipitate out during hot extrusion.
- Suitable heat treatments for this material are 1 h at 500°C for high strength and 3 h at 700°C for a good balance of strength and ductility.
- Dissolved carbon refines the martensitic grain size but promotes grain fusion during heat treatment.
- With 1 h at 500°C heat treatment, high strengths of up to 1490 MPa could be achieved through 1% TiC addition.
- With 3 h at 700°C heat treatment, carbon can increase both the strength and ductility of Ti64 when up to 0.5 wt.% is added.
- The improvements in strength are attributed to solid solution strengthening and slight grain refinement.
- The improvements to ductility are explained by carbon's preferential pinning of prismatic dislocation slip, which then inhibits necking.

Chapter 6:
Processing, Texture, and Carbon in L-PBF Ti-10Mo

6.1 Experimental Overview

This chapter investigates the development of optimal processing parameters for L-PBF titanium with 10 wt.% molybdenum (Ti-10Mo) as well as the impact of TiC addition. As discussed in §2.1.4, Ti-10Mo has a much higher β-phase stability than either CP-Ti or Ti64. It also differs from the previous two systems because Ti-10Mo is not a mass-produced alloy. Instead, it can be produced in-situ from a mixture of CP-Ti powder with pure Mo powder. As a bespoke alloy, it does not have commercially optimized process parameters. The first part of this chapter details the optimization of print parameters and post-processing of Ti-10Mo for excellent homogeneity and mechanical properties. Once the process conditions are fixed, the second part of this chapter shows the impact of a carbon solid solution on this alloy.

6.2 Process Optimization

6.2.1 Print Parameter Observation and Texture Mapping

While any number of print parameters could be investigated, it was desirable to keep most parameters constant due to the specifications of the printer itself. Laser speed v and VED were chosen as the parameters of interest due to their large range of printable values, excellent documentation in the literature, and significant effect on melt pool behavior, microstructure, and mechanical properties.

An array of 10×10×10 mm cubes was printed using scan speeds of 500, 800, 1000, 1500, 2000, and 2500 mm/s and VEDs of 50, 70, 90, 110, 130, and 150 J/mm^3. No cubes were printed at scan speeds of 500 or 2500 mm/s for VEDs of 50 and 70 J/mm^3 due to the low print

quality. All cubes were cut in half along the build planes and lightly polished on the build plane before undergoing XRD using Cu K_α radiation. Representative samples and extreme cases were imaged by EBSD. For comparison, a 0.5×1 mm IPF image was taken of the build plane of each sample at a 2 μm resolution. The multiples of uniform distribution (MUD) texture value was calculated by the EBSD analysis software using a harmonic series expansion with 5.0° gaussian smoothing.

EBSD revealed that Ti-10Mo displays three different as-printed microstructures under the parameters studied (Fig. 6.1). EBSD of samples that characterize the oriented, semi-oriented, and misoriented microstructures are shown in Fig. 6.2. These microstructures can be most readily quantified by the maximum MUD texture value T of the 0.5×1 mm build plane image. The observed samples and resulting microstructure are listed in Table 6.1. Oriented samples (Fig. 6.2a) had large, columnar grains and a strong texture of $T \geq 5$ times uniform distribution. The grains had dimensions of 20 μm in the build plane and a height in the build direction on the order of 50-500 μm. The grains showed a significant {100} texture in the build plane, which is typical for columnar growth of β-Ti[118,197]. This microstructure was observed when scan speed was less than 1500 mm/s and VED was at least 90 J/mm^3.

Misoriented samples (Fig. 6.2c) were defined by $T \leq 3$ times uniform distribution. While the grains showed no texture, they were also not equiaxed, as they were approximately 20 μm tall in the build direction, but 2-10 μm wide in the build plane. A large fraction of the misoriented samples, shown as black regions, could not be indexed, which preventing rigorous measurement of the grain size. These regions are caused by nanoscale α″ and ω grains disrupting the diffraction pattern[72,74,75]. The misoriented microstructure was observed when scan speed was at least 1500 mm/s or VED was less than 90 J/mm^3, and no significant variation was found across the misoriented samples. The intermediate, semi-oriented microstructure had a texture of between 3- and 5-times uniform distribution (Fig. 6.2b). This microstructure had grain sizes closer to the misoriented cases but retained the preferential {100} texture of the oriented microstructure.

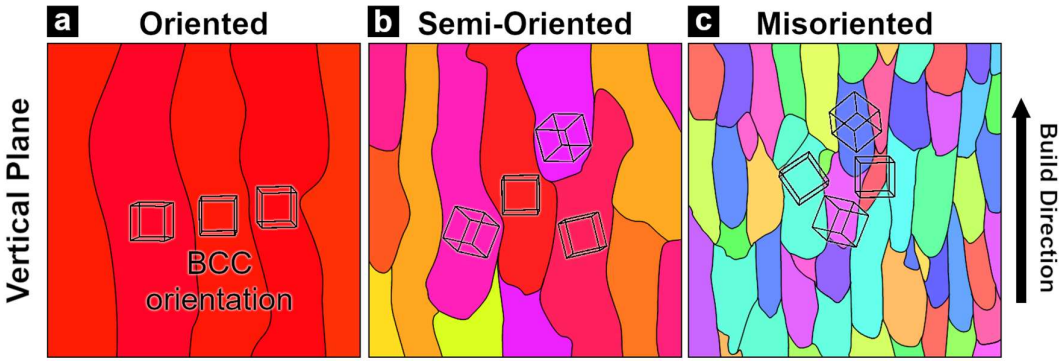

Figure 6.1: Schematic of three classifications of microstructures: a) oriented, b) semi-oriented, and c) misoriented.

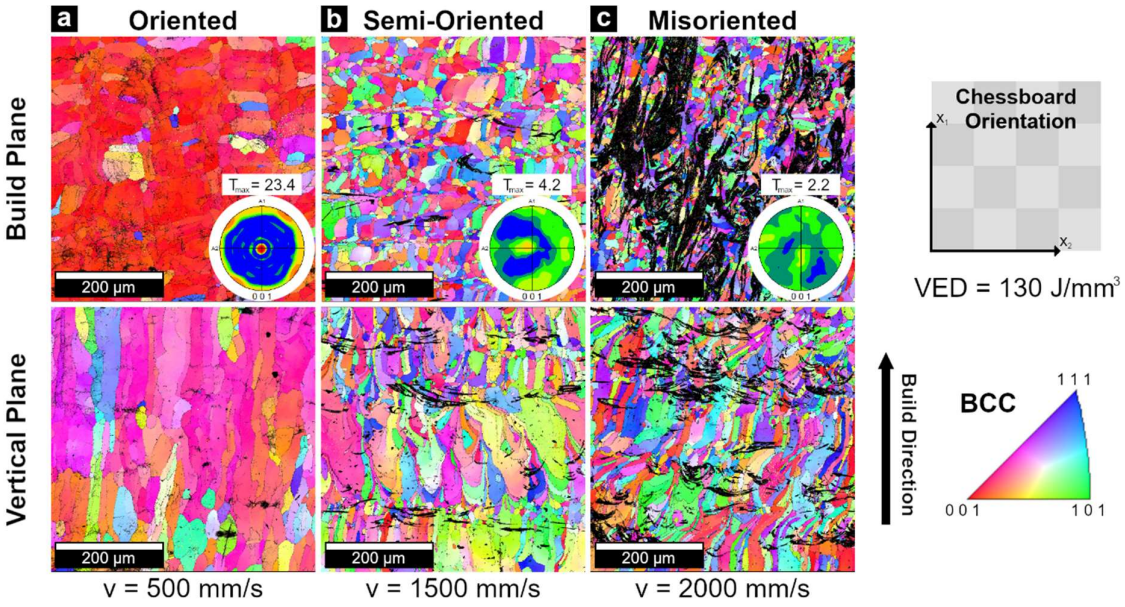

Figure 6.2: Representative EBSD of the three characteristic microstructures.

Table 6.1: Interstitial composition.

VED [J/mm3]	Scan speed [mm/s]	Texture T [MUD]	$I_{\text{rel}}^{\{200\}}$	Microstructure
50	800	2.145	0.38	Misoriented
50	2000	1.282	0.162	Misoriented
70	1500	1.687	0.304	Misoriented
90	500	4.951	0.946	Semi-oriented
90	800	6.480	1.360	Oriented
90	2000	1.709	0.389	Misoriented
90	2500	1.660	0.261	Misoriented
110	500	9.308	1.326	Oriented
110	1000	8.750	1.248	Oriented
110	1500	4.000	0.597	Semi-oriented
130	500	23.371	2.256	Oriented
130	1500	4.248	0.566	Semi-oriented
130	2500	2.214	0.328	Misoriented
150	500	30.715	2.748	Oriented
150	1000	15.151	1.348	Oriented
150	1500	2.076	0.267	Misoriented
150	2500	2.304	0.349	Misoriented

XRD results were found to correlate very well with the texture value from EBSD. As the oriented texture was {100} in the build direction, the relative intensity of the {200} XRD peak from scanning the build plane can be used to determine the microstructure (Fig. 6.3a). The relative intensity $I_{\mathrm{rel}}^{\{200\}}$ is defined as the absolute intensity of the {200} peak $I^{\{200\}}$ normalized by the average β-phase peak intensity $\bar{I}_{\beta}$[198]:

$$\boldsymbol{I_{\mathrm{rel}}^{\{200\}} = \frac{I^{\{200\}}}{\bar{I}_{\beta}}} \tag{6.1}$$

In some samples, such as the representative semi-oriented and misoriented patterns shown in Fig. 6.3a, α peaks are visible from the large fraction of α″ martensite. While it is difficult to deconvolute the overlapping $\{110\}_{\beta}$ and $\{002\}_{\alpha''}$ peaks, the crystallography of the β→α″ transition occurs such that all $\{002\}_{\alpha''}$ planes are transformed $\{110\}_{\beta}$ planes, so texture is effectively preserved[74]. The peaks from α″ martensite were determined not to have a significant effect on relative intensity. The value of $I_{\mathrm{rel}}^{\{200\}}$ was found to correlate directly with T (Fig. 6.3b). The semi-oriented data points fall between $I_{\mathrm{rel}}^{\{200\}}$ values of 0.5 and 1. The microstructure transition itself is not discrete and therefore cannot be strictly defined, however, these values can be used as approximate threshold values for the microstructure transition.

The $I_{\mathrm{rel}}^{\{200\}}$ value from all printed samples can be interpolated to create a continuous map of sample microstructure (Fig. 6.4a). Linearly interpreting $I_{\mathrm{rel}}^{\{200\}}$ over VED and scan speed creates a manifold of estimated $I_{\mathrm{rel}}^{\{200\}}$ values. Contours were then drawn on the manifold at the threshold $I_{\mathrm{rel}}^{\{200\}}$ values of 0.5 and 1 (Fig. 6.4b). These contours were then projected onto a single plane, sectioning the design space into three regions based on predicted microstructure (Fig. 6.4c). The resulting map shows two types of OMT. The thermal VED transition occurs between VEDs of 90 and 70 J/mm^3. The second transition is dependent on scan speed, or linear energy density (LED). While it consistently begins at a laser speed of approximately 1200 mm/s (LED = 0.133 J/mm), the microstructure becomes fully misoriented at different speeds

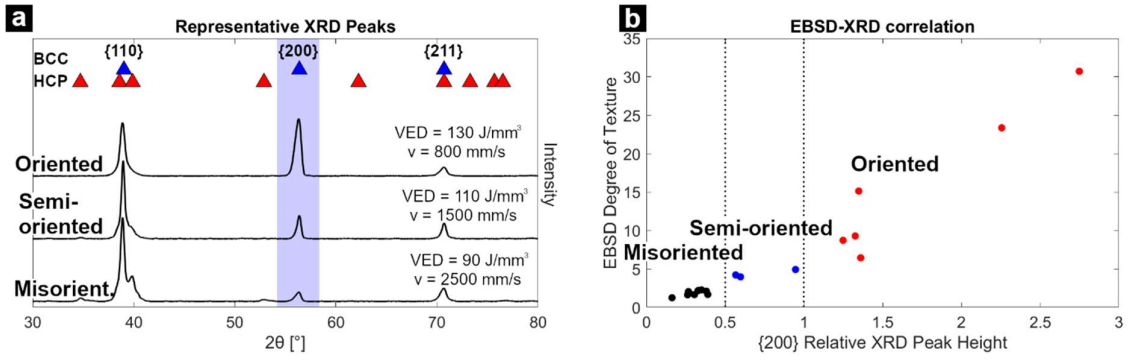

Figure 6.3: XRD peak definition and EBSD-XRD correlation.

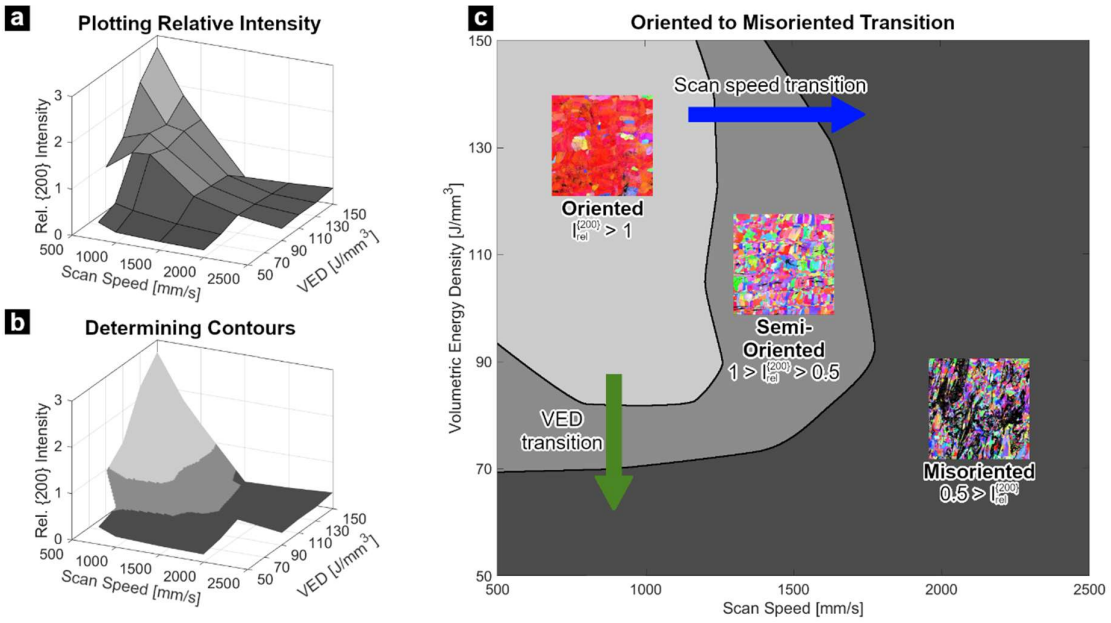

Figure 6.4: Development of an OMT map. a-b) Intermediate steps of map development. c) The OMT map.

depending on VED, ranging from 1400 mm/s (*LED* = 0.114 J/mm) at a VED of 150 J/mm^3 to 1700 mm/s (*LED* = 0.094 J/mm) at a VED of 90 J/mm^3.

6.2.2 Single-track Scans

To better understand how varying laser speed affects microstructure, in-situ single track "bead-on-plate" type experiments were performed using scan speeds of 500, 800, 1000, 1500, and 2000 mm/s. For each speed, two experiments were formed. In the "cold" case, single laser passes were run on a room temperature billet of Ti-10Mo produced by SPS. In the "in-situ" case, a block with a rectangular base of 5×10 mm and a height of 3 mm was printed using a VED of 130 J/mm^3. Single laser tracks spaced 2 mm apart were then immediately performed at the top of each block at the end of the L-PBF process (Fig. 6.5). These single laser tracks were angled at 45° to the chessboard pattern to increase contrast. Cross sections taken near the center of these weld tracks were polished then imaged by EBSD and EDS.

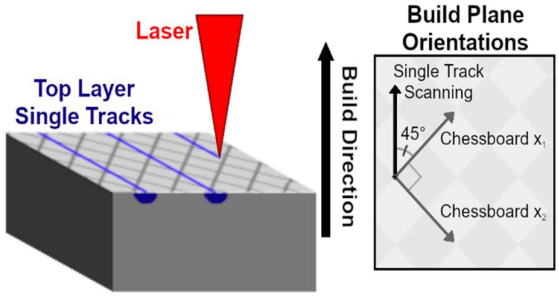

Figure 6.5: Schematic of the in-situ single-track experiment geometry.

Cross sections of the bead-on-plate experiments performed on the cold SPS billet showed high penetration and excellent homogenization. Combined IQ-IPF maps of the β-phase clearly show the profile of the melt pool through dark, low-IQ regions (Fig. 6.6). These low-IQ regions are full of α″ martensite and ω precipitates, as discussed in §6.2.1. The β-phase microstructure is still visible through the low-IQ regions and shows horizontal grain growth from border grains to a clear centerline across all conditions. Furthermore, a heat-affected zone (HAZ) is visible as a slightly darker area surrounding the main melt pool that has less of the white α-phase. The full dimensions including the surface width W_S, the width of the melt pool at 50% of the penetration depth W_{50}, and the width of the heat affected zone at 50% of the penetration depth W_{HAZ} are listed in Table 6.2. Notably, while W_{50} stays relatively constant around 60 µm across all scan speeds, the surface width and penetration depth decrease with increasing scan speed. This is most notable between 1000 mm/s and 1500mm/s, where the cross-section geometry switches from a keyhole profile to a conduction profile. EDS shows

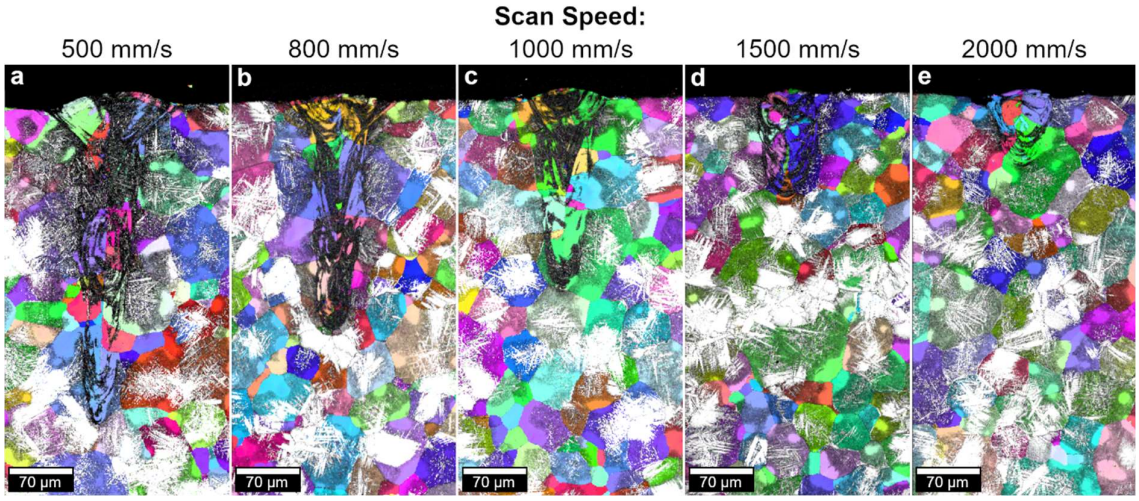

Figure 6.6: EBSD maps of weld pool cross sections on a cold SPS substrate. Contrast is IQ and IPF of the β-phase.

Table 6.2: Cold SPS single track dimensions.

Scan speed [mm/s]	W_S [µm]	W_{50} [µm]	W_{HAZ} [µm]	Penetration depth [µm]
500	153	60	137	357
800	116	61	125	257
1000	103	50	114	218
1500	67	66	91	125
2000	61	59	103	88

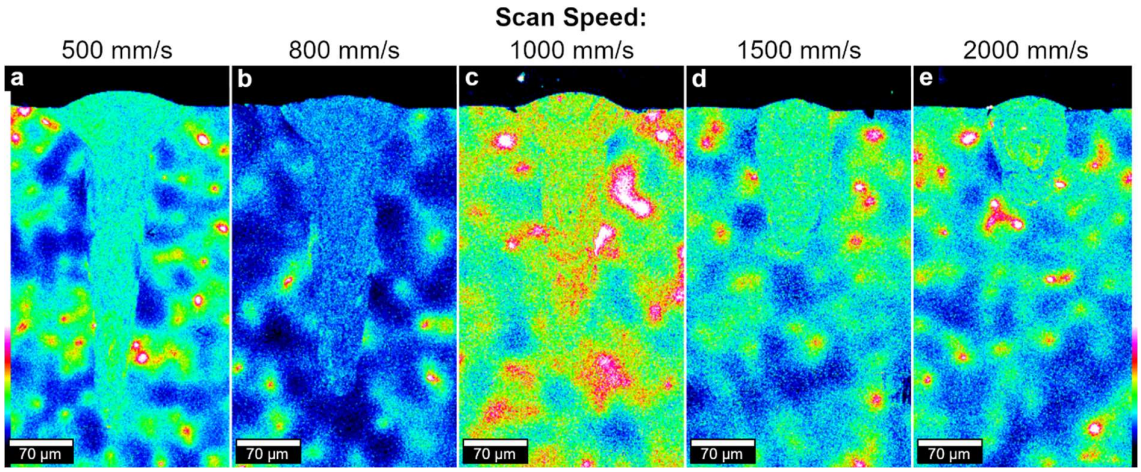

Figure 6.7: EDS maps of Mo concentration of weld pool cross sections on a cold SPS substrate.

excellent homogeneity across all scan speeds (Fig. 6.7). The molybdenum content in the melt pool is significantly more homogeneous than in the bulk.

The in-situ single-track laser passes were performed on blocks printed using the same scan speed and a VED of 130 J/mm^3. The melt pool width, overlap between adjacent tracks at a VED of 130 J/mm^3, and melt pool penetration from the estimated top of the powder layer are shown in Fig. 6.8 and listed in Table 6.3. The pure titanium powder has a nominal density of 50% fully dense and the layer thickness is 20 µm, so the powder layer height was estimated as 40 µm above the edge of the melt pool. While melt pool width decreases with increasing scan speed, the hatch spacing required to keep VED constant leads to an increase in overlap percentage. As before, the most notable feature is a change in weld pool morphology between

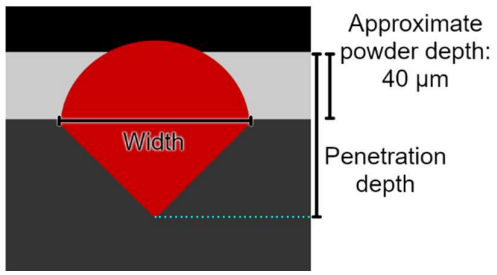

Figure 6.8: Diagram of measured melt pool dimensions.

Table 6.3: In-situ single track dimensions.

Scan speed [mm/s]	Width [µm]	Overlap [%]	Penetration [µm]
500	177	30	174
800	155	50	150
1000	137	55	139
1500	102	60	70
2000	81	62	57

1000 mm/s and 1500 mm/s. The penetration depth decreases drastically from 139 µm to 70 µm. This can again be attributed to the transition from a keyhole to a conduction type profile, as clearly seen in the cold case. The in-situ tracks were wider and shallower than the cold tracks of the same scan speed because of the 40 µm layer of powder on top. This layer densifies during melting, leading to greater lateral conduction of heat and wider tracks. Absorptivity also changes with powder addition, decreasing penetration depth.

EDS shows a significant decrease in Mo homogeneity with increasing scan speed (Fig. 6.9). The decrease in homogeneity is attributed to poor mixing in the liquid phase due to small, fast melt pools. No inhomogeneity due to solute trapping could be observed at this length scale. At faster scan speeds, incompletely melted Mo particles can be observed (Fig. 6.9d). The density of these particles increases steadily between 500 mm/s and 2000 mm/s, indicating less melting and homogenization. These particles can serve as randomly oriented nucleation sites for β-phase grains but occur at low enough density that they are unlikely to be the main driving factor of the OMT.

The solidification behavior of the melt pool can be seen by EBSD imaging (Fig. 6.10). Much of the weld pool is obscured by the precipitate-rich black regions. From the swirling patterns of these regions shown in Fig. 6.2 and Fig. 6.6, it can be concluded that they are artifacts of melt pool flow during solidification. These show the melt pool boundary of the single-track scan as well as prior melt pool boundaries in the bulk. The boundaries are confirmed by the BSE/EDS images. The single-track melt pools show two regions: an epitaxial growth zone at the base, and an equiaxed grain zone at the top[129].

Grains in the epitaxial growth region have a high vertical aspect ratio and are shown to be continuous with the unmelted grains bordering the melt pool. These boundary grains can serve as initiation sites for solidification and extend coherently into the melt pool during solidification. At faster scan speeds, some of the high aspect ratio grains in this region do not share their orientation with any bordering grains because the nucleation rate is fast enough to compete with purely epitaxial growth. Additionally, the width of epitaxial grains decreases at faster scan speeds, likely due to the solute trapping effect and increased nucleation.

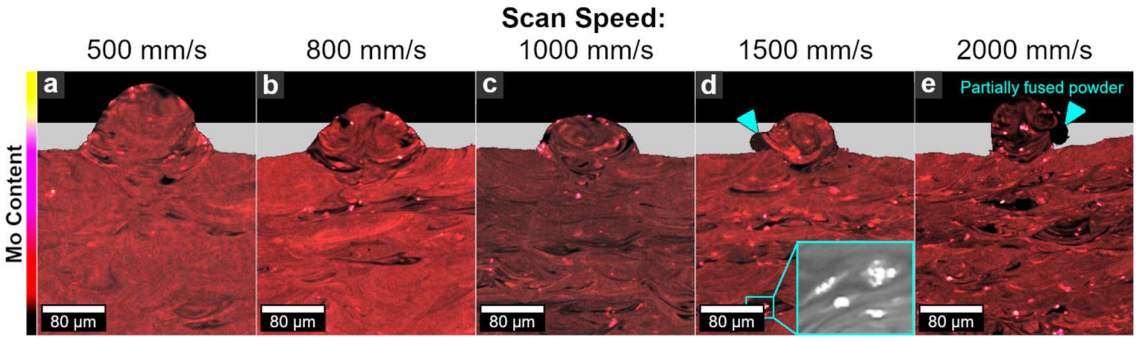

Figure 6.9: EDS maps of Mo concentration of weld pool cross sections from the in-situ single-tracks.

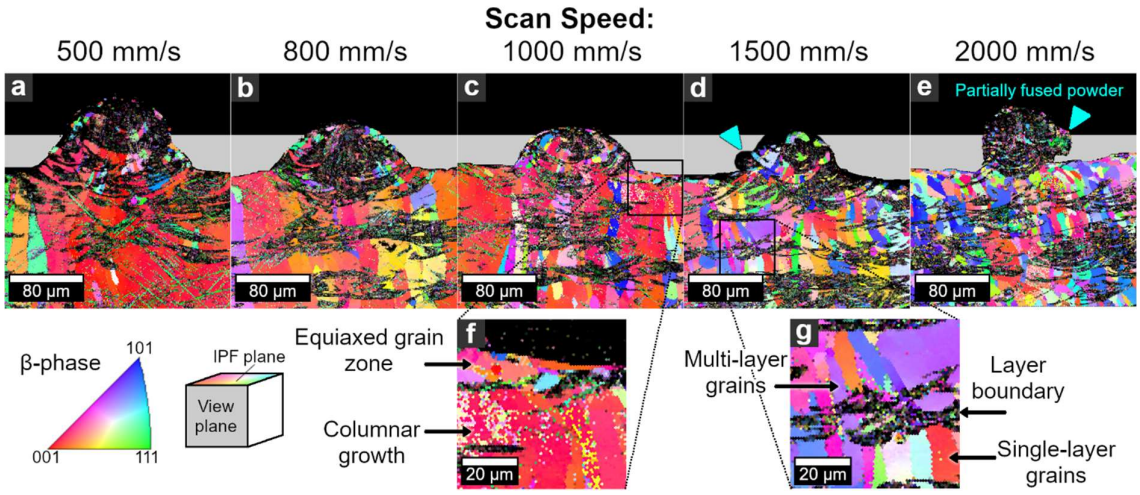

Figure 6.10: EBSD maps of weld pool cross sections from the in-situ single-tracks. Contrast is IQ and build plane IPF.

The tops of the melt pools have small, randomly oriented grains, indicating an equiaxed grain zone[132]. Epitaxial solidification occurs vertically upwards, so the top of the melt solidifies last. This allows for a greater degree of undercooling of the melt at the top, which increases the nucleation rate of new grains. When the nucleation rate exceeds a critical value, new nuclei outcompete epitaxial grain growth, and a CET occurs[126]. The equiaxed region increases in size with increasing scan speed due to a faster interface velocity promoting the CET[127].The equiaxed region of the top bulk layer is visible as small, randomly oriented grains that can be observed at scan speeds of 1000 mm/s to 2000 mm/s (Fig. 6.10f).

The orientation of grains in the epitaxial growth region and the bulk are governed by penetration depth. In the cases with deep keyhole profiles, the equiaxed layer is either small or nonexistent. Therefore, any equiaxed grains are fully remelted during the printing of every subsequent layer. The melt pool border is entirely composed of epitaxially grown grains of the previous layer. This allows for the coherent vertical extension of grains across multiple print layers, leading to a columnar, oriented microstructure. At the fast scan speed of 2000 mm/s, the penetration depth is small, and the equiaxed region is large. This leads to randomly oriented melt pool border grains, which in turn yields a misoriented epitaxial growth region. In the bulk, this can be seen to yield grains with heights of 20 µm, or one layer of thickness. In the 1500 mm/s case, the penetration depth is on the order of two layers, indicating that both epitaxially grown and equiaxed grains will border the melt pool, and the epitaxial region will have a weak orientation. This mixed-mode behavior creates the semi-oriented microstructure with grain heights ranging from 1-5 print layers (Fig. 6.10g).

6.3 Ti-10Mo Mechanical Properties and Mechanisms

6.3.1 As-Printed Microstructures of the Three Textures

While the texture of the as-printed microstructures has been well documented, further characterization must be done to fully understand their mechanical behavior. To compare mechanical properties, VED was held constant in order to keep the in-situ thermal history as consistent as possible. A high VED of 130 J/mm^3 was used to improve the homogeneity of Mo across all samples. The varied print parameters are listed in Table 6.4.

All three microstructures show large β grains on the order of 10-100 μm under EBSD, not counting the low image quality regions that were unable to be reliably indexed by EBSD

Table 6.4: Print parameters.

Scan speed [mm/s]	Hatch width [μm]	Expected texture
500	123	Oriented
1500	41	Semi-oriented
2000	31	Misoriented

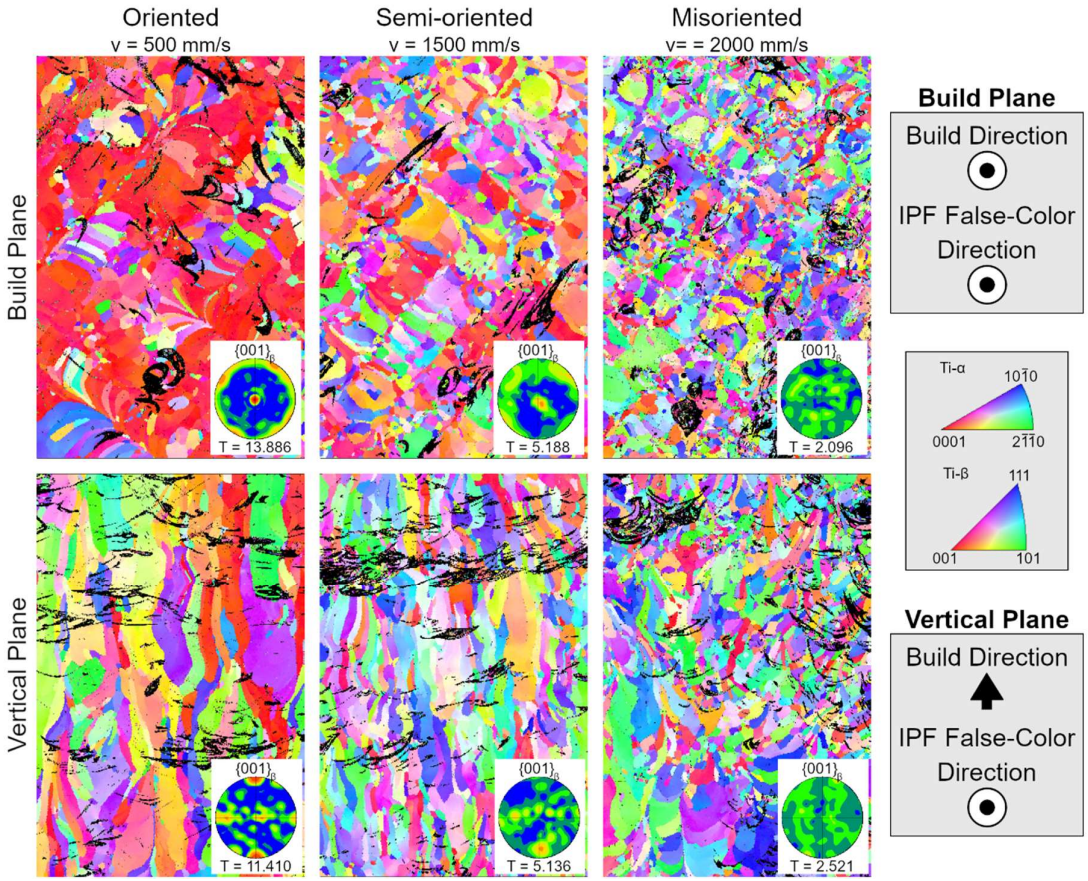

Figure 6.11: EBSD of the three microstructures achieved in this study with a pole figure of the {001} planes inlayed to show texture. Combined IQ-IPF maps are used to show the low IQ regions in black. a-c) Build plane cross-section, d-f) vertical plane cross section.

(Fig. 6.11). Again, the oriented microstructure showed a strong $\{001\}_\beta$ texture in the build direction, as well as a weak $\{001\}_\beta$ texture in the scan directions. The grains were columnar with a high aspect ratio, so to quantify grain size, the average diameter of a build plane cross section as well as the build direction height were measured. The oriented grains had an average build plane diameter of 38 μm and an average height of 68 μm. The semi-oriented microstructure showed a weak $\{001\}_\beta$ texture in the build direction and no significant scan direction texture. The grains were still columnar, although slightly smaller than the grains in the oriented microstructure. The semi-oriented grains had an average build plane diameter of 27 μm and an average height of 40 μm. As expected, the misoriented microstructure had no discernable texture. It also had the smallest and most equiaxed grains, with an average build plane diameter of 17 μm and an average height of 25 μm.

The nature of the low IQ EBSD regions was revealed by TEM (Fig. 6.12). While EBSD showed all three microstructures as being entirely β-phase, TEM of the as-printed oriented microstructure showed a high density of nanoprecipitates of other phases. Ti-10Mo is prone to the precipitation of both α″-phase martensite and ω-phase at elevated temperatures[74,110]. Both these phases are observed by TEM. SAD of the β-phase showed a diffraction pattern consistent with ω-phase precipitation (Fig. 6.12c). Dark field imaging using the ω-phase peaks shows it occurs as nanoprecipitates on the order of a few nanometers. The α″-phase martensite was identifiable by the SAD pattern. The pattern is identifiable as α″-phase rather than α-phase because the [001] peak is not completely forbidden by destructive interference, despite a low intensity. The α″-phase martensite occurs as high aspect ratio laths with sizes on the order of 100 nm to 1 μm (Fig. 6.12d). The morphology of the ω and α″ nanoprecipitates is consistent with reported microstructures[199].

The semi-oriented and misoriented samples can also be assumed to have α″-phase martensite and ω-phase precipitates. The laser scan speed varied between each of the three print conditions, affecting the melt pool solidification behavior and texture. However, volumetric energy density and layer thickness were kept constant across all three print conditions. Therefore, the heat flow was kept relatively constant and the thermal history of each point after the initial solidification should not have changed significantly between print conditions. Because the thermal conditions for precipitation of α″-phase martensite and ω-phase were met in the oriented sample, they should also have been met in the semi-oriented and misoriented samples. The presence of α″-phase martensite and ω-phase in all cases is further evidenced by the consistent presence of low IQ regions across the EBSD of all three samples.

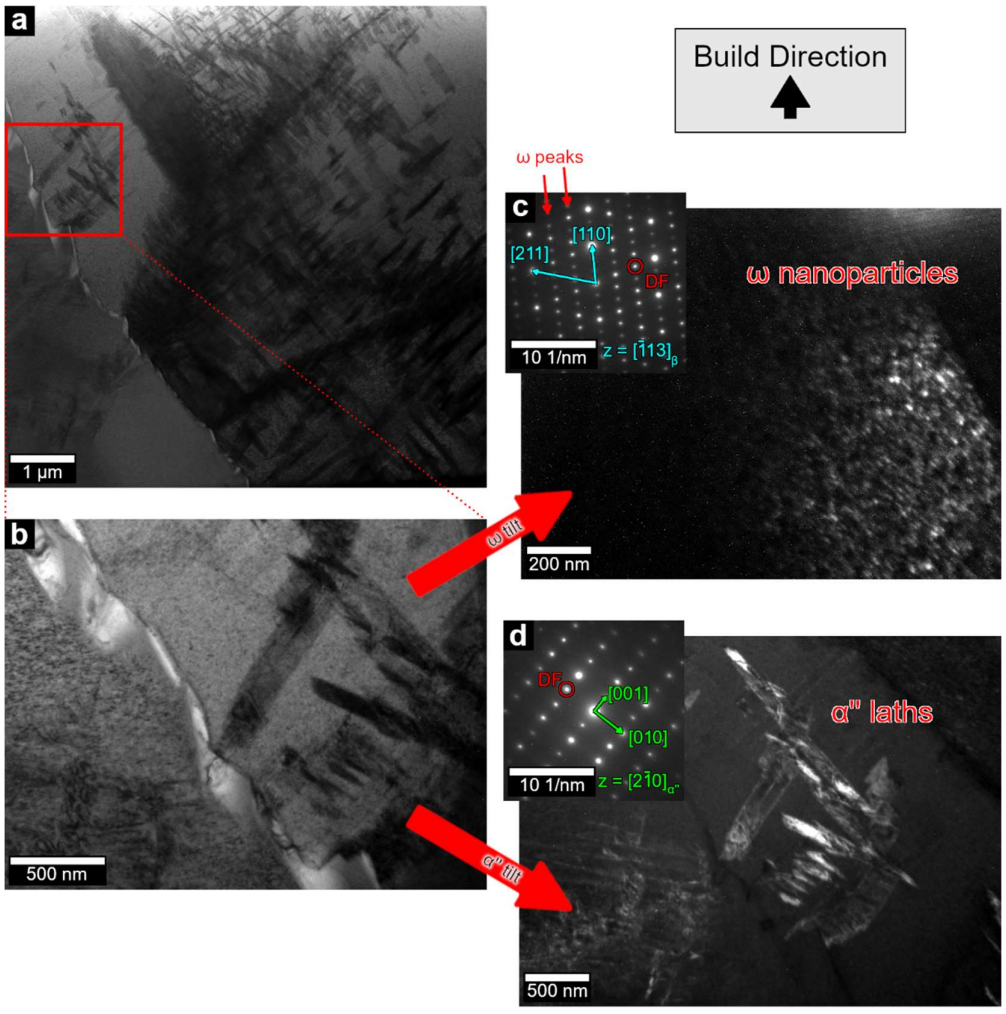

Figure 6.12: TEM of the as-printed oriented microstructure. a) STEM at 20kx magnification, b) STEM at 40kx magnification, c) dark field imaging showing ω-phase nanoparticles, d) dark field imaging showing α'' laths.

6.3.2 Heat Treatment Optimization of the Oriented Microstructure

Samples of the oriented condition were heat treated under the set of heat treatments listed in Table 6.5. The last condition (HT2X) was duplex aged, first treated for 8 h at 500°C, then furnace cooled to room temperature, then treated again for 3 h at 700°C. Tensile testing was performed on the as-printed material as well as all heat treatment conditions.

The heat treatments can be divided into three categories based on their mechanical performance (Fig. 6.13). The ultra-brittle category included the as-printed (AP) condition as well as HT500-1. This category is characterized by samples that fractured at the shoulders of the tensile dogbones rather than on the gauge, leading to poor and unreliable measured properties. The brittle category included HT900-0.5, HT900-2, and HT500-8. These conditions had high yield strengths above 1100 MPa, but negligible ductility. Only two conditions, HT700-3 and HT2X, showed any plasticity, making them the ductile category. HT2X and HT700-3 had similar yield strengths of 828 ± 11 MPa and 837 ± 11 MPa respectively. HT2X

Table 6.5: Heat treatment conditions.

Name	Holding temperature [°C]	Holding time [h]	Cooling method	Approx. cooling rate [°C/s]
HT500-1	500	1	Furnace Cool	0.1
HT500-8	500	8	Furnace Cool	0.1
HT700-3	700	3	Furnace Cool	0.1
HT900-0.5	900	0.5	Air Quench	10
HT900-2	900	2	Air Quench	10
HT2X	500, 700	8, 3	Furnace Cool	0.1

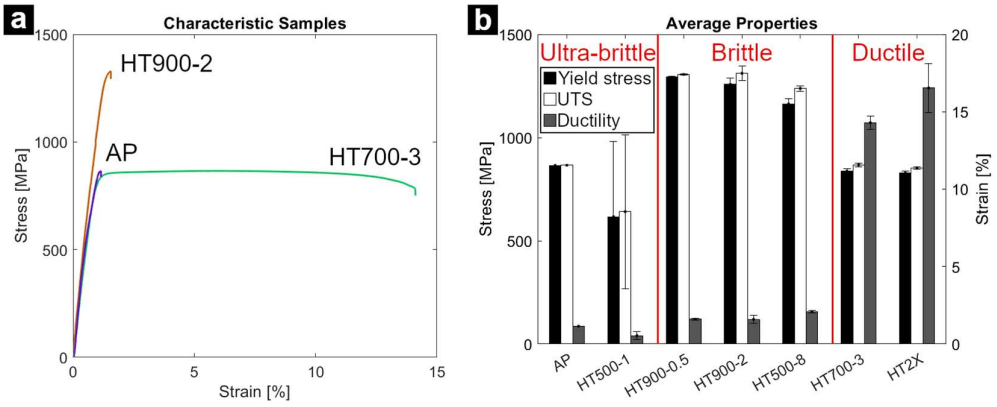

Figure 6.13: Mechanical properties of the oriented microstructure after various heat treatments. a) Characteristic stress-strain curves, b) average mechanical properties.

showed a slightly higher average ductility of 16.5 ± 1.6% compared to 14.3 ± 0.4% in HT700-3. This improvement to ductility was considered marginal for the additional 8 hours of heat treatment, so HT700-3 was selected as the heat treatment for further comparison of all three microstructures.

To understand why the solution treated samples showed such low ductility, HT900-2 was examined by EBSD and TEM. EBSD shows a microstructure similar to the as-printed microstructure, although with slightly larger and more rounded grains due to grain growth (Fig. 6.14)[200]. While the whole image showed a lower average IQ, the localized low-IQ regions were dissipated by this heat treatment. TEM shows that the uniformly reduced IQ is from a high density of α″-phase martensite laths (Fig. 6.15a) and an almost complete saturation of the β matrix with ω-phase precipitates (Fig. 6.15b). The brittle mechanical performance is concluded to be from the high density of ω-phase precipitates[76].

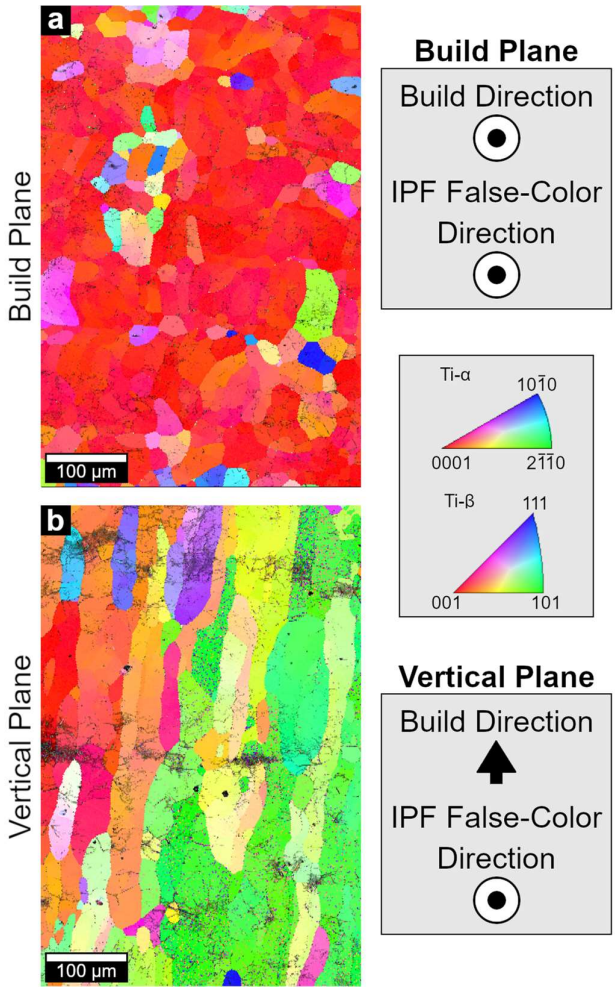

Figure 6.14: The EBSD microstructure of condition HT900-2. IQ-IPF of the a) build and b) vertical planes.

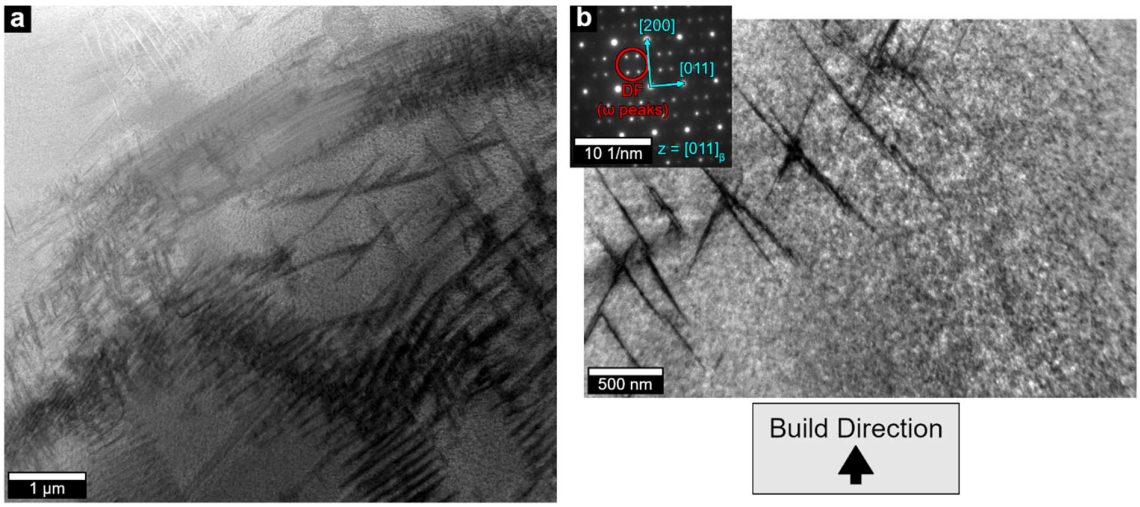

Figure 6.15: TEM of condition HT900-2. a) 20,000x magnification STEM showing precipitated α'' lathes. b) Dark field showing a high density of ω-phase nanoprecipitates.

TEM of the HT700-3 condition shows it to have a duplex α-β microstructure (Fig. 6.16). STEM shows a β-phase matrix (dark), with a single large, vertical α grain as well as several diagonal α grains. The vertical grain is grain boundary nucleated α-phase (α_{GB}), while the diagonal α grains occur at angles consistent with martensite, suggesting they grow from the α″ precipitates[57]. These martensite-nucleated α grains (α_M) have a high aspect ratio with a constant width of around 200 nm.

TEM-EDS shows strong Mo segregation into the β phase (Fig. 6.16d-g). Mo content is 22% in the β-phase matrix and less than 1% in both grain boundary and matrix α-phase. At 700°C, the equilibrium Mo content is 17.8% in the β-phase and 0.8% in the α-phase (Fig. 6.17). The measured Mo content in the β-phase is higher than the 700°C equilibrium concentration because the equilibrium concentration increases during furnace cooling. No significant accumulation or depletion of Mo near the grain interfaces was observed. The high Mo content of the β-phase has a stabilizing effect, suppressing the formation of α″-phase martensite and ω-phase precipitates during cooling. SAD of the β-phase matrix shows ω-phase peaks, but they are significantly weaker in intensity than the as-printed or HT900-2 cases (Fig. 6.16c).

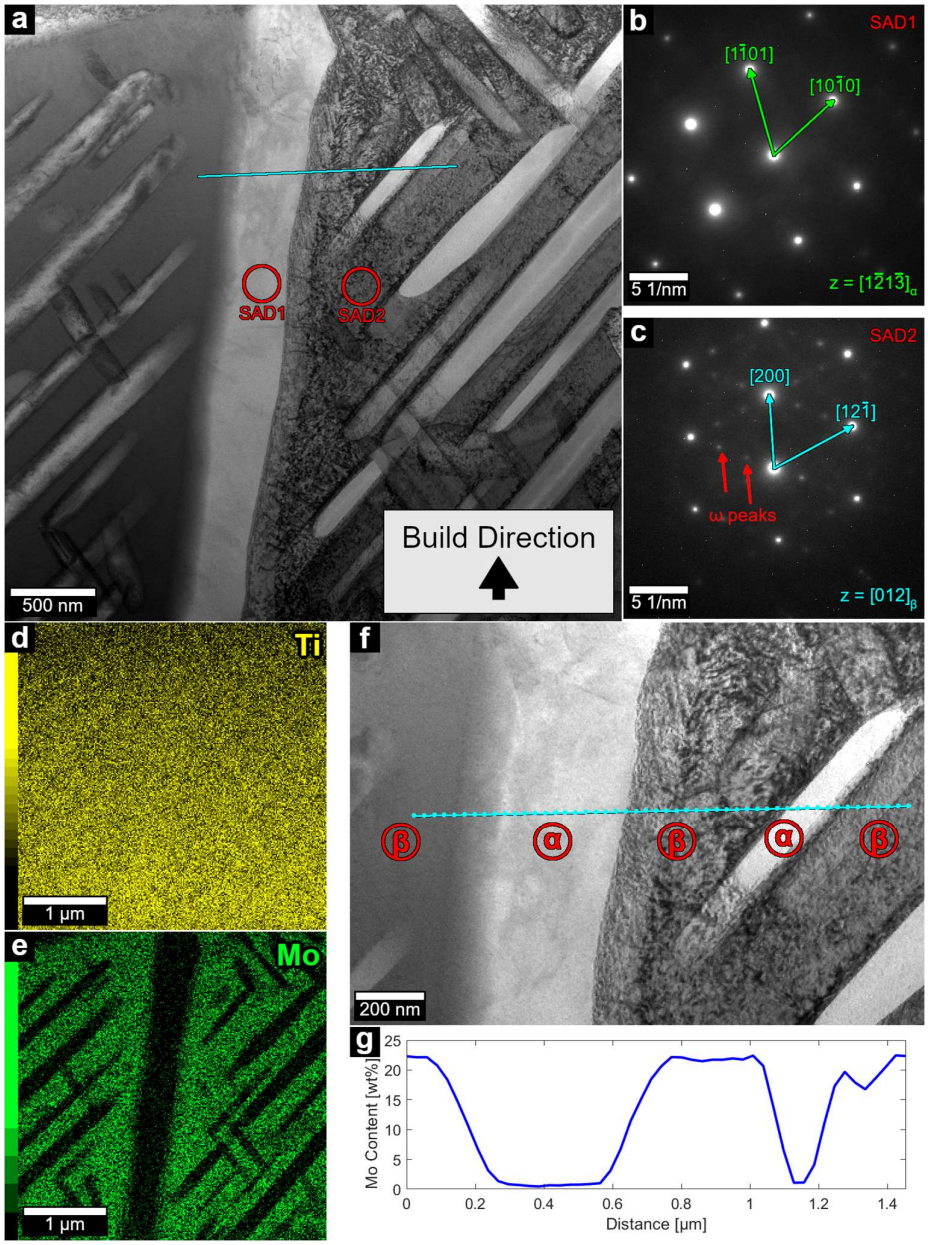

Figure 6.16: The microstructure of the oriented microstructure heat treated for 3 h at 700°C. a) STEM at 40kx magnification. SAD of b) grain boundary α-phase and c) β phase. EDS imaging of d) the Ti-K peak and e) Mo-L peak. EDS line scan f) STEM location, g) Mo content.

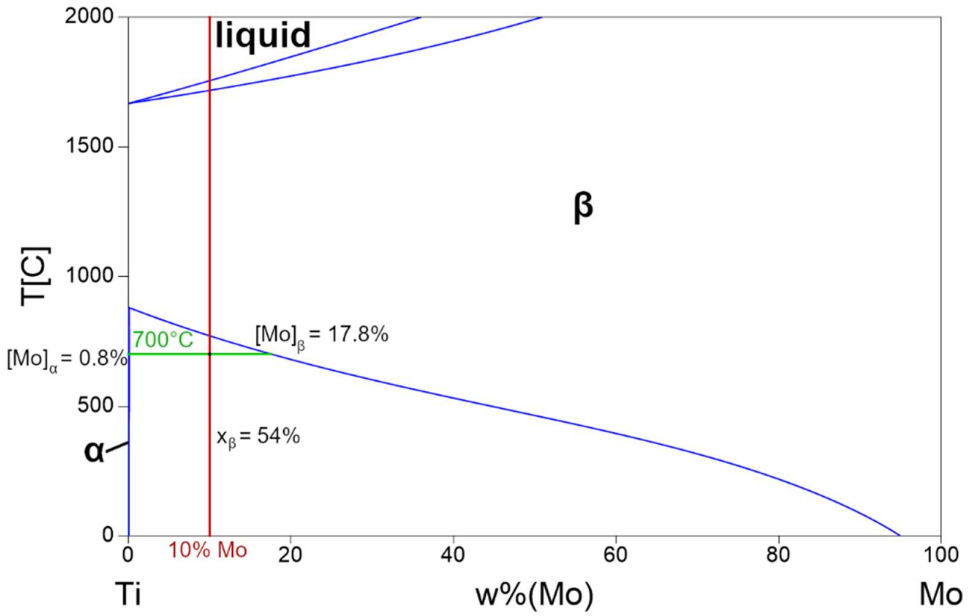

Figure 6.17: Calculated phase diagram of the Ti-Mo binary system showing the equilibrium state of Ti-10Mo at 700°C.

While α″-phase martensite formation was suppressed in the high Mo content β-phase, lower Mo content regions showed evidence of α″-phase formation (Fig. 6.18). The α″-phase takes the form of vertical bands, which are marked with arrows. These vertically banded regions coincide with areas of lower Mo content (Fig. 6.18b). SAD of these banded regions identifies them as α″ martensite due to the presence of {001} peaks (Fig. 6.18c). The dark bands, shown clearly in Fig. 6.18d, have lengths on the order of 100 nm and extremely narrow widths on the order of 1 nm.

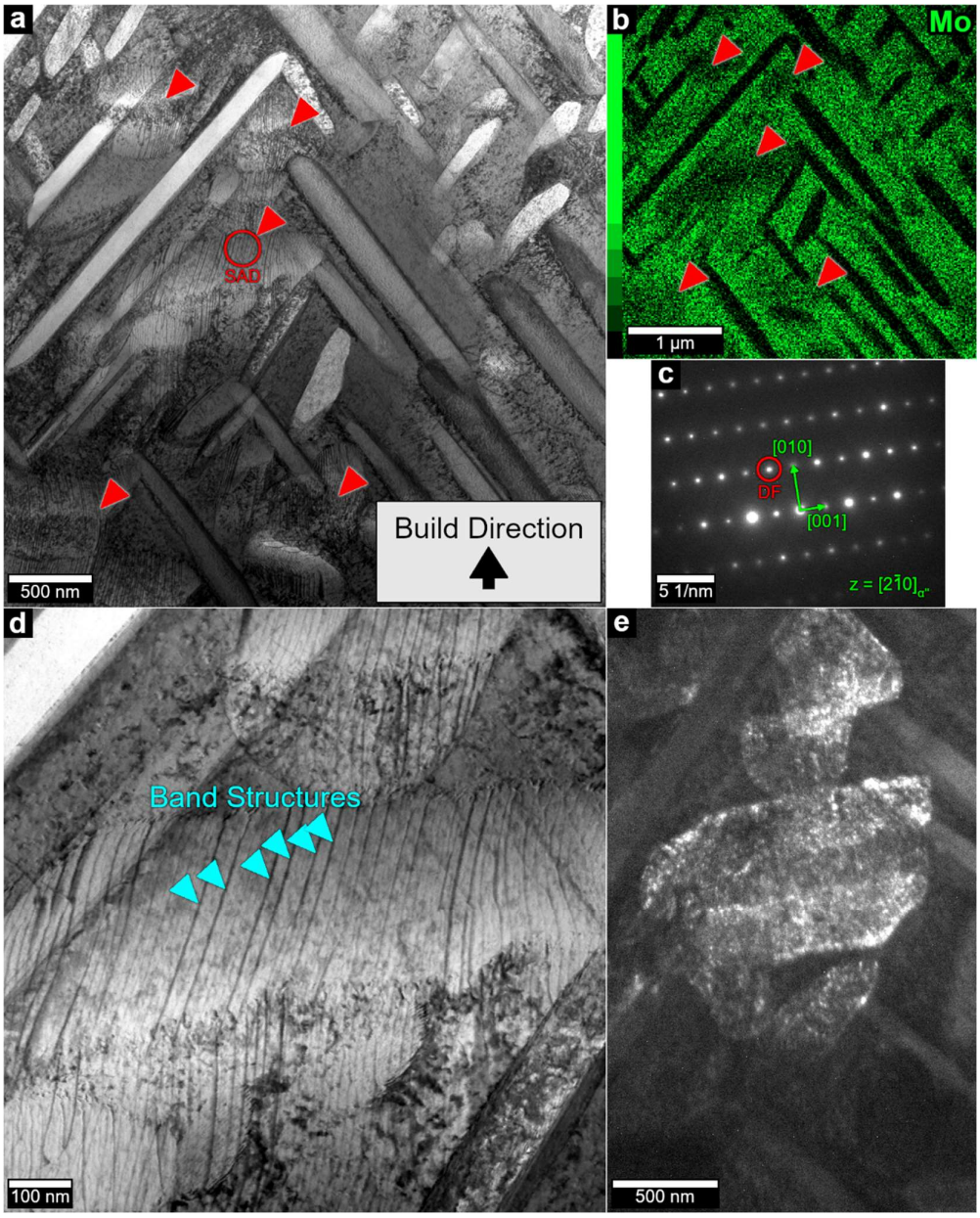

Figure 6.18: Banded regions of the oriented microstructure heat treated for 3 h at 700°C. a) STEM at x40k magnification with red arrows pointing out banding regions, b) EDS frequency of the Mo-L peak. Closer inspection of the banded region was done using c) SAD, d) high-magnification STEM, and e) dark field imaging.

6.3.3 Heat Treated Microstructures with Three Textures

The HT700-3 heat treatment (3 h at 700°C then furnace cooled) was applied to all three microstructures. Texture analysis of a 400 µm by 600 µm region shows how heat treatment affects the as-printed texture (Fig. 6.19a-c). The texture of the β-phase after heat treatment is identical to the as-printed β-phase texture. The oriented microstructure shows that $\{110\}_\beta$ and

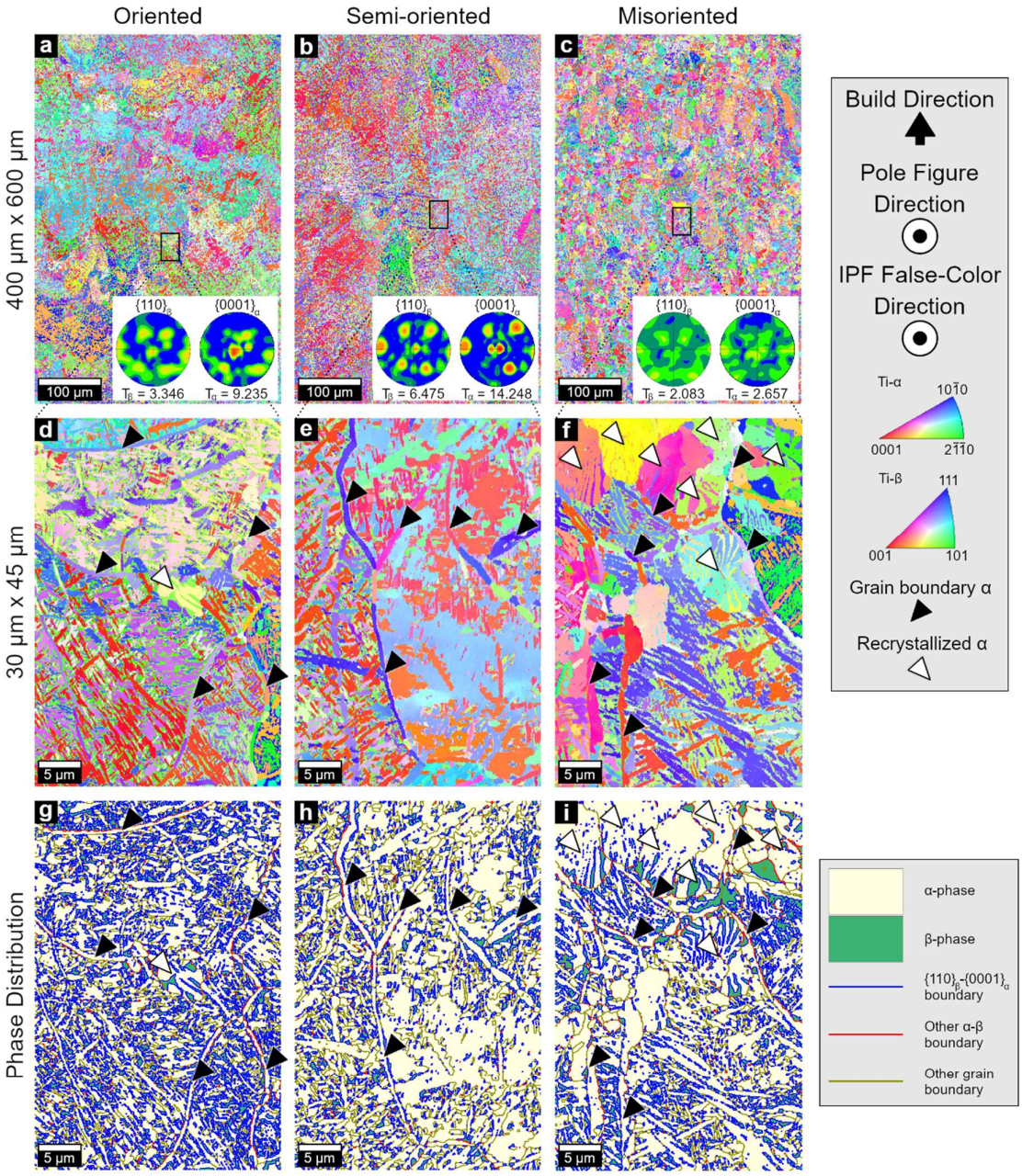

Figure 6.19: EBSD of all three microstructures heat treated for 3 h at 700°C. a-c) Large IPF maps showing both α and β textures in the pole-figure inlays, d-f) fine IPF maps showing the microstructure, with grain boundary α labeled with a black arrow, g-i) phase distribution of α and β phases, with $\{110\}_\beta$-$\{0001\}_\alpha$ interfaces highlighted in red.

$\{0001\}_\alpha$ planes align during the $\beta \rightarrow \alpha$ transition (Fig. 6.19a). However, the transition is not equal across $\{110\}_\beta$ planes. The $\{0001\}_\alpha$ texture shows a strong texture that is perpendicular to the build direction. The anisotropy of the transition can be attributed to high aspect ratio parent-β grains as well as residual stress relief favoring transitions along the build plane.

In the semi-oriented and misoriented cases, the preference for $\{0001\}_\alpha$ facets in the build plane continues, although more weakly (Fig. 6.19b-c). In the semi-oriented case, the pole figures for $\{110\}_\beta$ and $\{0001\}_\alpha$ show peaks in the same locations, but the $\{0001\}_\alpha$ peaks in horizontal directions are stronger than those out-of-plane. In the misoriented case, there is no distinct $\{110\}_\beta$ texture. However, there is still a weak trend towards $\{0001\}_\alpha$ in the horizontal build plane and a clear lack of $\{0001\}_\alpha$ facets in the build direction.

Higher resolution imaging shows three distinct classes of α-phase grains (Fig. 6.19d-f). Due to the fine nature of the microstructure, EBSD does not show the β matrix clearly (Fig. 6.19g-i). However, the nature of the α-phase grains is distinguishable through their morphology and location. The previously identified α_{GB} is marked with black arrows. The α_G grains have a high aspect ratio and a curved shape that follows the interface between two parent-β grains. Recrystallized α (α_{RX}) is marked with white arrows and has a pearlite-type microstructure with interspaced β-phase. The remaining α-phase is α_M, which occurs at sets of parallel lamellae within the matrix of single parent-β grain.

The texture of the parent-β grains is well preserved by the α-phase because most α grains are aligned with an adjacent β grain through a $\{110\}_\beta$-$\{0001\}_\alpha$ interface. The α_M grains show exclusively $\{110\}_\beta$-$\{0001\}_\alpha$ interfaces, which is consistent with martensite formation within a single parent-β grain[31]. The α_{GB} grains consistently show only partial $\{110\}_\beta$-$\{0001\}_\alpha$ interfaces due to bordering multiple β grains with different orientations (Fig. 6.19g-i). The orientation mismatch is particularly strong in the misoriented case, where adjacent parent-β grains have completely independent orientations. However, the α_{GB} grains always have at least one $\{110\}_\beta$-$\{0001\}_\alpha$ interface, indicating they still preserve texture. The recrystallized α_{RX} regions show no evidence of preserving the as-printed texture, decreasing in the texture of the heat-treated material. Although the density of α_{RX} was unable to be reliably quantified by EBSD, the α_{RX} appears to occur with higher frequency in the misoriented phase, where the texture is already low. It was concluded that the quantity of α_{RX} is insufficient to affect overall texture trends.

6.3.4 Mechanical Testing of Three Textures

Mechanical testing was performed in tension in the transverse direction as well as in compression in both the transverse and build directions (Fig. 6.20a). For compression testing, cubes with an edge length of approximately 4.5-5 mm were cut from each sample. Sample

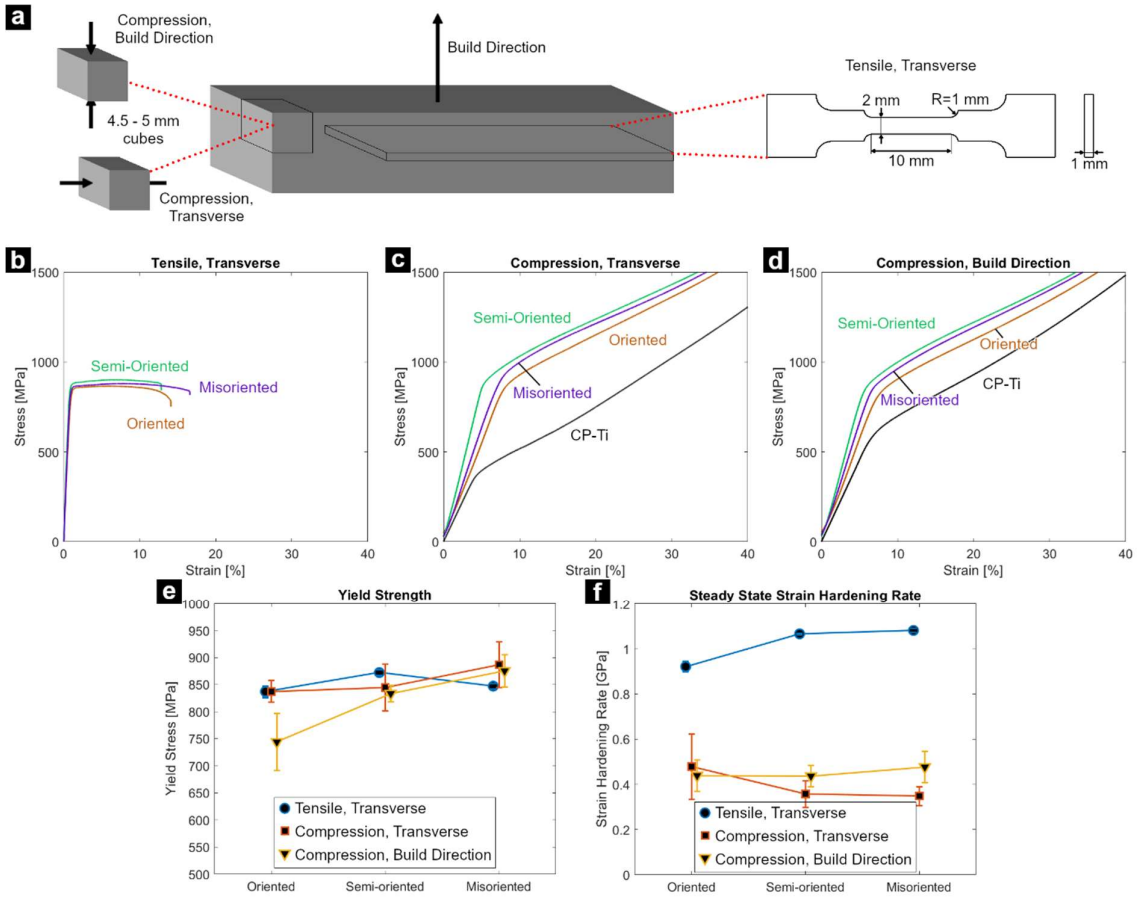

Figure 6.20: Mechanical performance of all microstructures heat treated for 3 h at 700°C. a) Sampling geometries, b-d) stress-strain curves, e-f) average mechanical properties.

dimensions were confirmed by micrometer before testing Compression tests were also performed on L-PBF CP-Ti heat treated for 3 h at 700°C as a reference comparison.

Tensile testing in the transverse direction showed that strength and ductility do not vary linearly with texture (Fig. 6.20b). Results are summarized in Table 6.6. The yield stress and ultimate tensile stress (UTS) had average values within 1 standard deviation of error for the oriented and misoriented samples, but higher for the semi-oriented sample. Ductility decreased between the oriented and semi-oriented samples but increased to a maximum of 16.5% with the misoriented samples. For comparison, cast Ti - 7.5wt.% Mo heat treated to an equivalent microstructure is reported to have a tensile yield strength of 700 to 750 MPa and a ductility of

Table 6.6: Tensile properties.

Orientation	Yield stress [MPa]	UTS [MPa]	Ductility [%]
Oriented	837 ± 11	867 ± 9	14.3 ± 0.4
Semi-oriented	872 ± 6	902 ± 4	12.7 ± 0.5
Misoriented	847 ± 5	858 ± 3	16.5 ± 0.8

20%[201]. L-PBF Ti-10Mo shows higher strength but reduced ductility compared to the cast equivalent.

Compressive testing showed an unusually low slope in the elastic region (Fig. 6.20c-d). In compressive testing, strain could not be verified by DIC. Strain was taken as the machine stroke relative to the measured sample height. The Ti-10Mo samples showed extremely low effective Young's moduli of 10-15 GPa, and the reference CP-Ti samples had an effective Young's modulus of 10 GPa. These values are non-physical and likely the result of additional machine elasticity that was unaccounted for.

The strain hardening rate was calculated as the local derivative of true stress with respect to true strain. The steady state strain hardening rate (SSSHR) was taken as the average strain hardening rate between 3% and 9% true strain for tensile samples, and 15% and 30% true strain for compressive samples. The SSSHR of the compressive samples was unusually low due to the strain measurement technique, but this does not affect the relative values of the SSSHR because all samples were the same size[202].

Unusually, the SSSHR decreases in isotropy with decreasing texture (Fig. 6.20f). In the oriented microstructure, the SSSHR was similar in both directions. With decreasing texture, the compressive SSSHR decreased in the transverse direction and increased slightly in the build direction. The anisotropy of compressive SSSHR in the misoriented case can be explained by the texture of the α-phase. Across all three microstructures, the α-phase has a $\{0001\}_\alpha$ texture in the transverse direction. The α-phase texture leads to an anisotropic component of work hardening in which the compressive SSSHR is higher in the build direction than the transverse direction. In the misoriented sample, α-phase texture is the primary source of microstructural anisotropy. The isotropy of SSSHR in the oriented case cannot yet be explained and will be discussed in the next section.

6.3.5 Deformation Mechanics

TEM of an oriented sample from near the fracture surface shows the active deformation mechanisms (Fig. 6.21). The duplex α-β microstructure is still visible, but the α_M laths have experienced moderate plastic deformation. Closer inspection shows a pileup of defects such as dislocations and nanovoids in the β matrix at α-β interfaces (Fig. 6.21b). The location of pileups in the β-phase indicates that under tension, the bulk of plastic deformation as well as void initiation occurs in the softer β phase.

The localization of deformation in the β-phase is consistent with yield stress performance. The yield stress and yield stress isotropy increased with decreasing texture, which correlates strongly with the β-phase microstructure (Fig. 6.20e). The increase in yield stress can be attributed to the decreasing size of parent-β grains over the OMT, and the increase in yield stress isotropy can be attributed to the misorientation of β grains. The β-phase governance

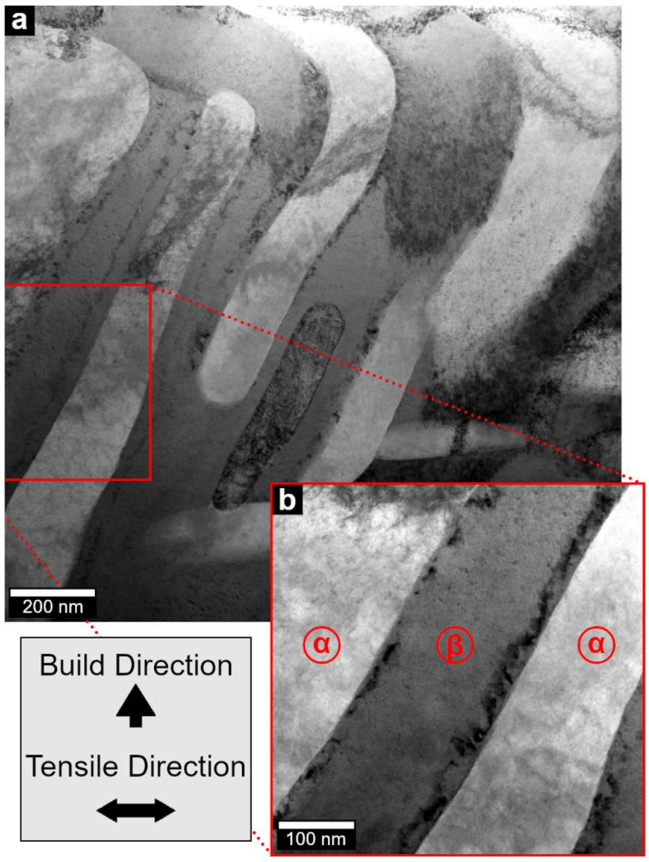

Figure 6.21: TEM of the oriented sample near the tensile fracture surface.

of yield stress is because the β-phase is softer than the α-phase and therefore yields preferentially. Preferential yielding of the β-phase is supported by the deformed structure seen in Fig. 6.21, with defect accumulation in the β-phase near the α interfaces.

By performing EBSD analysis at different stages of the tensile deformation process, further effects of texture on deformation mechanisms can be determined. EBSD was performed on tensile sample after fracture on the build plane in three locations: the undeformed region outside the shoulders, the uniform deformation region of the gauge 1.5 to 2 mm from the fracture surface, and in the necking region at the fracture surface (Fig. 6.22).

Dislocation motion behavior was summarized by plotting the Schmid factor (SF) of each major slip system. For the α-phase, the basal $\{0001\}$, prismatic $\{10\bar{1}0\}$, and first order pyramidal $\{10\bar{1}1\}$ slip systems of *a*-type ($\mathbf{b}=\langle 11\bar{2}\,0\rangle$) dislocations were considered[36]. For the β-phase, only the cubic close packed $\{110\}$ slip system for $\langle 1\bar{1}1\rangle$ dislocations is shown. For each slip system, the fraction of points in the respective phase with a Schmid factor of at least 0.45 was calculated and plotted in Fig. 6.22.

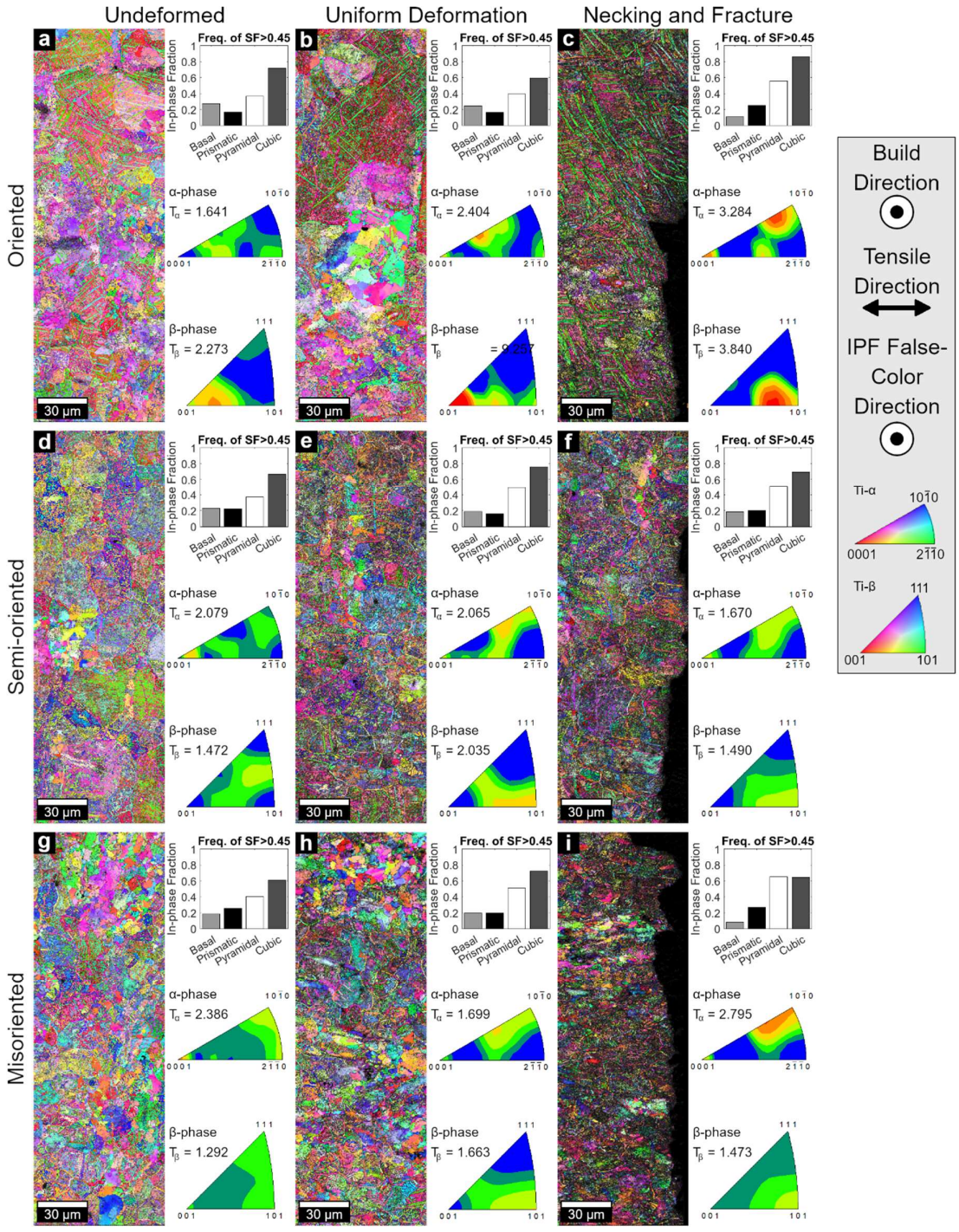

Figure 6.22: EBSD of the build plane of tensile samples using a combined IQ-IPF contrast. Fraction of high Schmid factor points and IPF texture plots in the tensile direction are shown alongside each image.

For all three initial microstructures, the fraction of points with a high pyramidal Schmid factor increases significantly with increasing deformation (Fig. 6.23). The change in Schmid factor frequency is due to the rotation of grains and subgrains[203–205]. The increase in orientations which readily pyramidal slip indicates that the pyramidal slip system is dominant for tensile deformation of the α-phase. The α-phase has been shown to have a very low Mo content, so pyramidal slip is consistent with the reported deformation behavior of pure Ti[206]. The fraction of points with a high prismatic Schmid factor also increases slightly with increasing deformation, indicating it is a secondary slip system. The fraction of points with a high basal Schmid factor decreases with increasing deformation, so the basal slip system can be considered inactive. The cubic close packed slip system has a large fraction of high Schmid factor points in the undeformed region of all three textures due to its high symmetry, so no noticeable changes due to grain rotation were observed.

Pole figure texture mapping along the tensile direction shows how orientation shifts during deformation from the original texture to a preferential deformation texture. In the α-phase, $\{10\bar{1}0\}_\alpha$-adjacent and $\{0001\}_\alpha$ textures develop in the tensile direction. Applying a uniaxial tensile stress at normal to either $\{10\bar{1}0\}_\alpha$ or $\{0001\}_\alpha$ planes yields a pyramidal Schmid factor of 0.408, given a c/a ratio of 1.56. The c/a ratio was calculated using Bragg's law from the XRD results in §6.2.1. The $\{10\bar{1}0\}_\alpha$-adjacent peak is slightly offset from $\{10\bar{1}0\}_\alpha$ such that it is centered at the orientation which would give the maximum Schmid factor of 0.5. No offset from the $\{0001\}_\alpha$ peak is visible. IPF mapping of the β-phase shows a direct trend towards a $\{101\}_\beta$ texture in the tensile direction, which correlates well with BCC close-packed slip.

The texture shift from grain rotation occurs more strongly in the oriented case. While all three microstructures shift in the same direction, the trend in maximum texture value of the β-

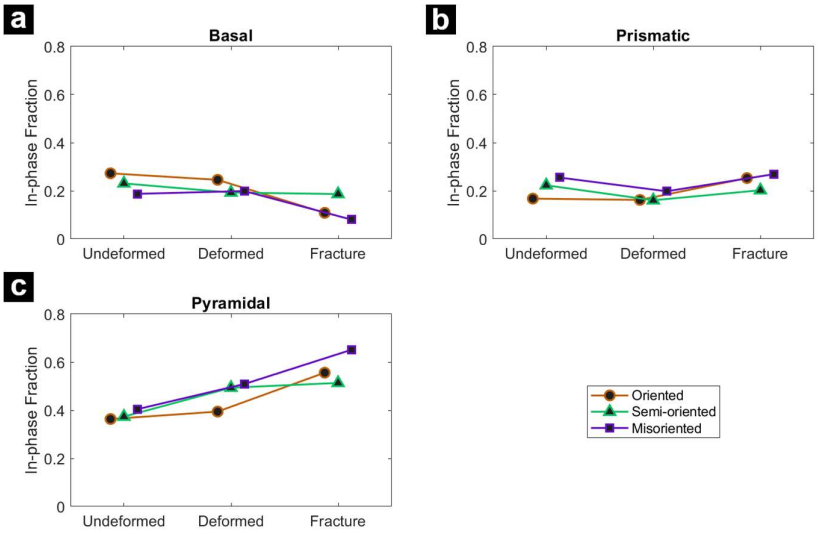

Figure 6.23: High Schmid factor frequency from undeformed, uniform deformation, and fracture regions of the α-phase slip systems: a) basal slip, b) prismatic slip, c) pyramidal slip.

phase T_β remains the same. The deformed misoriented sample remains more isotropic than the deformed semi-oriented sample, which is in turn more isotropic than the deformed oriented sample. Notably, T_β in the uniform deformation region of the oriented sample is unusually high due to a large colony of α_{RX} taking up most of the image so that only one complete parent-β grain was included.

The increased tendency for grain rotation in oriented case is also visible when observing α-phase. The α-phase maximum texture T_α in the undeformed state can increase in the transverse direction over the OMT (Fig. 6.22a, d, g). Despite this, T_α in the uniformly deformed state has the opposite trend (Fig. 6.22b, e, h). The change in T_α between the undeformed and deformed states is from the rotation of α-phase grains toward high pyramidal Schmid factor orientations, which occurs more strongly in the more oriented cases.

The facilitation of grain rotation in the oriented case offers an explanation as to why SSSHR isotropy showed an inverse relation with β-phase orientation isotropy (Fig. 6.20f). The oriented case shows similar compressive SSSHRs in the transverse and build directions, but the build direction SSSHR was clearly higher than the transverse SSSHR in the misoriented case. Grain rotation occurs more readily and uniformly in the oriented case, as shown by the increase in orientation shift. Because the grains rotate more strongly to preferential deformation orientation, the undeformed texture has less of an effect on the steady-state properties for the oriented case. In the misoriented case, grain rotation was suppressed, so factors such as α-phase texture led to a discrepancy between the transverse and build direction SSSHR.

A crack was found 200 μm from the fracture surface in the oriented sample which shows a potential fracture mechanism (Fig. 6.24). The crack occurs along a parent-β boundary at α_{GB}-β interfaces, which has been previously reported in duplex titanium alloys[207]. The crack follows these boundaries very closely, deflecting at interface junctions and stopping growth where the interface parallel to the tensile direction (Fig. 6.24b). It can be seen that α_{GB} grains delaminate from one of the adjacent β grains (Fig. 6.24c). It was shown earlier that all α_{GB} grains had at least one $\{110\}_\beta$-$\{0001\}_\alpha$ interface, but the α_{GB} grains along the crack exclusively show α-β interfaces that are at least 10° away from being $\{110\}_\beta$-$\{0001\}_\alpha$ interfaces (Fig. 6.24d). The lack of $\{110\}_\beta$-$\{0001\}_\alpha$ interfaces after cracking suggests that the crack is preferentially propagating along $\{110\}_\beta$-$\{0001\}_\alpha$ interfaces between α_{GB} grains and the adjacent β grains.

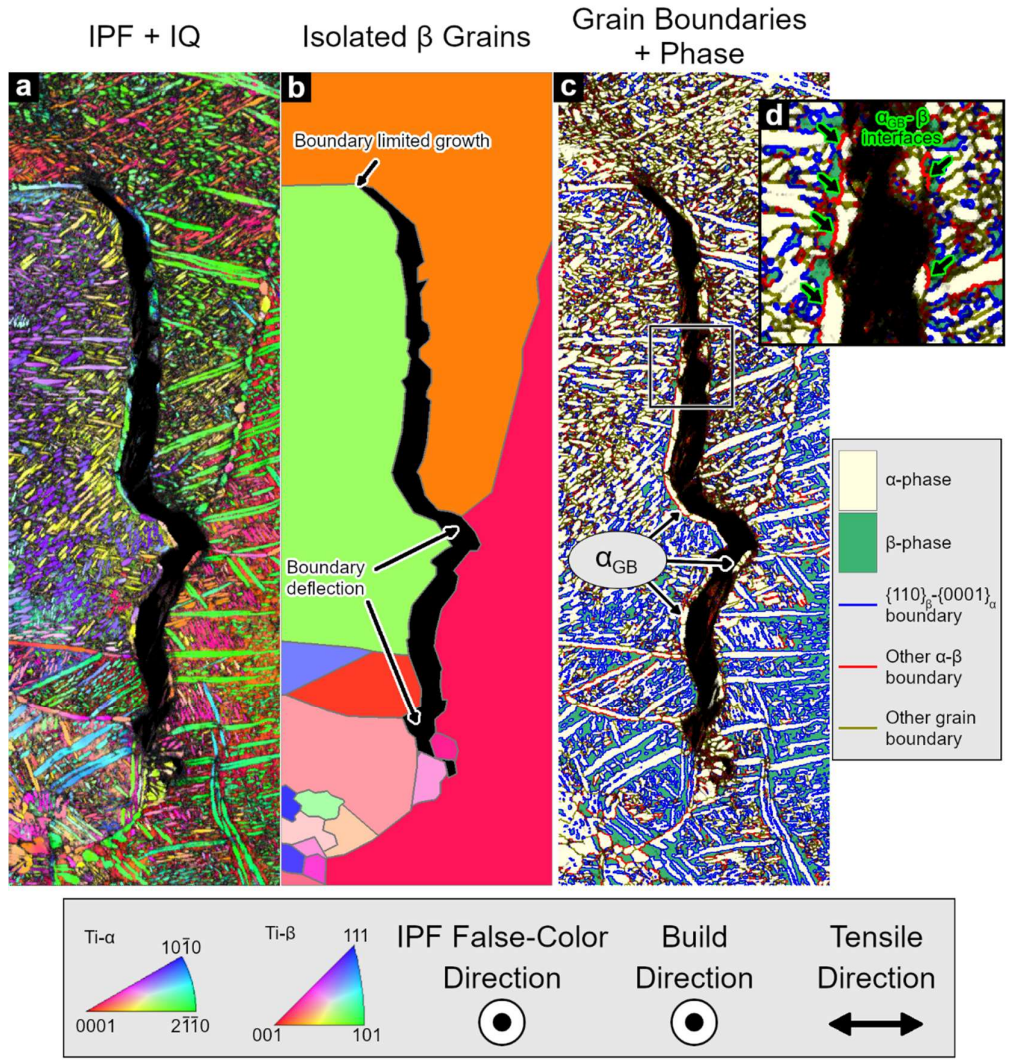

Figure 6.24: EBSD of a crack 200 μm from the fracture surface in the oriented sample. a) IPF + IQ map, b) parent β grains, and c) grain boundaries and phases with d) inlay highlighting α_{GB}-β interfaces.

6.4 Varying TiC Content

6.4.1 Sample Preparation

TiC was added to Ti-10Mo mixed powder in quantities of 0.5 and 1 wt.%. Two billets were printed at each condition using print conditions for an oriented microstructure, with a VED of 130 J/mm^3 and a scan speed of 500 mm/s. The oriented condition was selected because it was shown in Ti-10Mo to yield the most compositionally homogeneous product. One sample was left as-printed while the other underwent the optimized heat treatment of 3 h at 700°C.

6.4.2 Microstructure Observation

The addition of TiC does not induce significant changes in the columnar nature of the as-printed microstructure. The build plane shows no appreciable change in the $\{100\}_\beta$ texture in the build direction (Fig. 6.25a-c). However, the density of dark, unindexable regions increase significantly between 0% and 0.5% TiC. Closer examination of the dark regions as well as the β-phase grains shows α″ laths with widths on the order of 1 μm that were not observed in the 0% TiC sample (Fig. 6.25d-e). In the 0% TiC sample, α″ nano-laths could be observed by TEM (Fig. 6.12d). The addition of carbon, an α stabilizer, appears to promote the martensitic transformation, leading to larger α″ laths in the as-printed state that could be observed by EBSD. Also of note is the presence of TiC particles. Unmelted or partially melted TiC particles are again seen suspended in the matrix, but at dilute concentrations indicating that most of the carbon has been absorbed into solid solution. This is consistent with the findings in CP-Ti and Ti64.

Observation of the vertical plane of the as-printed samples shows a slight change in build plane texture (Fig. 6.25f-j). While the build direction texture remains the same, the build plane texture is more isotropic when TiC is added. This indicates that TiC addition suppresses the formation of preferred orientations in the scan direction. Furthermore, the addition of TiC leads to a reduction in columnar grain width from 15 μm at 0% TiC to 13 μm at 0.5% TiC to 10 μm at 1% TiC. The reduction in columnar grain width can be attributed to the solute drag effect as well as an increase in nucleation from TiC particles.

Observation of the samples heat-treated for 3 h at 700°C shows how the addition of TiC yields a significant change in heat-treated microstructure. The microstructure retains the characteristic α_{RX} and α_M observed in the TiC free case, but α_{GB} is not readily observable (Fig. 6.26e-f, j-k). The microstructure is bimodal and divided into lamellar α_M regions and α_{RX} colonies, which were evenly distributed in the vertical plane as well as the build plane. The lamellar α_M regions have laths on the order of 1 μm. Notably, the α_M laths all show a $\{2\bar{1}\bar{1}0\}$ texture in the build direction. The α_{RX} colonies are globular with very little residual β-phase. The 1% TiC case showed a slightly higher fraction of α_{RX} colonies, likely due to the higher

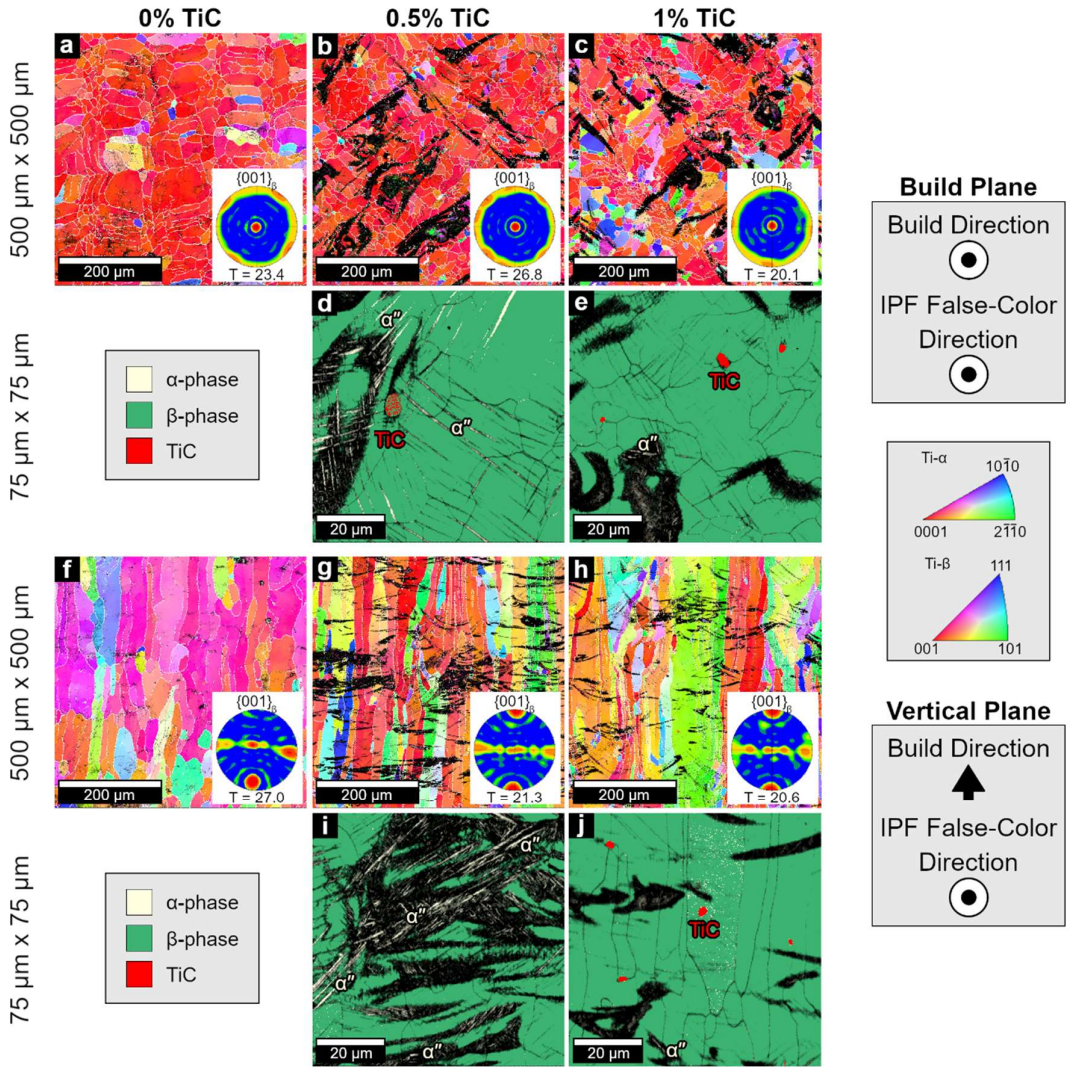

Figure 6.25: EBSD of as-printed Ti-10Mo with increasing TiC content: a-c) build plane IQ and IPF contrast, d-e), build plane IQ and phase contrast, f-h) vertical plane IQ and IPF contrast, i-j), vertical plane IQ and phase contrast.

stability of the α-phase from carbon addition. The α_{RX} shows a strong $\{10\bar{1}2\}$ texture in the build direction. The geometry of these transformations is shown in Fig. 6.27.

In the 1% TiC case, there is partial precipitation of TiC at the grain boundaries, particularly parent-β boundaries (Fig. 6.26k). While 0.5% TiC is completely soluble in Ti-10Mo at 700°C, 1% TiC is not and has a calculated equilibrium concentration of 0.7% (Fig. 6.28). Unlike the Ti64 case, the TiC appears to precipitate out to near-equilibrium concentrations.

The bimodal microstructure of the heat-treated sample with 0.5% TiC is also observable by TEM, which contains α_{RX} regions and α_M regions (Fig. 6.29). The lack of apparent α_{GB} can be seen in Fig. 6.29b, where a parent-β boundary is observable. The parent-β boundary shows the presence of an alternating α-β lath-like structure instead of the large α_{GB} grain observed in

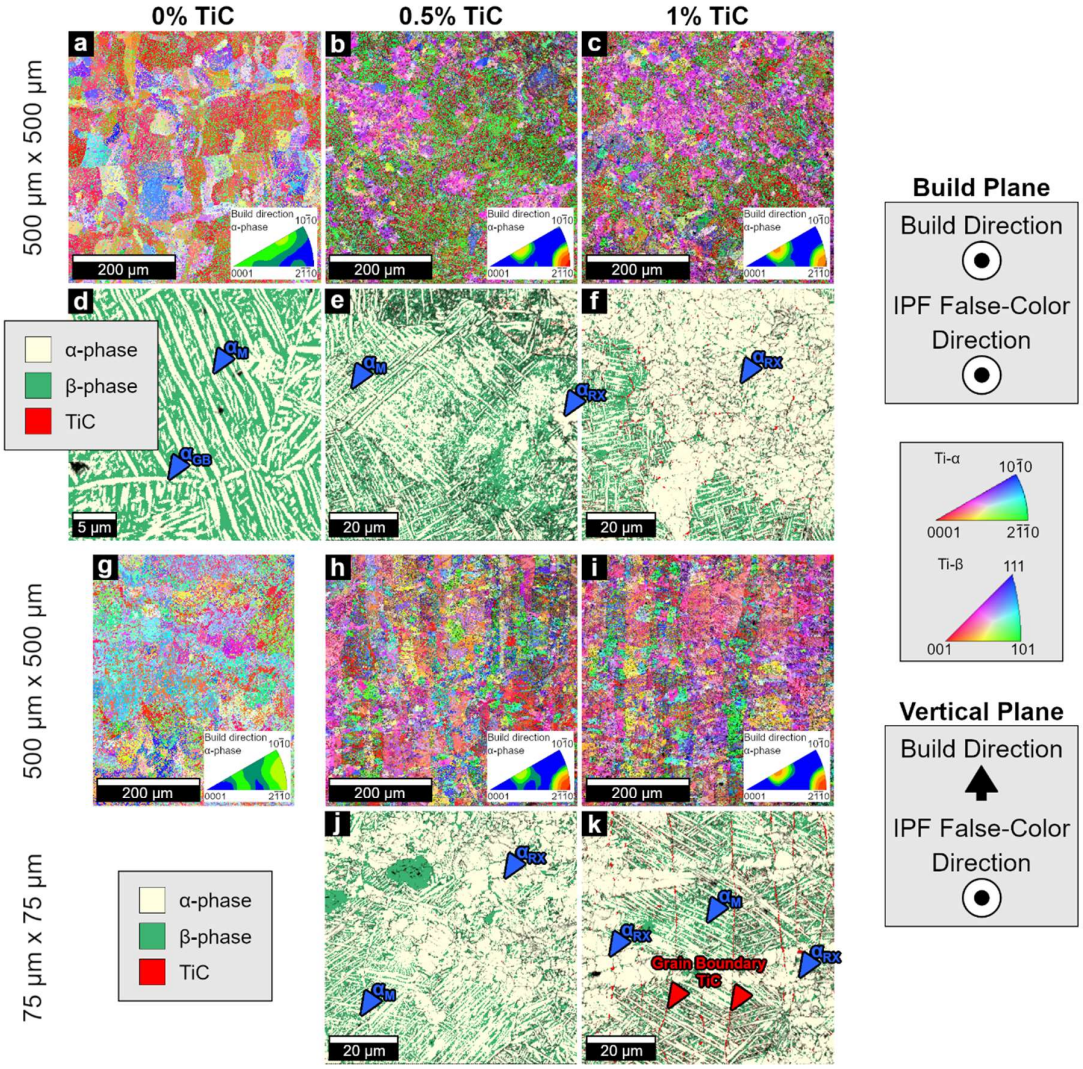

Figure 6.26: EBSD of Ti-10Mo heat treated for 3 h at 700°C with increasing TiC content: a-c) build plane IQ and IPF contrast, d-f), build plane IQ and phase contrast, g-i) vertical plane IQ and IPF contrast, j-k), vertical plane IQ and phase contrast.

the sample without TiC in Fig. 6.16. Observation of the parent-β boundary shows no evidence of TiC precipitation, which is consistent with full carbon solubility for 0.5% TiC at 700°C. The recrystallized regions are shown to be composed of pearlite-type duplex structures with a lamella width of 200-400 µm. SAD patterns show that trace amounts of ω-phase are present in the β-phase lamellae (Fig. 6.29d, f).

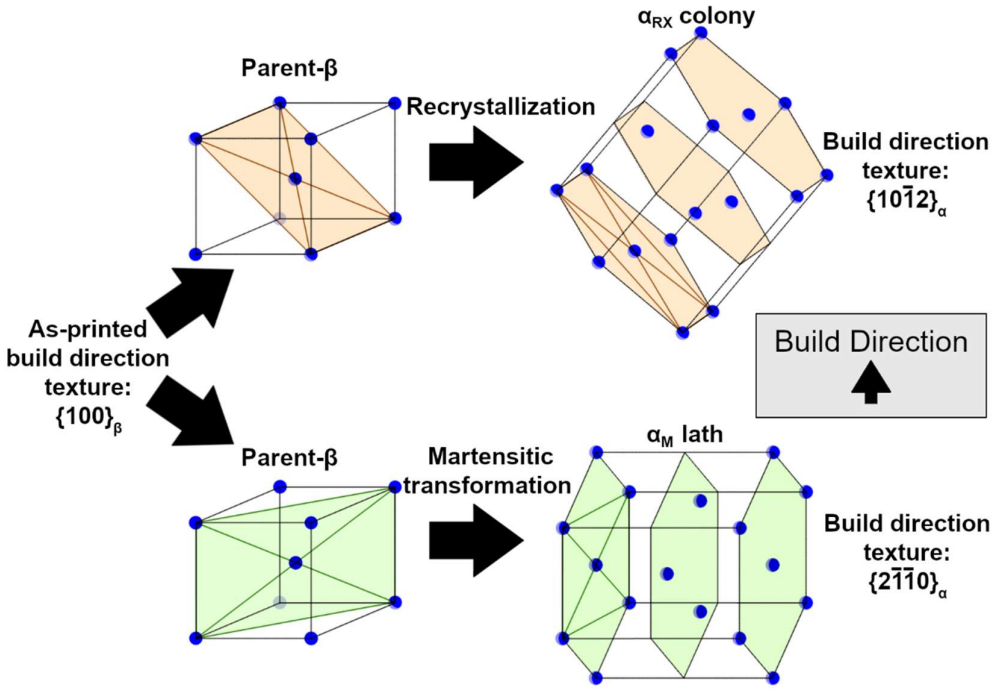

Figure 6.27: Crystallography of the difference in the α_{RX} and α_M transitions.

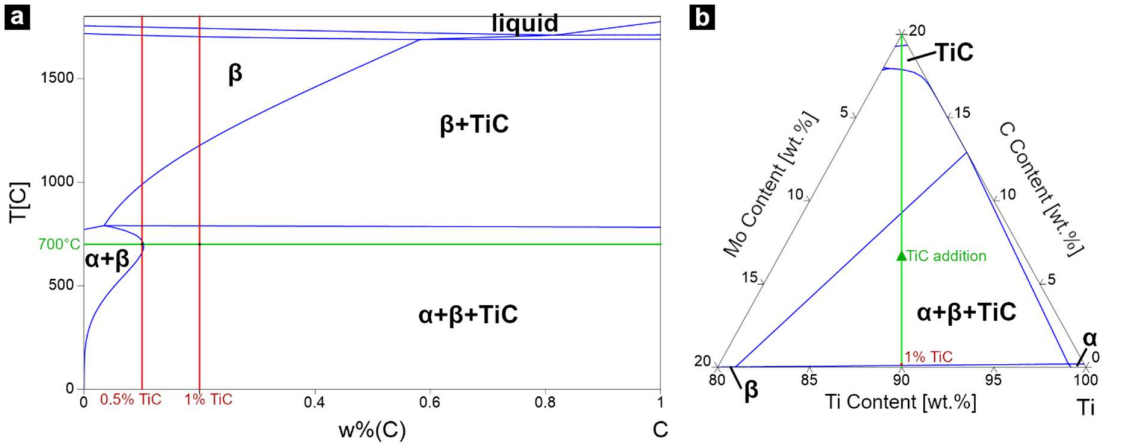

Figure 6.28: Calculated phase diagrams of the Ti-Mo-C system. a) Pseudo-binary phase diagram of Ti-10Mo and carbon, b) ternary isotherm at 700°C.

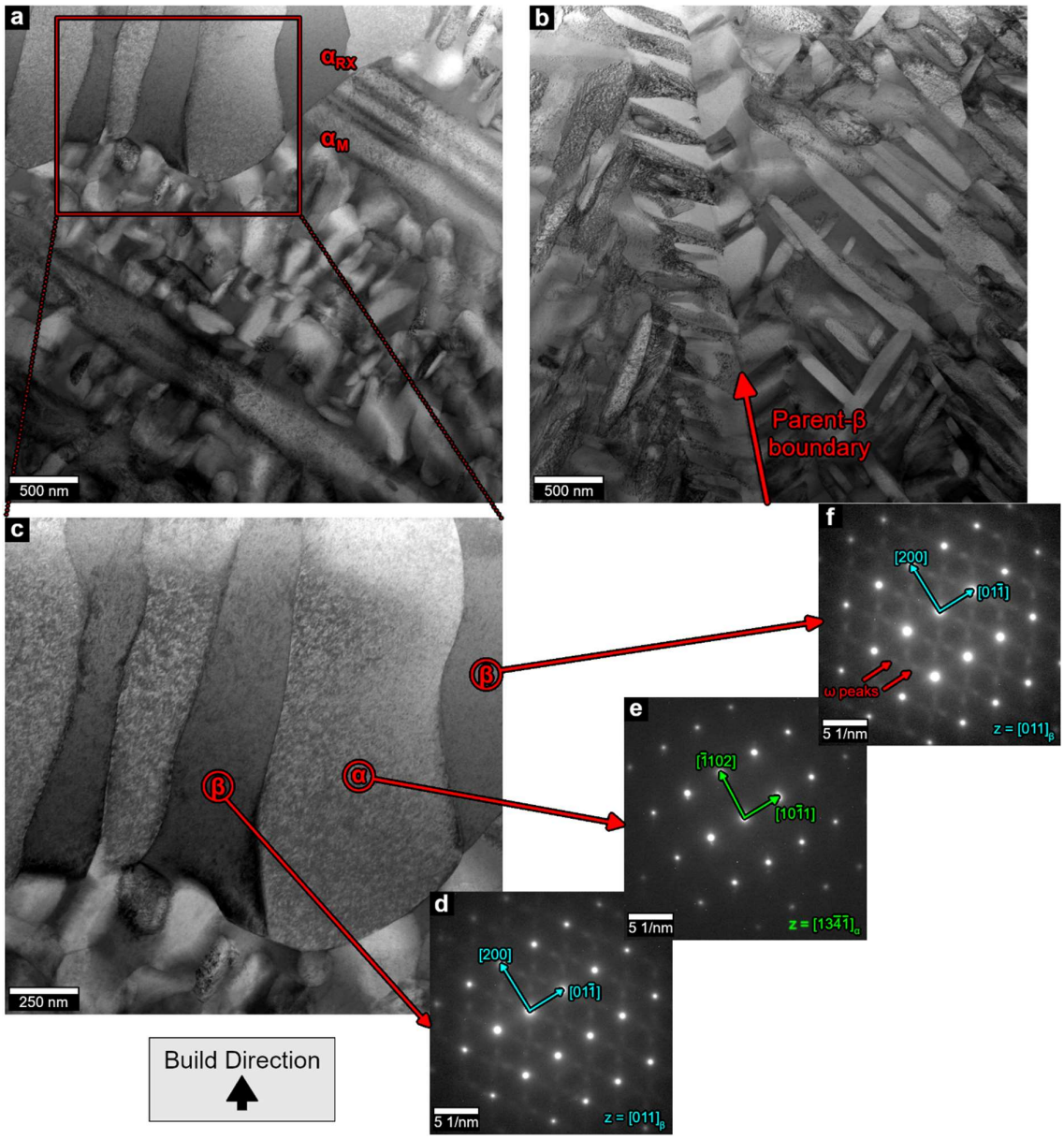

Figure 6.29: TEM of Ti-10Mo with 0.5% TiC heat treated for 3 h at 700°C. a) 40kx magnification of an α_{RX} - α_M interface, b) 40kx magnification of a prior-β grain boundary, c) 100kx magnification α_{RX}, d-f) SAD patterns of α_{RX}.

6.4.3 Mechanical Testing

Tensile testing was performed on transverse direction samples in both the as-printed and heat-treated conditions (Fig. 6.30). The results are listed in Table 6.7. The as-printed condition has samples that are extremely brittle and was previously noted as a hyper-brittle case in §6.3.2. The as-printed 0% TiC sample shows no values in Table 6.7 due to its highly brittle nature. Tensile samples of this condition either cracked before testing or failed outside of the tensile gauge area, so no valid data was obtained. While all three compositions are brittle, the 0.5% TiC case shows a noticeably higher ductility. This can be attributed to carbon suppressing formation of the embrittling ω-phase[170]. As before in the CP-Ti and Ti64 cases, increasing the TiC content from 0.5% to 1% reduces ductility.

The samples heat treated for 3 h at 700°C show the most unusual dependency of mechanical properties on TiC concentration in that there is almost no dependency of mechanical properties on TiC concentration (Fig. 6.30b). All three samples showed yield strength, ultimate tensile strength, and ductility within 5% of each other. Of the three concentrations tested, the case without TiC addition had the highest strength and ductility. The

Table 6.7: Tensile properties.

Heat treatment	TiC content [wt.%]	Yield stress [MPa]	UTS [MPa]	Ductility [%]
As-printed	0	-	-	-
	0.5	1025 ± 29	1122 ± 23	2.3 ± 0.2
	1	1046 ± 17	1088 ± 16	1.3 ± 0.2
3 h at 700°C	0	837 ± 11	867 ± 9	14.3 ± 0.4
	0.5	810 ± 3	862 ± 1	12.3 ± 1.7
	1	824 ± 3	855 ± 5	13.7 ± 0.3

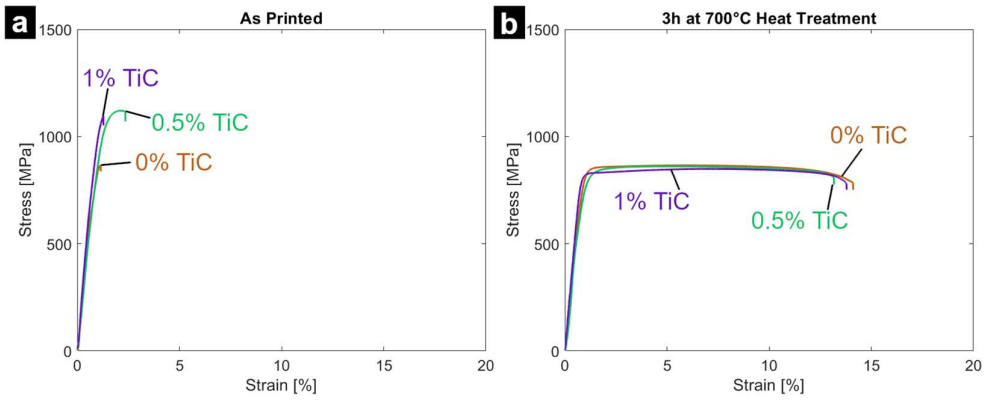

Figure 6.30: Uniaxial tensile testing of Ti-10Mo with added TiC in the a) as-printed and b) heat treated for 3 h at 700°C conditions.

slightly higher strength can be attributed to unsuppressed ω-phase formation. The resilience of the mechanical properties to TiC addition is particularly notable given that the microstructures observed in Fig. 6.26 showed a distinct change in microstructure between 0% and 0.5% TiC involving the development of α_{RX} colonies and a change in α-phase orientation. Furthermore, TiC precipitates formed only at a concentration of 1% TiC but showed no effect on mechanical properties. The independence of mechanical properties on the microstructural changes highlights the resiliency of bimodal duplex systems.

TEM of the area near the fracture surface of the 0.5% TiC case shows the deformation distribution in the duplex structure (Fig. 6.31). The α_M laths show a moderately wavy morphology but retain their high aspect ratio (Fig. 6.31a-b). An α_{RX} colony shows no

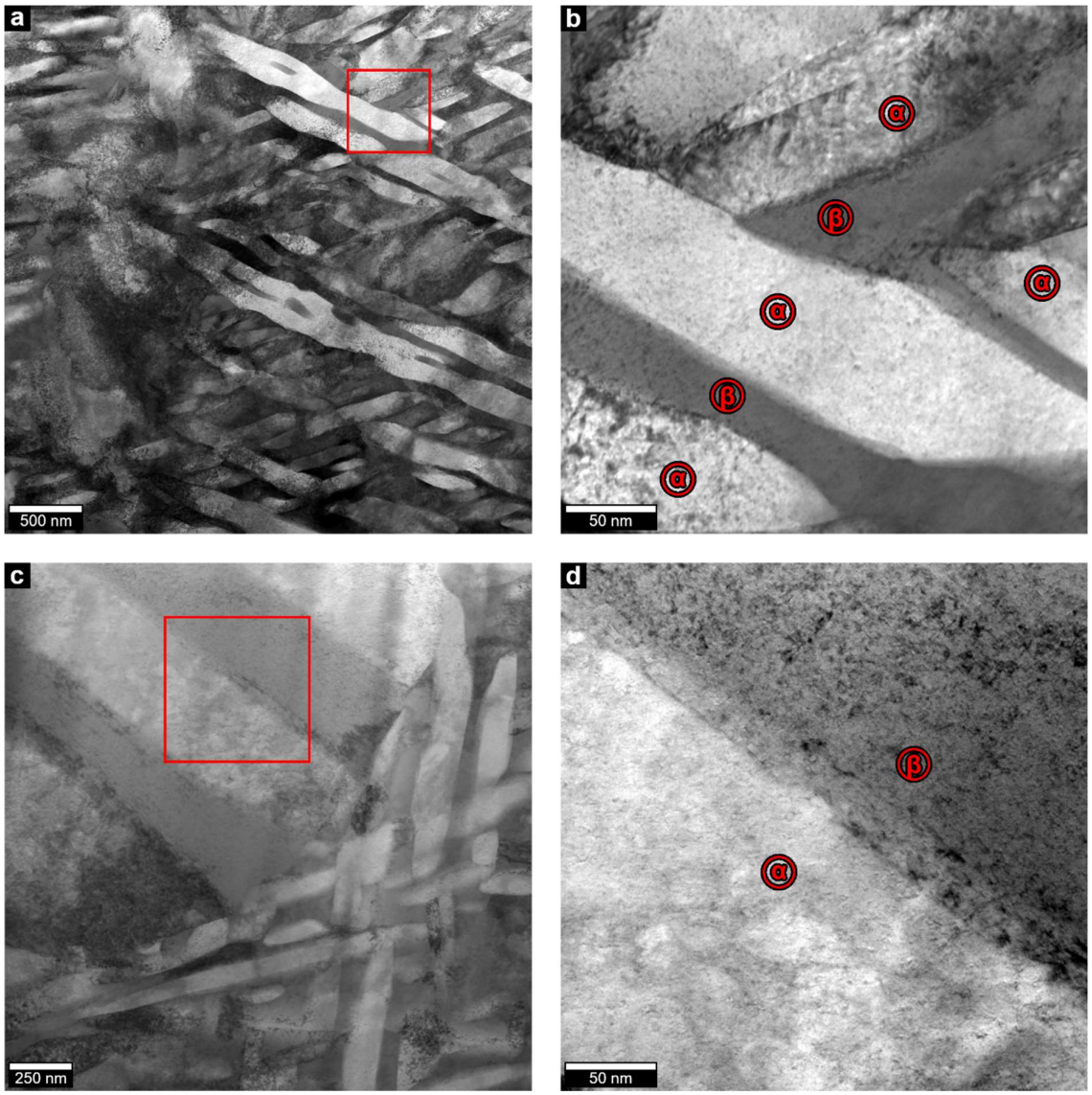

Figure 6.31: TEM of Ti-10Mo with 0.5% TiC heat treated for 3 h at 700°C from near the fracture surface. a-b) α_M lamellar region, c-d) α_{RX} colony.

significant deformation (Fig. 6.31c-d). The high magnification TEM images are inconclusive as to the phase distribution of dislocations. The β-phase is the softest phase present, so it would naturally be the most deformed and defect-rich.

Grain rotation can still be observed after TiC addition (Fig. 6.32). In the undeformed state, the addition of TiC increases the texture of both the α-phase and β-phase. After uniform deformation, the difference in texture between the different TiC concentrations is less significant, a trend which holds until fracture. The 0.5% TiC sample at fracture shows the weakest texture due to the low IQ of its highly deformed microstructure. For all three TiC concentrations at fracture, the IQ is reduced, particularly in the β-phase. The low IQ of the β-phase indicates that most deformation occurs in the β-phase, which is consistent with previous results.

When up to 1% TiC is added to Ti-10Mo, the carbon is strongly segregated into the α-phase. In Ti-10Mo at 700°C equilibrium, the α-phase has only 0.8% Mo, while the β-phase has 17.8% Mo. When 1% TiC is added, the Mo concentration in the α-phase changes negligibly

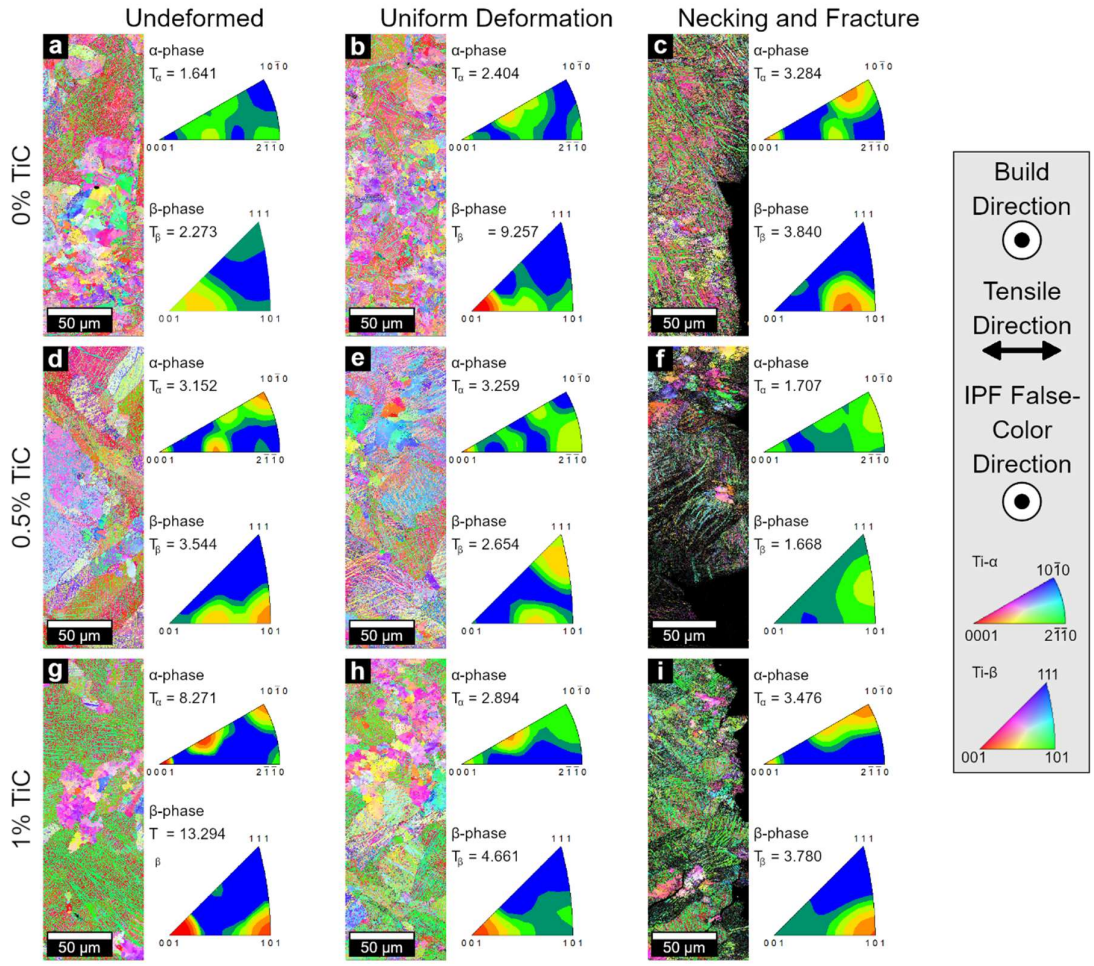

Figure 6.32: EBSD of the build plane of tensile samples using a combined IQ-IPF contrast. IPF texture plots in the tensile direction are shown alongside each image for each phase.

while increasing to 19.0% in the β-phase due to a lower fraction of β-phase (Fig. 5.28b). The lower β-phase fraction is caused by the stabilization of the α-phase by carbon, which preferentially occurs in the α-phase at a concentration of 0.2% while only occurring in the β-phase in trace amounts.

Because the addition of TiC causes no significant change to the β-phase composition, the deformation mechanics are largely unchanged. Ti-10Mo was shown to deform as a soft β-phase matrix with harder α-phase laths. When TiC is added, the α-phase laths are hardened by the increased carbon content. However, the β-phase remains relatively unchanged, so the primary deformation is also unchanged.

Grain rotation of the α-phase supports that deformation mechanics do not change with TiC addition (Fig. 6.33). The 1% TiC sample shows a slightly lower fraction of grains oriented towards basal and pyramidal slip in the undeformed state due to its local texture. Once deformation has occurred, the fraction of grains oriented for each slip system behaves similarly at all TiC concentrations. The pyramidal system remains the dominant slip system, particularly at fracture (Fig. 6.33c).

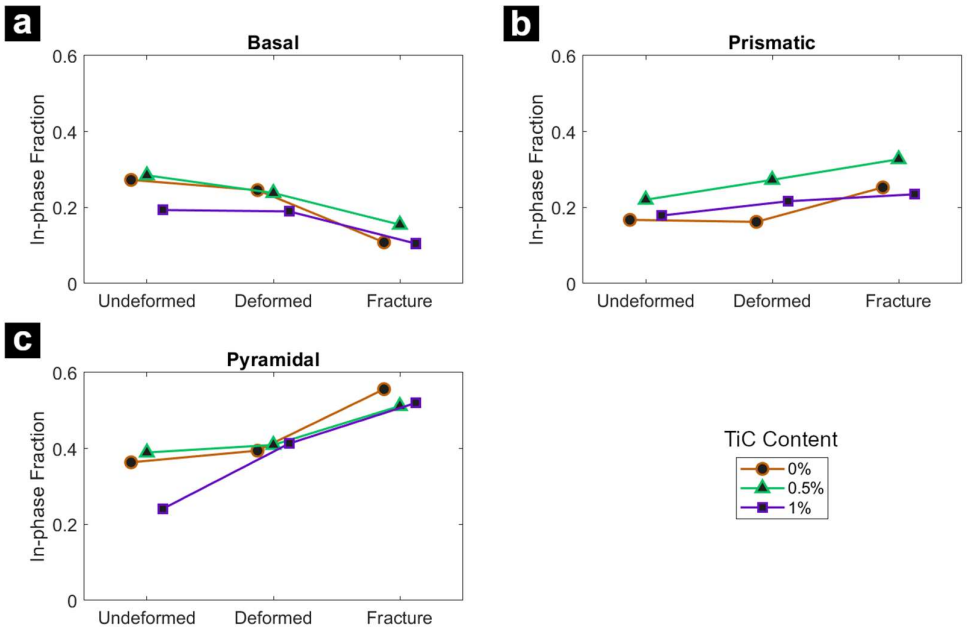

Figure 6.33: High Schmid factor in-phase fraction from undeformed, uniform deformation, and fracture regions of the α-phase slip systems: a) basal slip, b) prismatic slip, c) pyramidal slip.

6.5 Conclusions

In this chapter, Ti-10Mo was manufactured by L-PBF. The effect of print parameters, namely volumetric energy density and laser scan speed, on microstructure were thoroughly observed and characterized. Once ideal conditions were found for Ti-10Mo, TiC was added up to 1%. The effect of carbon on the microstructure and mechanical properties was also characterized. The following conclusions were obtained:

- An oriented-to-misoriented transition was discovered in Ti-10Mo occurred at low volumetric energy densities of 70-90 J/mm^3, or high scan speeds of 1200-1700 mm/s. XRD relative peak intensities were shown to be a rapid and accurate method of identifying the OMT and were used to map microstructure over the design space.
- The scan speed OMT was attributed to the faster solidification interface speed increasing equiaxed grain zone size and lower penetration depths inhibiting the continuity of grain orientations across build layers.
- The as-printed and solution treated Ti-10Mo had a high density of ω nanoprecipitates and α″ martensite, leading to extreme brittleness. Heat treating the as-printed material for 3 h at 700°C yielded a duplex α+β microstructure with significantly improved ductility.
- Decreasing the orientation of the as-printed microstructure of Ti-10Mo led to higher yield stress and yield stress isotropy in the heat-treated material, but strain hardening became less isotropic due to the suppression of grain rotation.
- In tension, plastic deformation of the α-phase occurs via pyramidal dislocation slip, and crack propagation in tension is suggested to preferentially occur along the {110}β-{0001}α interfaces of grain boundary α.
- The addition of TiC led to larger α″ laths in the as-printed condition and a highly oriented, bimodal microstructure consisting of a duplex lamellar region and recrystallized α-phase colonies after heat treatment.
- TiC addition led to a slight increase in ductility as-printed but had no significant effect on the heat-treated condition.

These results quantify the behavior of Ti-10Mo manufactured by L-PBF. Deformation mechanisms and behaviors were also investigated as a reference point for future parameter optimization and alloy design. TiC was shown to be an effective additive to Ti-10Mo in the as-printed condition because it increases ductility.

Chapter 7:
Conclusion

7.1 Conclusions

This dissertation showed the effect of a super-saturated carbon solid solution on the microstructural and mechanical properties of titanium and its alloys. The studied materials were produced by mechanically mixing feedstock powders, then in-situ alloying during L-PBF. Carbon, in the form of TiC, was added to CP-Ti, Ti64, and Ti-10Mo at concentrations of up to 1 wt.% TiC. In order to properly assess the efficacy of carbon addition on each alloy, the effects of L-PBF process parameters as well as post-processing heat treatments were evaluated.

Carbon addition to CP-Ti produced the most dramatic results. The addition of the minimum amount of TiC, 0.25%, changed the structure of α-phase grains from large, columnar grains to fine, martensitic grains. Further addition of TiC refined the martensitic grain size. It was shown that through a combination of grain refinement and solid solution strengthening, yield stress was doubled from 328 MPa without TiC to 660 MPa with 1% TiC. Remarkably, this increment came with no associated loss to ductility. In fact, ductility was highest at a TiC concentration of 0.5%.

Carbon was also shown to improve the mechanical performance of Ti64, albeit less dramatically. The solid solution from 0.75% added TiC was shown to be stable across a wide variety of heat treatments, but hot extrusion induced large TiC precipitates that deteriorated mechanical properties. Of the heat treatments investigated, 1 h at 500°C was shown to maintain superior strength while relieving the residual stresses of L-PBF, and 3 h at 700°C was shown to anneal the material such that an excellent balance of strength and ductility could be achieved. The addition of carbon unilaterally increased strength across both heat treatments, but only

increased ductility in the samples heat treated for 3 h at 700°C at concentrations of up to 0.5%. The increase in ductility was attributed to carbon inhibiting prismatic dislocation slip.

Ti64 and CP-Ti with added TiC exhibited martensitic grain structures as-printed. In both systems, increasing carbon content decreased the martensitic lath size. While carbon decreased the initial grain size, it was shown that carbon increases the increment of grain size after heat treatment. Unusually, this was shown not to be from increasing the grain interface growth rate, but instead by promoting fusion of multiple martensitic laths of the same orientation. The replicability of the grain fusion effect across CP-Ti and Ti64 confirms that it is caused by increased carbon content, although the mechanisms are not yet fully understood.

The Ti-10Mo system was first optimized and understood without TiC. When selecting print parameters, an oriented-to-misoriented transition was identified and mapped using a correlative XRD function. The OMT occurred between VEDs of 90 to 70 J/mm^3 and scan speeds of 1200 to 1700 mm/s. The scan speed OMT was determined to be caused by decreasing laser penetration and increasing equiaxed grain nucleation at higher solidification velocities. Ti-10Mo displayed a large amount of ω-phase precipitation and α″ martensite both as-printed and after multiple different heat treatments, leading to brittle mechanical performance. Heat treating for 3 h at 700°C was found to improve mechanical performance by allowing a large fraction of α-phase to form. The resulting phase segregation of molybdenum inhibited the formation ω-phase precipitates. The effect of the OMT on mechanical properties at a constant energy density was determined. Decreasing orientation increased transverse direction ductility and build direction yield strength. The isotropy of yield strength increased with decreasing orientation, but the isotropy of strain hardening decreased due to smaller grains suppressing the grain rotation effect.

Heat treated Ti-10Mo was found to be mechanically insensitive to the addition of TiC. After a heat treatment of 3 h at 700°C, the yield stress decreased from 837 MPa to 824 MPa, and ductility decreased from 14.3% to 13.7%. These changes to mechanical properties are remarkably small for the amount of added TiC. The insensitivity of Ti-10Mo to TiC was attributed to the phase segregation of carbon into the α-phase and grain boundary precipitates, while yield and deformation is governed by the β-phase. Within the β-phase, the slightly increased presence of carbon decreased ω-phase precipitation, leading to the decreased yield stress after heat treatment. The suppression of the ω-phase can also be seen in the mechanical behavior of the as-printed samples, where the sample with 0.5% added TiC had the highest ductility.

Overall trends show that while carbon is a powerful strengthening agent in CP-Ti, its efficacy diminishes with increasing β-phase stability. The addition of 1% TiC increased the yield strength of CP-Ti by up to 332 MPa and the yield strength of Ti64 by up to 299 MPa but decreased the yield strength of Ti-10Mo by 13 MPa. While the maximum increment to strength

in Ti64 is comparable to that of CP-Ti, it came at the cost of ductility for that sample. However, across all three systems, there was always at least one heat treatment at which adding TiC increased ductility. For CP-Ti, it was both the 1 h at 500°C and 3 h at 700°C heat treatments, for Ti64, it was at 3 h at 700°C, and for Ti-10Mo it was as-printed. In all cases, the maximum ductility was when 0.5% TiC was added, indicating that this is the critical concentration for carbon addition. 0.5% TiC is approximately equal to 0.1% C across all three systems.

Carbon is thereby determined to be an effective strengthening agent for α-phase or near α-phase titanium alloys at concentrations of up to 0.1 wt.%. It can be used as a cheap, non-toxic, readily available additive for high strength titanium applications. While carbon cannot be recommended for use as a strengthening agent for near-β alloys, duplex alloys with a high β-phase fraction are shown to be mechanically tolerant of a carbon content of up to 0.2 wt.%. Therefore Ti-10Mo can be robustly used in applications with variable carbon contamination.

7.2 Recommendations for Future Work

The development of this thesis led to several additional potential topics of research. While carbon was shown to contribute to grain fusion of martensitic laths during heat treatment, the mechanism by which it contributes this is unexplored. More detailed grain growth observations and simulations are required to fully understand this effect. First principles simulations would also assist in the confirmation of carbon's selective pinning of prismatic dislocations proposed herein.

The effect of carbon in other titanium alloys should also be considered. Within this study, carbon was always segregated into the α-phase. Higher β-phase stability systems such as Ti-15Mo or Ti-20V would allow carbon's effect on the β-phase to be better understood.

Appendix A
Nitrogen Accumulation

The Nitrogen Accumulation Problem

Occasionally, samples showed nitrogen accumulation during printing. This is particularly notable in the CP-Ti samples heat treated for 3 h at 700°C from §4.2.1. The nitrogen content of the 0.5 and 1% TiC samples heat treated is significantly higher than the other samples. This dramatic increase in nitrogen content is non-uniform. Nitrogen content is lower close to the substrate and higher near the top of the print (Fig. A.1). This nitrogen accumulation problem (NAP) is a repeated issue over the course of this project and remains unresolved. In NAP samples, the nitrogen content is much higher and increases with z-height. This accumulation is consistent over all samples from a single build plate such that at a given z-height, every sample has a similar nitrogen content. However, even if two prints were made under identical conditions, one build plate may show NAP even if the other does not. NAPs were more likely to occur when a small leak was introduced into the build chamber, however they were not guaranteed to occur because small leaks were automatically offset by the addition of argon gas.

The NAP appears to originate from nitrogen-rich sputter products being formed during printing, then accumulating over the course of the print. After printing a NAP sample, sputter was collected from between the build cylinder and the filter intake (Fig. A.2a). The nitrogen and oxygen content of the feedstock powder, the build cylinder powder, the waste cylinder powder, and the sputter were compared (Fig. A.2b). The sputter is rich in nitrogen and oxygen. Therefore, nitrogen absorption occurs within the highly reactive melt pool. However, the steady state oxygen content in the build chamber is measured as less than 1.5 ppm without a leak for

the entirety of the print. Assuming the ratio of nitrogen to oxygen remains constant from atmospheric, that gives a nitrogen content of less than 5.5 ppm. In a 29,000 cm^3 process chamber at atmospheric pressure, there is less than 0.3 mg of nitrogen. Each bar has a mass of about 22 g, so a 2-bar build plate with an average nitrogen increase of 0.05% absorbs about 11 mg of nitrogen, much more than the expected atmospheric amount. The source of the nitrogen, as well as why it increases with build height, remains unsolved.

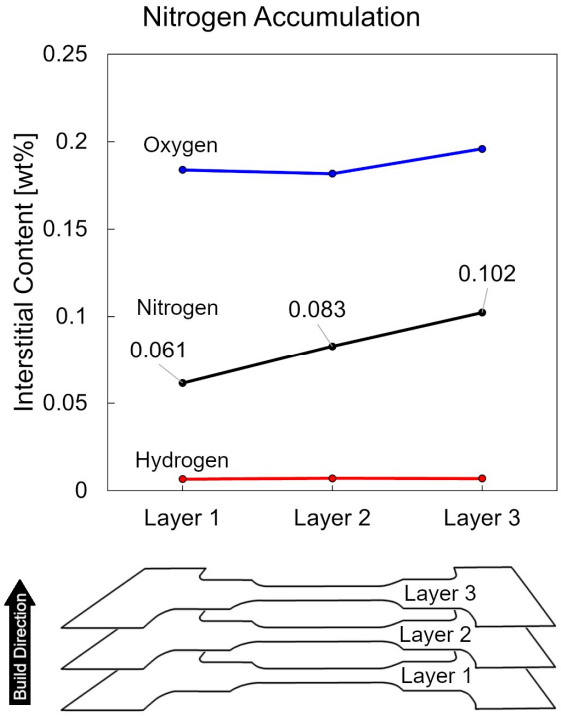

Figure A.1: Nitrogen accumulation in CP-Ti with 0.5% TiC

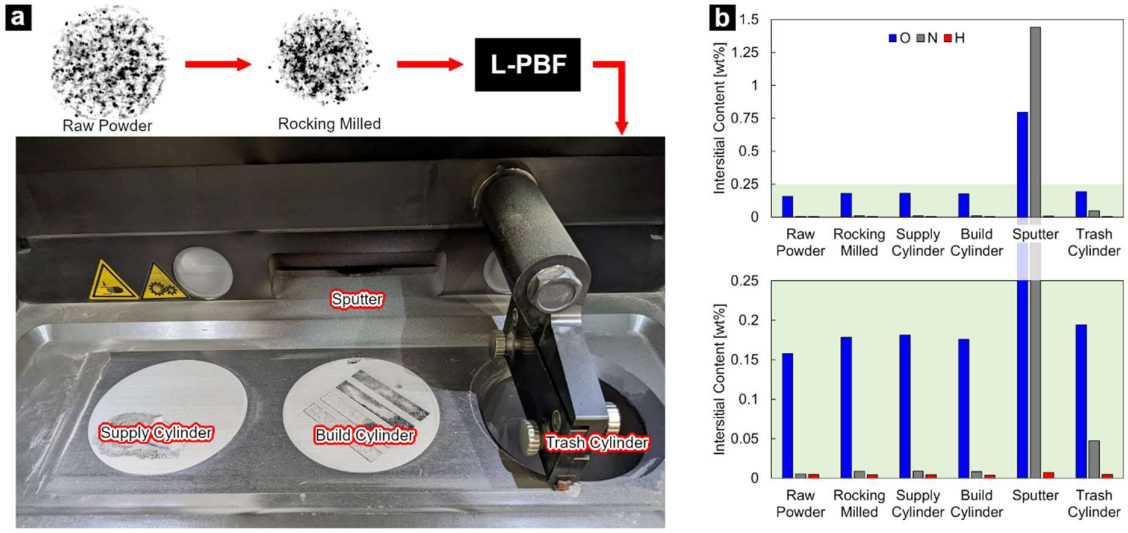

Figure A.2: Oxygen, nitrogen, and hydrogen content of powders during the L-PBF process. a) Powder sampling locations. b) Elemental composition.

References

1. UET 5, 0081 artifact entry. *Cuneiform Digital Library Initiative* https://cdli.ucla.edu/P414985 (2023).
2. Oppenheim, A. L. *Letters from Mesopotamia*. *The University of Chicago Press* (1967).
3. Yumak, N. & Aslantaş, K. A review on heat treatment efficiency in metastable β titanium alloys: the role of treatment process and parameters. *Journal of Materials Research and Technology* **9**, 15360–15380 (2020).
4. Kobayashi, Y. *et al.* Effect of forging ratio and grain size on tensile and fatigue strength of pure titanium forgings. *Journal of the Society of Materials Science, Japan* **54**, 66–72 (2005).
5. Rahulan, N., Sharma, S. S., Rakesh, N. & Sambhu, R. A short review on mechanical properties of SLM titanium alloys based on recent research works. *Mater Today Proc* (2021) doi:10.1016/j.matpr.2021.10.184.
6. Williams, J. C. & Boyer, R. R. Opportunities and issues in the application of titanium alloys for aerospace components. *Metals (Basel)* **10**, (2020).
7. Nguyen, H. D. *et al.* A critical review on additive manufacturing of Ti-6Al-4V alloy: Microstructure and mechanical properties. *Journal of Materials Research and Technology* **18**, 4641–4661 (2022).
8. Matsumoto, H. " Metallurgy " of Structural Titanium Alloys : Past-Current-Future. 49–55 (2022).
9. Wollmann, M., Kiese, J. & Wagner, L. Properties and applications of titanium alloys in transport. *Ti 2011 - Proceedings of the 12th World Conference on Titanium* **2**, 837–844 (2012).
10. Liu, Z., He, B., Lyu, T. & Zou, Y. A Review on Additive Manufacturing of Titanium Alloys for Aerospace Applications: Directed Energy Deposition and Beyond Ti-6Al-4V. *JOM* **73**, 1804–1818 (2021).
11. Anil Kumar, V., Gupta, R. K., Prasad, M. J. N. V. & Narayana Murty, S. V. S. Recent advances in processing of titanium alloys and titanium aluminides for space applications: A review. *J Mater Res* **36**, 689–716 (2021).
12. Bower, K., Murray, S., Reinhart, A. & Nieto, A. Corrosion resistance of selective laser melted Ti–6Al–4V alloy in salt fog environment. *Results in Materials* **8**, 100122 (2020).
13. Zhang, L.-C. & Attar, H. Selective Laser Melting of Titanium Alloys and Titanium Matrix Composites for Biomedical Applications: A Review . *Adv Eng Mater* **18**, 463–475 (2016).
14. Steinemann, S. G. Metal implants and surface reactions. *Injury* **27**, (1996).
15. Boyer, R. R. Aerospace applications of beta titanium alloys. *JOM* **46**, 20–23 (1994).
16. Cotton, J. D. *et al.* State of the Art in Beta Titanium Alloys for Airframe Applications. *JOM* **67**, 1281–1303 (2015).

17. Boyer, R. R. & Briggs, R. D. The Use of β Titanium Alloys in the Aerospace Industry. *J Mater Eng Perform* **14**, 681–685 (2005).
18. Oliveira, N. & Guastaldi, A. Electrochemical stability and corrosion resistance of Ti–Mo alloys for biomedical applications. *Acta Biomater* **5**, 399–405 (2009).
19. Gao, Z., Luo, H., Li, Q. & Wan, Y. Preparation and Characterization of Ti-10Mo Alloy by Mechanical Alloying. *Metallography, Microstructure, and Analysis* **1**, 282–289 (2012).
20. Gambogi, J. *Titanium mineral concentrates*. *U.S. Geological Survey, Mineral Commodity Summaries* (2023).
21. Nguyen, T. H. & Lee, M. S. A Review on the Recovery of Titanium Dioxide from Ilmenite Ores by Direct Leaching Technologies. *Mineral Processing and Extractive Metallurgy Review* **40**, 231–247 (2019).
22. Titanium. *Observatory of Economic Complexity* https://oec.world/en/profile/hs/titanium (2023).
23. Raabe, D. The Materials Science behind Sustainable Metals and Alloys. *Chem Rev* **123**, 2436–2608 (2023).
24. Lee, H. *et al.* Lasers in additive manufacturing: A review. *International Journal of Precision Engineering and Manufacturing - Green Technology* **4**, 307–322 (2017).
25. Seong, S., Younossi, O., Goldsmith, B., Lang, T. & Neumann, M. *Titanium: Industrial Base, Price Trends, and Technology Initiatives*. *Distribution* (RAND Corporation, 2009). doi:10.7249/MG789.
26. Fereiduni, E., Ghasemi, A. & Elbestawi, M. Selective laser melting of aluminum and titanium matrix composites: Recent progress and potential applications in the aerospace industry. *Aerospace* **7**, 77 (2020).
27. Wood, R. M. The Lattice Constants of High Purity Alpha Titanium. *Proceedings of the Physical Society* **80**, 783–786 (1962).
28. Jain, A. *et al.* Commentary: The Materials Project: A materials genome approach to accelerating materials innovation. *APL Mater* **1**, 011002 (2013).
29. Pawar, R. R. & Deshpande, V. T. The anisotropy of the thermal expansion of α-titanium. *Acta Crystallographica Section A* **24**, 316–317 (1968).
30. Levinger, B. W. Lattice Parameter of Beta Titanium at Room Temperature. *JOM* **5**, 195–195 (1953).
31. Hammond, C. & Kelly, P. M. The crystallography of titanium alloy martensites. *Acta Metallurgica* **17**, 869–882 (1969).
32. Yan, J. Y. & Olson, G. B. Computational thermodynamics and kinetics of displacive transformations in titanium-based alloys. *J Alloys Compd* **673**, 441–454 (2016).

33. Jafari, M., Vaezzadeh, M. & Noroozizadeh, S. Thermal Stability of α Phase of Titanium by Using X-Ray Diffraction. *Metallurgical and Materials Transactions A* **41**, 3287–3290 (2010).
34. ASTM. Standard Specification for Titanium and Titanium Alloy Castings. *ASTM International* **ASTM B367**, (2017).
35. Zhao, S. *et al.* Cryoforged nanotwinned titanium with ultrahigh strength and ductility. *Science* **373**, 1363–1368 (2021).
36. Wang, Q. *et al.* Microstructure evolution of commercial pure titanium during interrupted in situ tensile test. *Metallurgical and Materials Transactions A* **52**, 2477–2488 (2021).
37. Arrazola, P. J. *et al.* Machinability of titanium alloys (Ti6Al4V and Ti555.3). *J Mater Process Technol* **209**, 2223–2230 (2009).
38. Jing, R. *et al.* Structure and mechanical properties of Ti–6Al–4V alloy after zirconium addition. *Materials Science and Engineering: A* **552**, 295–300 (2012).
39. Yang, Y. *et al.* Crystallographic features of α variants and β phase for Ti-6Al-4V alloy fabricated by selective laser melting. *Materials Science and Engineering: A* **707**, 548–558 (2017).
40. Wagoner Johnson, A. J., Bull, C. W., Kumar, K. S. & Briant, C. L. The influence of microstructure and strain rate on the compressive deformation behavior of Ti-6Al-4V. *Metallurgical and Materials Transactions A* **34**, 295–306 (2003).
41. Chong, Y., Bhattacharjee, T., Park, M.-H., Shibata, A. & Tsuji, N. Factors determining room temperature mechanical properties of bimodal microstructures in Ti-6Al-4V alloy. *Materials Science and Engineering: A* **730**, 217–222 (2018).
42. Bridier, F., Villechaise, P. & Mendez, J. Analysis of the different slip systems activated by tension in a α/β titanium alloy in relation with local crystallographic orientation. *Acta Mater* **53**, 555–567 (2005).
43. Li, H., Boehlert, C. J., Bieler, T. R. & Crimp, M. A. Examination of the distribution of the tensile deformation systems in tension and tension-creep of Ti-6Al-4V (wt.%) at 296 K and 728 K. *Philosophical Magazine* **95**, 691–729 (2015).
44. Anne, B. R., Okuyama, Y., Morikawa, T. & Tanaka, M. Activated slip systems in bimodal Ti–6Al–4V plastically deformed at low and moderately high temperatures. *Materials Science and Engineering: A* **798**, 140211 (2020).
45. Ivanov, S., Gushchina, M., Artinov, A., Khomutov, M. & Zemlyakov, E. Effect of elevated temperatures on the mechanical properties of a direct laser deposited Ti-6Al-4V. *Materials* **14**, 6432 (2021).
46. Alaghmandfard, R., Chalasani, D., Odeshi, A. & Mohammadi, M. Activated slip and twin systems in electron beam melted Ti-6Al-4V subjected to elevated and high strain rate dynamic deformations. *Mater Charact* **172**, 110866 (2021).

47. Chong, Y. *et al.* Yielding nature and Hall-Petch relationships in Ti-6Al-4V alloy with fully equiaxed and bimodal microstructures. *Scr Mater* **172**, 77–82 (2019).
48. Echlin, M. L. P. *et al.* Microstructure-based estimation of strength and ductility distributions for α+ β titanium alloys. *Metall Mater Trans A Phys Metall Mater Sci* **52**, 2411–2434 (2021).
49. Kuang, Y. Generation of TTT and CCT Curves for Cast Ti-6Al-4V Alloy. (University of Florida, 2004).
50. Sieniawski, J., Ziaja, W., Kubiak, K. & Motyk, M. Microstructure and Mechanical Properties of High Strength Two-Phase Titanium Alloys. in *Titanium Alloys - Advances in Properties Control* (InTech, 2013). doi:10.5772/56197.
51. Cao, S. *et al.* Role of martensite decomposition in tensile properties of selective laser melted Ti-6Al-4V. *J Alloys Compd* **744**, 357–363 (2018).
52. Shaikh, A. *et al.* Effect of temperature and cooling rates on the α+β morphology of Ti-6Al-4V alloy. *Procedia Structural Integrity* **14**, 782–789 (2019).
53. Abdel-Hady, M., Hinoshita, K. & Morinaga, M. General approach to phase stability and elastic properties of β-type Ti-alloys using electronic parameters. *Scr Mater* **55**, 477–480 (2006).
54. Ishida, K. Schaeffler-type phase diagram of Ti-based alloys. *Metallurgical and Materials Transactions A* **48**, 4990–4998 (2017).
55. Murray, J. L. The Mo−Ti (Molybdenum-Titanium) system. *Bulletin of Alloy Phase Diagrams* **2**, 185–192 (1981).
56. Weiss, I. & Semiatin, S. L. Thermomechanical processing of beta titanium alloys—an overview. *Materials Science and Engineering: A* **243**, 46–65 (1998).
57. Mei, W., Sun, J. & Wen, Y. Martensitic transformation from β to α′ and α″ phases in Ti–V alloys: A first-principles study. *J Mater Res* **32**, 3183–3190 (2017).
58. Inamura, T. *et al.* Composition dependent crystallography of α″-martensite in Ti-Nb-based β-titanium alloy. *Philosophical Magazine* **87**, 3325–3350 (2007).
59. Neelakantan, S., Rivera-Díaz-del-Castillo, P. E. J. & van der Zwaag, S. Prediction of the martensite start temperature for β titanium alloys as a function of composition. *Scr Mater* **60**, 611–614 (2009).
60. Bignon, M., Bertrand, E., Rivera-Díaz-del-Castillo, P. E. J. & Tancret, F. Martensite formation in titanium alloys: Crystallographic and compositional effects. *J Alloys Compd* **872**, 159636 (2021).
61. Zheng, Y. *et al.* The effect of alloy composition on instabilities in the β phase of titanium alloys. *Scr Mater* **116**, 49–52 (2016).
62. Zhang, J., Tasan, C. C., Lai, M. J., Dippel, A.-C. & Raabe, D. Complexion-mediated martensitic phase transformation in Titanium. *Nat Commun* **8**, 14210 (2017).

63. Sun, F. *et al.* Influence of a short thermal treatment on the superelastic properties of a titanium-based alloy. *Scr Mater* **63**, 1053–1056 (2010).
64. Ellyson, B. *et al.* Tuning the strength and ductility balance of a TRIP titanium alloy. *Scr Mater* **194**, 113641 (2021).
65. Nejezchlebová, J. *et al.* The effect of athermal and isothermal ω phase particles on elasticity of β-Ti single crystals. *Acta Mater* **110**, 185–191 (2016).
66. Du, Z. *et al.* Microstructure evolution during aging heat treatment and its effects on tensile properties and dynamic Young's modulus of a biomedical β titanium alloy. *Materials Science and Engineering: A* **791**, 139677 (2020).
67. Gysler, A., Lütjering, G. & Gerold, V. Deformation behavior of age-hardened Ti-Mo alloys. *Acta Metallurgica* **22**, 901–909 (1974).
68. Bermingham, M. J., Kent, D., Pace, B., Cairney, J. M. & Dargusch, M. S. High strength heat-treatable β-titanium alloy for additive manufacturing. *Materials Science and Engineering: A* **791**, 139646 (2020).
69. Raza, D. *et al.* Development and heat treatment of β-phase titanium alloy for orthopedic application. *Mater Today Proc* **50**, 649–654 (2021).
70. Mantri, S. A. *et al.* Tuning the scale of α precipitates in β-titanium alloys for achieving high strength. *Scr Mater* **154**, 139–144 (2018).
71. Niwa, N., Arai, A., Takatori, H. & Ito, K. Mechanical properties of cold-worked and high-low temperature duplex-aged Ti-15V-3Cr-3Sn-3Al alloy. *ISIJ International* **31**, 856–862 (1991).
72. Ho, W. F., Ju, C. P. & Chern Lin, J. H. Structure and properties of cast binary Ti–Mo alloys. *Biomaterials* **20**, 2115–2122 (1999).
73. Cardoso, F. F., Ferrandini, P. L., Lopes, E. S. N., Cremasco, A. & Caram, R. Ti–Mo alloys employed as biomaterials: Effects of composition and aging heat treatment on microstructure and mechanical behavior. *J Mech Behav Biomed Mater* **32**, 31–38 (2014).
74. Li, M., Min, X., Yao, K. & Ye, F. Novel insight into the formation of α″-martensite and ω-phase with cluster structure in metastable Ti-Mo alloys. *Acta Mater* **164**, 322–333 (2019).
75. Zheng, Y., Banerjee, D. & Fraser, H. L. A nano-scale instability in the β phase of dilute Ti–Mo alloys. *Scr Mater* **116**, 131–134 (2016).
76. Chen, W. *et al.* Origin of the ductile-to-brittle transition of metastable β-titanium alloys: Self-hardening of ω-precipitates. *Acta Mater* **170**, 187–204 (2019).
77. Blackburn, M. J. & Feeney, J. A. *Stress-Induced Transformations in Ti-Mo Alloys*. (1970).
78. Marteleur, M. *et al.* On the design of new β-metastable titanium alloys with improved work hardening rate thanks to simultaneous TRIP and TWIP effects. *Scr Mater* **66**, 749–752 (2012).

79. Sun, F. *et al.* The role of stress induced martensite in ductile metastable beta Ti-alloys showing combined TRIP/TWIP effects. *Mater Today Proc* **2**, S505–S510 (2015).
80. Min, X. H., Tsuzaki, K., Emura, S. & Tsuchiya, K. Heterogeneous twin formation and its effect on tensile properties in Ti–Mo based β titanium alloys. *Materials Science and Engineering: A* **554**, 53–60 (2012).
81. Zhou, X., Min, X. a, Emura, S. & Tsuchiya, K. Accommodative {332} 〈113〉 primary and secondary twinning in a slightly deformed β-type Ti-Mo titanium alloy. *Materials Science and Engineering: A* **684**, 456–465 (2017).
82. Koul, M. K. & Breedis, J. F. Phase transformations in beta isomorphous titanium alloys. *Acta Metallurgica* **18**, 579–588 (1970).
83. Duerig, T. W., Albrecht, J., Richter, D. & Fischer, P. Formation and reversion of stress induced martensite in Ti-10V-2Fe-3Al. *Acta Metallurgica* **30**, 2161–2172 (1982).
84. Wang, C. H., Russell, A. M. & Cao, G. H. A semi-empirical approach to the prediction of deformation behaviors of β-Ti alloys. *Scr Mater* **158**, 62–65 (2019).
85. Bignon, M., Bertrand, E., Tancret, F. & Rivera-Díaz-del-Castillo, P. E. J. Modelling martensitic transformation in titanium alloys: The influence of temperature and deformation. *Materialia (Oxf)* **7**, 100382 (2019).
86. Wang, W., Zhang, X., Mei, W. & Sun, J. Role of omega phase evolution in plastic deformation of twinning-induced plasticity β Ti–12V–2Fe–1Al alloy. *Mater Des* **186**, 108282 (2020).
87. Yao, K. & Min, X. Static and dynamic Hall–Petch relations in {332}⟨113⟩ TWIP Ti–15Mo alloy. *Materials Science and Engineering A* **827**, 142044(1-13) (2021).
88. Almeida, A., Gupta, D., Loable, C. & Vilar, R. Laser-assisted synthesis of Ti–Mo alloys for biomedical applications. *Materials Science and Engineering: C* **32**, 1190–1195 (2012).
89. Sun, F. *et al.* Strengthening strategy for a ductile metastable β -titanium alloy using low-temperature aging. *Mater Res Lett* **5**, 547–553 (2017).
90. Davis, B. W. & Varsanik, R. G. A study of crystalline titanium carbide. *J Colloid Interface Sci* **37**, 870–878 (1971).
91. Gu, D., Shen, Y. & Meng, G. Growth morphologies and mechanisms of TiC grains during Selective Laser Melting of Ti–Al–C composite powder. *Mater Lett* **63**, 2536–2538 (2009).
92. Deckard, C. R. Selective laser sintering. (University of Texas, Austin, 1988).
93. Sames, W. J., List, F. A., Pannala, S., Dehoff, R. R. & Babu, S. S. The metallurgy and processing science of metal additive manufacturing. *International Materials Reviews* **61**, 315–360 (2016).
94. Gibson, I., Rosen, D. W. & Stucker, B. *Additive Manufacturing Technologies*. *Additive Manufacturing Technologies: Rapid Prototyping to Direct Digital Manufacturing* (Springer US, 2010). doi:10.1007/978-1-4419-1120-9.

95. Herzog, D., Seyda, V., Wycisk, E. & Emmelmann, C. Additive manufacturing of metals. *Acta Mater* **117**, 371–392 (2016).
96. Wang, C. *et al.* Additive manufacturing of NiTi shape memory alloys using pre-mixed powders. *J Mater Process Technol* **271**, 152–161 (2019).
97. DebRoy, T. *et al.* Additive manufacturing of metallic components – Process, structure and properties. *Prog Mater Sci* **92**, 112–224 (2018).
98. Elmer, J. W., Wong, J., Fröba, M., Waide, P. A. & Larson, E. M. Analysis of heat-affected zone phase transformations usingin situ spatially resolved x-ray diffraction with synchrotron radiation. *Metallurgical and Materials Transactions A* **27**, 775–783 (1996).
99. Gorsse, S., Hutchinson, C., Gouné, M. & Banerjee, R. Additive manufacturing of metals: a brief review of the characteristic microstructures and properties of steels, Ti-6Al-4V and high-entropy alloys. *Sci Technol Adv Mater* **18**, 584–610 (2017).
100. Yang, J. *et al.* Formation and control of martensite in Ti-6Al-4V alloy produced by selective laser melting. *Mater Des* **108**, 308–318 (2016).
101. Li, C., Liu, J. F., Fang, X. Y. & Guo, Y. B. Efficient predictive model of part distortion and residual stress in selective laser melting. *Addit Manuf* **17**, 157–168 (2017).
102. Denlinger, E. R. & Michaleris, P. Effect of stress relaxation on distortion in additive manufacturing process modeling. *Addit Manuf* **12**, 51–59 (2016).
103. Zaeh, M. F. & Branner, G. Investigations on residual stresses and deformations in selective laser melting. *Production Engineering* **4**, 35–45 (2010).
104. Vrancken, B., Thijs, L., Kruth, J.-P. & Van Humbeeck, J. Heat treatment of Ti6Al4V produced by Selective Laser Melting: Microstructure and mechanical properties. *J Alloys Compd* **541**, 177–185 (2012).
105. Vrancken, B., Thijs, L., Kruth, J.-P. & Van Humbeeck, J. Microstructure and mechanical properties of a novel β titanium metallic composite by selective laser melting. *Acta Mater* **68**, 150–158 (2014).
106. Bhardwaj, T., Shukla, M., Paul, C. P. & Bindra, K. S. Direct energy deposition - laser additive manufacturing of titanium-molybdenum alloy: parametric studies, microstructure and mechanical properties. *J Alloys Compd* **787**, 1238–1248 (2019).
107. Lin, X., Yue, T. M., Yang, H. O. & Huang, W. D. Laser rapid forming of SS316L/Rene88DT graded material. *Materials Science and Engineering: A* **391**, 325–336 (2005).
108. Collins, P. C., Banerjee, R., Banerjee, S. & Fraser, H. L. Laser deposition of compositionally graded titanium–vanadium and titanium–molybdenum alloys. *Materials Science and Engineering: A* **352**, 118–128 (2003).
109. Liu, S. & Shin, Y. C. The influences of melting degree of TiC reinforcements on microstructure and mechanical properties of laser direct deposited Ti6Al4V-TiC composites. *Mater Des* **136**, 185–195 (2017).

110. Krajňák, T. *et al.* Microstructure evolution in compositionally graded Ti(4–12 wt% Mo) prepared by laser directed energy deposition. *Journal of Materials Research and Technology* **23**, 4527–4537 (2023).
111. Wang, F., Mei, J., Jiang, H. & Wu, X. Laser fabrication of Ti6Al4V/TiC composites using simultaneous powder and wire feed. *Materials Science and Engineering: A* **445–446**, 461–466 (2007).
112. Bobbio, L. D., Qin, S., Dunbar, A., Michaleris, P. & Beese, A. M. Characterization of the strength of support structures used in powder bed fusion additive manufacturing of Ti-6Al-4V. *Addit Manuf* **14**, 60–68 (2017).
113. Derimow, N. & Hrabe, N. Oxidation in reused powder bed fusion additive manufacturing Ti-6Al-4V feedstock: a brief review. *JOM* **73**, 3618–3638 (2021).
114. Farayibi, P. K., Abioye, T. E., Kennedy, A. & Clare, A. T. Development of metal matrix composites by direct energy deposition of 'satellited' powders. *J Manuf Process* **45**, 429–437 (2019).
115. Fu, C. H. & Guo, Y. B. Three-dimensional temperature gradient mechanism in selective laser melting of Ti-6Al-4V. *J Manuf Sci Eng* **136**, (2014).
116. Gong, H., Rafi, K., Gu, H., Starr, T. & Stucker, B. Analysis of defect generation in Ti–6Al–4V parts made using powder bed fusion additive manufacturing processes. *Addit Manuf* **1–4**, 87–98 (2014).
117. Chen, Q. *et al.* Elucidating the effect of preheating temperature on melt pool morphology variation in Inconel 718 laser powder bed fusion via simulation and experiment. *Addit Manuf* **37**, 101642 (2021).
118. Chen, W. *et al.* Controlling the microstructure and mechanical properties of a metastable β titanium alloy by selective laser melting. *Materials Science and Engineering: A* **726**, 240–250 (2018).
119. Yap, C. Y. *et al.* Review of selective laser melting: Materials and applications. *Appl Phys Rev* **2**, 041101 (2015).
120. Tonelli, L., Fortunato, A. & Ceschini, L. CoCr alloy processed by Selective Laser Melting (SLM): effect of Laser Energy Density on microstructure, surface morphology, and hardness. *J Manuf Process* **52**, 106–119 (2020).
121. Wycisk, E. *et al.* Effects of defects in laser additive manufactured Ti-6Al-4V on fatigue properties. *Phys Procedia* **56**, 371–378 (2014).
122. Suzuki, A., Nishida, R., Takata, N., Kobashi, M. & Kato, M. Design of laser parameters for selectively laser melted maraging steel based on deposited energy density. *Addit Manuf* **28**, 160–168 (2019).

123. Song, B., Dong, S., Liao, H. & Coddet, C. Process parameter selection for selective laser melting of Ti6Al4V based on temperature distribution simulation and experimental sintering. *The International Journal of Advanced Manufacturing Technology* **61**, 967–974 (2012).
124. Dzogbewu, T. C. & du Preez, W. B. In situ alloying of Ti-10Mo fused tracks and layers via laser powder bed fusion. *Manuf Rev (Les Ulis)* **9**, 23 (2022).
125. Liu, S., Stebner, A. P., Kappes, B. B. & Zhang, X. Machine learning for knowledge transfer across multiple metals additive manufacturing printers. *Addit Manuf* **39**, 101877 (2021).
126. Lingda, X., Guoli, Z., Gaoyang, M., Chunming, W. & Ping, J. A phase-field simulation of columnar-to-equiaxed transition in the entire laser welding molten pool. *J Alloys Compd* **858**, 157669 (2021).
127. Raghavan, N. *et al.* Numerical modeling of heat-transfer and the influence of process parameters on tailoring the grain morphology of IN718 in electron beam additive manufacturing. *Acta Mater* **112**, 303–314 (2016).
128. Kurz, W., Bezençon, C. & Gäumann, M. Columnar to equiaxed transition in solidification processing. *Sci Technol Adv Mater* **2**, 185–191 (2001).
129. Bermingham, M. J., StJohn, D. H., Krynen, J., Tedman-Jones, S. & Dargusch, M. S. Promoting the columnar to equiaxed transition and grain refinement of titanium alloys during additive manufacturing. *Acta Mater* **168**, 261–274 (2019).
130. Nabavizadeh, S. A., Eshraghi, M. & Felicelli, S. D. Three-dimensional phase field modeling of columnar to equiaxed transition in directional solidification of Inconel 718 alloy. *J Cryst Growth* **549**, 125879 (2020).
131. Mokadem, S., Bezençon, C., Hauert, A., Jacot, A. & Kurz, W. Laser repair of superalloy single crystals with varying substrate orientations. *Metallurgical and Materials Transactions A* **38**, 1500–1510 (2007).
132. Wang, T., Zhu, Y. Y., Zhang, S. Q., Tang, H. B. & Wang, H. M. Grain morphology evolution behavior of titanium alloy components during laser melting deposition additive manufacturing. *J Alloys Compd* **632**, 505–513 (2015).
133. Sofinowski, K. A., Raman, S., Wang, X., Gaskey, B. & Seita, M. Layer-wise engineering of grain orientation (LEGO) in laser powder bed fusion of stainless steel 316L. *Addit Manuf* **38**, 101809 (2021).
134. Li, C. L. *et al.* Simultaneous achievement of equiaxed grain structure and weak texture in Pure Titanium via selective laser melting and subsequent heat treatment. *J Alloys Compd* **803**, 407–412 (2019).
135. Liu, S. & Shin, Y. C. Additive manufacturing of Ti6Al4V alloy: A review. *Mater Des* **164**, 107552 (2019).

136. Simonelli, M., Tse, Y. Y. & Tuck, C. Effect of the build orientation on the mechanical properties and fracture modes of SLM Ti–6Al–4V. *Materials Science and Engineering: A* **616**, 1–11 (2014).
137. Yang, J., Yu, H., Wang, Z. & Zeng, X. Effect of crystallographic orientation on mechanical anisotropy of selective laser melted Ti-6Al-4V alloy. *Mater Charact* **127**, 137–145 (2017).
138. Wu, M.-W., Lai, P.-H. & Chen, J.-K. Anisotropy in the impact toughness of selective laser melted Ti–6Al–4V alloy. *Materials Science and Engineering: A* **650**, 295–299 (2016).
139. Todaro, C. J. *et al.* Grain structure control during metal 3D printing by high-intensity ultrasound. *Nat Commun* **11**, 1–9 (2020).
140. Helmer, H., Bauereiß, A., Singer, R. F. & Körner, C. Grain structure evolution in Inconel 718 during selective electron beam melting. *Materials Science and Engineering A* **668**, 180–187 (2016).
141. Zhang, F., Mei, M., Al-Hamdani, K., Tan, H. & Clare, A. T. Novel nucleation mechanisms through satelliting in direct metal deposition of Ti-15Mo. *Mater Lett* **213**, 197–200 (2018).
142. Dehoff, R. R. *et al.* Site specific control of crystallographic grain orientation through electron beam additive manufacturing. *Materials Science and Technology (United Kingdom)* **31**, 931–938 (2015).
143. Pinomaa, T., Laukkanen, A. & Provatas, N. Solute trapping in rapid solidification. *MRS Bull* **45**, 910–915 (2020).
144. Hillert, M. Solute drag, solute trapping and diffusional dissipation of Gibbs energy. *Acta Mater* **47**, 4481–4505 (1999).
145. Aziz, M. J. & Kaplan, T. Continuous growth model for interface motion during alloy solidification. *Acta Metallurgica* **36**, 2335–2347 (1988).
146. Liu, J. *et al.* Effects of post heat treatments on microstructures and mechanical properties of selective laser melted Ti6Al4V alloy. *Metals (Basel)* **11**, 1593 (2021).
147. Liu, J. *et al.* Grain boundary α-phase precipitation and coarsening: Comparing laser powder bed fusion with as-cast Ti-6Al-4V. *Scr Mater* **207**, 114261 (2022).
148. Lu, Y., Tang, H. B., Fang, Y. L., Liu, D. & Wang, H. M. Microstructure evolution of sub-critical annealed laser deposited Ti–6Al–4V alloy. *Mater Des* **37**, 56–63 (2012).
149. Qiu, C., Adkins, N. J. E. & Attallah, M. M. Microstructure and tensile properties of selectively laser-melted and of HIPed laser-melted Ti–6Al–4V. *Materials Science and Engineering: A* **578**, 230–239 (2013).
150. Qi, M. *et al.* Columnar to equiaxed transition during β heat treatment in a near β alloy by laser additive manufacture. *Journal of Materials Research and Technology* **13**, 1159–1168 (2021).

151. Ng, C. H., Bermingham, M. J. & Dargusch, M. S. Controlling grain size, morphology and texture in additively manufactured β-titanium alloy with super transus hot isostatic pressing. *Addit Manuf* **59**, (2022).
152. Chong, Y. *et al.* Elimination of oxygen sensitivity in α-titanium by substitutional alloying with Al. *Nature Communications* **12**, 6158 (2021).
153. Finlay, W. L. & Snyder, J. A. Effects of three interstitial solutes (nitrogen, oxygen, and carbon) on the mechanical properties of high-purity, alpha titanium. *JOM* **2**, 277–286 (1950).
154. Jaffee, R. I., Ogden, H. R. & Maykuth, D. J. Alloys of titanium with carbon, oxygen, and nitrogen. *JOM* **2**, 1261–1266 (1950).
155. Ogden, H. R. & Jaffee, R. I. *The Effects of Carbon, Oxygen, and Nitrogen on the Mechanical Properties of Titanium and Titanium Alloys*. http://www.osti.gov/servlets/purl/4370612-Z0r4S5/native/ (1955) doi:10.2172/4370612.
156. Conrad, H. The rate controlling mechanism during yielding and flow of α-titanium at temperatures below 0.4 TM. *Acta Metallurgica* **14**, 1631–1633 (1966).
157. Conrad, H. Effect of interstitial solutes on the strength and ductility of titanium. *Prog Mater Sci* **26**, 123–403 (1981).
158. Nayak, S. K. *et al.* Insight into point defects and impurities in titanium from first principles. *NPJ Comput Mater* **4**, (2018).
159. Montanari, R., Costanza, G., Tata, M. E. & Testani, C. Lattice expansion of Ti–6Al–4V by nitrogen and oxygen absorption. *Mater Charact* **59**, 334–337 (2008).
160. Nakajima, H. & Koiwa, M. Diffusion in Titanium. *ISIJ International* **31**, 757–766 (1991).
161. Scotti, L. & Mottura, A. Interstitial diffusion of O, N, and C in α-Ti from first-principles: Analytical model and kinetic Monte Carlo simulations. *J Chem Phys* **144**, 084701 (2016).
162. Chong, Y. *et al.* Mechanistic basis of oxygen sensitivity in titanium. *Sci Adv* **6**, 4060–4083 (2020).
163. Wang, C. S. *et al.* Tailoring bimodal structure for high strength and ductility in pure titanium manufactured via laser powder bed fusion. *J Alloys Compd* **901**, 163590 (2022).
164. S. Kariya *et al.* Effect of grain size on the tensile ductility and fracture mechanism of Ti-O alloy. *Materials Science and Engineering: A* **874**, 145068 (2023).
165. Liu, L. *et al.* In-situ nitrogen strengthening of selective laser melted Ti6Al4V with superior mechanical performance. *Addit Manuf* **46**, 102142 (2021).
166. Wysocki, B. *et al.* Microstructure and mechanical properties investigation of CP titanium processed by selective laser melting (SLM). *J Mater Process Technol* **241**, 13–23 (2017).
167. Kondoh, K. *et al.* Tensile property enhancement by oxygen solutes in selectively laser melted titanium materials fabricated from pre-mixed pure Ti and TiO2 powder. *Materials Science and Engineering: A* **795**, 139983 (2020).

168. Issariyapat, A., Visuttipitukul, P., Umeda, J. & Kondoh, K. Refined grain formation behavior and strengthening mechanism of α-titanium with nitrogen fabricated by selective laser melting. *Addit Manuf* **36**, 101537 (2020).
169. Kondoh, K., Issariyapat, A., Umeda, J. & Visuttipitukul, P. Selective laser-melted titanium materials with nitrogen solid solutions for balanced strength and ductility. *Materials Science and Engineering: A* **790**, 139641 (2020).
170. Hennig, R. G. *et al.* Impurities block the α to ω martensitic transformation in titanium. *Nature Materials* **4**, 129–133 (2005).
171. Wang, X. L., Li, L., Xing, H., Ou, P. & Sun, J. Role of oxygen in stress-induced ω phase transformation and {3 3 2} 〈1 1 3〉 mechanical twinning in βTi–20V alloy. *Scr Mater* **96**, 37–40 (2015).
172. Yan, M. *et al.* Review of effect of oxygen on room temperature ductility of titanium and titanium alloys. *Powder Metallurgy* **57**, 251–257 (2014).
173. Okamoto, H. C−Ti (Carbon-Titanium). *J Phase Equilibria Diffus* **27**, 306–307 (2006).
174. Elkhateeb, M. G. & Shin, Y. C. Molecular dynamics-based cohesive zone representation of Ti6Al4V/TiC composite interface. *Mater Des* **155**, 161–169 (2018).
175. Wang, X. *et al.* Microstructure Evolution and Enhanced Hot Workability of TiC/Ti-6Al-4V Composites Fabricated by Melt Hydrogenation. *Materials* **15**, 8884 (2022).
176. Loretto, M. H. & Konitzer, D. G. The effect of matrix reinforcement reaction on fracture in Ti-6Al-4V base composites. *Composites Manufacturing* **1**, 263 (1990).
177. Dong, M., Zhou, W., Zhou, Z. & Nomura, N. Simultaneous enhancement of powder properties, additive manufacturability, and mechanical performance of Ti–6Al–4V alloy by 2D-nanocarbon decoration. *Materials Science and Engineering A* **859**, 144215 (2022).
178. Yi, M. *et al.* Comparative investigation on microstructures and mechanical properties of (TiB + TiC)/Ti-6Al-4V composites from Ti-B4C-C and Ti-TiB2-TiC systems. *Mater Charact* **140**, 281–289 (2018).
179. Shi, Q. *et al.* In-situ formation of Ti-Mo biomaterials by selective laser melting of Ti/Mo and Ti/Mo2C powder mixtures: A comparative study on microstructure, mechanical and wear performance, and thermal mechanisms. *J Mater Sci Technol* **115**, 81–96 (2022).
180. Cai, C. *et al.* Laser powder bed fusion of Mo2C/Ti-6Al-4V composites with alternately laminated α′/β phases for enhanced mechanical properties. *Addit Manuf* **46**, 102134 (2021).
181. Mandal, V., Tripathi, P., Kumar, A., Singh, S. S. & Ramkumar, J. A study on selective laser melting (SLM) of TiC and B4C reinforced IN718 metal matrix composites (MMCs). *J Alloys Compd* **901**, 163527 (2022).
182. Vrancken, B. *et al.* Selective Laser Melting process optimization of Ti–Mo–TiC metal matrix composites. *CIRP Annals* **68**, 221–224 (2019).

183. Wei, W. *et al.* Agglomeration-free nanoscale TiC reinforced titanium matrix composites achieved by in-situ laser additive manufacturing. *Scr Mater* **187**, 310–316 (2020).
184. Li, H. *et al.* Effect of heat treatment on microstructure evolution and mechanical properties of selective laser melted Ti–6Al–4V and TiB/Ti–6Al–4V composite: A comparative study. *Materials Science and Engineering: A* **801**, 140415 (2021).
185. Dadbakhsh, S., Mertens, R., Vanmeensel, K., Ji, G. & Kruth, J.-P. In situ transformations during SLM of an ultra-strong TiC reinforced Ti composite. *Sci Rep* **10**, 10523 (2020).
186. Ochonogor, O. F., Meacock, C., Abdulwahab, M., Pityana, S. & Popoola, A. P. I. Effects of Ti and TiC ceramic powder on laser-cladded Ti–6Al–4V in situ intermetallic composite. *Appl Surf Sci* **263**, 591–596 (2012).
187. Gu, D., Hagedorn, Y.-C., Meiners, W., Wissenbach, K. & Poprawe, R. Nanocrystalline TiC reinforced Ti matrix bulk-form nanocomposites by Selective Laser Melting (SLM): Densification, growth mechanism and wear behavior. *Compos Sci Technol* **71**, 1612–1620 (2011).
188. Tang, M., Zhang, L. & Zhang, N. Microstructural evolution, mechanical and tribological properties of TiC/Ti6Al4V composites with unique microstructure prepared by SLM. *Materials Science and Engineering: A* **814**, 141187 (2021).
189. Borisov, E., Masaylo, D. V. & Popovich, V. Selective laser melting of nanocomposite Ti-6Al-4V and TiC powder. *Key Eng Mater* **822**, 575–579 (2019).
190. Wagoner Johnson, A. J., Kumar, K. S. & Briant, C. L. Deformation mechanisms in Ti-6Al-4V/TiC composites. *Metallurgical and Materials Transactions A* **34**, 1869–1877 (2003).
191. Kwasniak, P., Muzyk, M., Garbacz, H. & Kurzydlowski, K. J. Influence of C, H, N, and O interstitial atoms on deformation mechanism in titanium—First principles calculations of generalized stacking fault energy. *Mater Lett* **94**, 92–94 (2013).
192. Mathieu, J. B., Mathieu, H. J. & Landolt, D. Electropolishing of Titanium in Perchloric Acid-Acetic Acid Solution: I . Auger Electron Spectroscopy Study of Anodic Films. *J Electrochem Soc* **125**, 1039–1043 (1978).
193. ASTM. Standard Guide for Electrolytic Polishing of Metallographic Specimens. *ASTM International* **ASTM E1558**, (2014).
194. Chen, K., Huang, D. J., Li, H., Jia, N. & Chong, W. Avoiding abnormal grain growth when annealing selective laser melted pure titanium by promoting nucleation. *Scr Mater* **209**, 114377 (2022).
195. Harwig, D., Ittiwattana, M. & Castner, H. Advances in oxygen equivalent equations for predicting the properties of titanium welds. *Welding Journal (Miami, Fla)* **80**, (2001).
196. De Barros, M. I., Rats, D., Vandenbulcke, L. & Farges, G. Influence of internal diffusion barriers on carbon diffusion in pure titanium and Ti–6Al–4V during diamond deposition. *Diam Relat Mater* **8**, 1022–1032 (1999).

197. Wolf, D. Correlation between the energy and structure of grain boundaries in b.c.c. metals. II. Symmetrical tilt boundaries. *Philosophical Magazine A* **62**, 447–464 (1990).
198. Karbasi, M., Yazdian, N. & Vahidian, A. Development of electro-co-deposited Ni–TiC nano-particle reinforced nanocomposite coatings. *Surf Coat Technol* **207**, 587–593 (2012).
199. Sabeena, M. *et al.* Microstructural characterization of transformation products of bcc β in Ti-15 Mo alloy. *Journal of Alloys and Compounds* **658**, 301–315 (2016).
200. Lu, J. W., Zhao, Y. Q., Ge, P. & Niu, H. Z. Microstructure and beta grain growth behavior of Ti-Mo alloys solution treated. *Mater Charact* **84**, 105–111 (2013).
201. Chen, Y. C., Lin, J. H. C. & Ju, C. P. Effects of post-aging cooling condition on structure and tensile properties of aged Ti-7.5Mo alloy. *Mater Des* **54**, 515–519 (2014).
202. Gao, J. *et al.* Deformation mechanisms in a metastable beta titanium twinning induced plasticity alloy with high yield strength and high strain hardening rate. *Acta Mater* **152**, 301–314 (2018).
203. Du, C. *et al.* Deformation-induced grain rotation and grain boundary formation achieved through dislocation-disclination reactions in polycrystalline hexagonal close-packed metals. *Acta Mater* **250**, 118855 (2023).
204. Du, C. *et al.* Deformation-induced grain rotation and grain boundary formation achieved through dislocation-disclination reactions in polycrystalline hexagonal close-packed metals. *Acta Mater* **250**, 118855 (2023).
205. Hémery, S., Tromas, C. & Villechaise, P. Slip-stimulated grain boundary sliding in Ti-6Al-4 V at room temperature. *Materialia* **5** (2019).
206. Ren, Y., Zhang, X., Xia, T., Sun, Q. & Liu, Q. Microstructural and textural evolution of high-purity titanium under dynamic loading. *Mater Des* **126**, 123–134 (2017).
207. Tan, C., Sun, Q. & Zhang, G. Role of microstructure in plastic deformation and crack propagation behaviour of an α/β titanium alloy. *Vacuum* **183**, 109848 (2021).

Attributions

List of Publications

Academic Journal Publications:

J. Peterson, A. Issariyapat, J. Umeda, K. Kondoh. The effects of heat treatment and carbon content on the microstructure and mechanical properties of laser powder bed fusion Ti-6Al-4V with dissolved TiC particles. *Journal of Alloys and Compounds* 920 (2022). https://doi.org/10.1016/j.jallcom.2022.165930

J. Peterson, S. Kariya, A. Issariyapat, J. Umeda, K. Kondoh. Experimentally mapping the oriented-to-misoriented transition in laser powder bed fusion Ti-10%Mo alloys. *Scripta Materialia* 231 (2023). https://doi.org/10.1016/j.scriptamat.2023.115472

J. Peterson, A. Issariyapat, S. Kariya, J. Umeda, K. Kondoh. The mechanical and microstructural behavior of heat treated, texture-controlled Ti-10%Mo alloys manufactured by laser powder bed fusion. *Materials Science and Engineering: A.* Under Review.

Presentations and Posters:

J. Peterson, S. Kariya, J. Umeda, K. Kondoh. Experimentally mapping the columnar-to-equiaxed transition in laser powder bed fusion Ti-10%Mo Alloys. Poster presented at: Visual JW 2022 and DEJI2MA-2; October 25th, 2022; Osaka, Japan.

J. Peterson, J. Umeda, K. Kondoh. Mapping a novel columnar-to-isotropic transition in laser powder bed fusion Ti-10Mo. Presented at: Autumn Meeting of Japan Institute of Metals and Materials, 2022; September 22nd, 2022; Fukuoka, Japan.

J. Peterson, E. Ichikawa, J. Umeda, K. Kondoh. SLM Induced Carbon Solid Solution in Titanium Alloys. Presented at: 2022 Autumn Meeting of Japan Society of Powder and Powder Metallurgy; November 11th, 2021; Online Remote Conference.

Acknowledgements

The production of this thesis was assisted by a number of people who have been generous with their time, knowledge, and support. I would like to take this time to recognize their contributions.

Firstly, I would like to thank Professor Katsuyoshi Kondoh for his guidance over the past six years. His enthusiasm for and infallible knowledge of the metallurgical sciences have been an invaluable boon for both my academic progress and personal interest in this field.

Next, I would like to thank Professor Junko Umeda for her support in making this thesis logistically possible. She handled the administrative aspects of not only the academic side of this project, but also the monumental hurdle of helping me adjust to life across the planet.

I am also incredible grateful for the assistant professors Ammarueda Issariyapat, Shota Kariya, and Abdollah Bahador. Dr. Issariyapat's guidance on experimental design and technical writing allowed this thesis to develop a cohesive story and structure. The insights of Dr. Kariya and Dr. Bahador into the science and industry of titanium manufacturing have repeatedly saved me whenever I got stuck with a problem.

My gratitude extends to the entire Kondoh-Umeda Lab for always making me welcome and giving me a home away from home. I would particularly like to acknowledge the staff members Mrs. Takeda, Mr. Minamitani, Mrs. Fujii, and Mr. Murakami for their technical expertise and helping my research run quickly and smoothly. The students of the Department of Composite Materials Processing have my appreciation for their friendship and for making my time here so pleasant with lunch runs, birthday celebrations, and lab trips. I would like to recognize Eri Ichikawa for her contributions to the research included in this thesis and for her kind assistance when I was getting set up.

I gratefully acknowledge the Light Metals Educational Foundation, the Joining and Welding Research Institute, and Osaka University for giving me the opportunity to study here.

I will finish by thanking all the friends and family in Japan and California who supported me along this endeavor. Special thanks goes to my father, Bret Peterson, for reading through each chapter of this thesis to ensure that it was all intelligible.